Technical University of Munich
CERN

Development and performance study for the ALICE ITS3: the first truly cylindrical inner tracker

Supervisors:

Prof. Dr. Laura Fabbietti

Dr. Magnus Mager

Candidate:

Isabella Sanna

TUM School of Natural Sciences

Development and performance study for the ALICE ITS3: the first truly cylindrical inner tracker

Isabella Sanna

Complete reprint of the dissertation approved by the TUM School of Natural Sciences of the Technical University of Munich for the award of the Doktorin der Naturwissenschaften (Dr. rer. nat.)

Chair: Prof. Dr. Nora Brambilla

Examiners: 1. Prof. Dr. Laura Fabbietti
2. Priv.-Doz. Dr. Oliver Kortner

The dissertation was submitted to the Technical University of Munich on 30.01.2025 and accepted by the TUM School of Natural Sciences on 12.02.2025

Development and performance study for the ALICE ITS3: the first truly cylindrical inner tracker

ABSTRACT

The ITS3 upgrade of the ALICE experiment at the Large Hadron Collider (LHC) represents a significant leap in vertex detector technology. Scheduled for installation during the third LHC Long Shutdown (LS3, 2026-2029), this upgrade will replace the three innermost layers of the current system with curved, wafer-scale, ultra-thin silicon sensors arranged in truly cylindrical geometries. This novel configuration aims at reducing the material budget, and enhancing the tracking performance.

Achieving this breakthrough requires the adoption of innovative approaches, some of which are unprecedented in high-energy physics. These include low-speed air-flow cooling, bent silicon, stitching technology, and the deployment of a new sensor design based on a 65 nm CMOS imaging process. Moving to a 65 nm process requires a technology qualification phase, dedicated to process optimisation and charge collection performance evaluation with respect to pixel size, pixel design and radiation load.

This thesis focuses on the characterization of an analog prototype sensor developed using the 65 nm technology. An extensive series of measurements was conducted, including laboratory experiments using an ^{55}Fe source and beam tests, to assess charge collection efficiency, detection efficiency, and radiation tolerance. Several variants of the prototype were tested to identify the optimal design for the ITS3 application.

Complementing the experimental work, a detailed simulation study was undertaken to model the charge collection process. The simulation workflow involved calculating the sensor's electric field using TCAD simulations and employing this field in Garfield++ to simulate charge transport and collection mechanism. The charge collection information is then used to simulate the chip reponse to X-rays coming from the ^{55}Fe source. The simulated results show a good agreement with the experimental data, allowing for a deep understanding of the device.

The findings presented in this thesis highlight the potential of MAPS technology for high-energy particle detection. The 65 nm CMOS imaging process was conclusively validated as a robust solution for the ITS3 upgrade, while the developed simulation framework demonstrates its potential as a powerful tool for the design and optimization of MAPS sensors. Beyond the ITS3, these technological advancements and methodologies hold promise for future applications in high-energy physics and other applications.

Contents

1 ALICE at the LHC **1**

1.1 ALICE and the LHC complex 1

1.2 Physics motivations 3

1.2.1 QGP probes 5

1.3 The ALICE detector 6

1.3.1 The Inner Tracking System 8

2 ITS3 **13**

2.1 A novel vertex detector 13

2.1.1 Low-speed air-flow cooling 13

2.1.2 Bent silicon 15

2.1.3 Stitching 16

2.1.4 65 nm imaging process 17

2.2 Detector Layout 18

2.3 Physics performance 20

2.3.1 Tracking performance 20

2.3.2 Measurement of Λ_c 21

2.3.3 Measurement of thermal dielectrons 23

2.3.4 Complementarity with other LHC experiments 24

3 Monolithic Active Pixel Sensors **27**

3.1 Silicon properties 28

3.1.1 Band structure 28

3.1.2 Doping and junctions 29

3.1.3 Charge carrier migration 32

3.2 Radiation damage 34

3.2.1 Non-ionising radiation damage 35

3.2.2 Ionising radiation damage 37

3.3 Energy loss of particles in silicon detectors 37

3.3.1 Charged particles 37

3.3.2 Electromagnetic radiation 40
3.4 Working principles of Monolithic Active Pixel Sensors 43

4 The Analogue Pixel Test Structure 47
4.1 The APTS chip 47
4.1.1 In pixel front-end 50
4.1.2 Test system 51
4.2 Signal extraction and noise 53
4.3 Front-end parameters and operating point determination 56
4.3.1 $\mathrm{I}_{\mathrm{reset}}$ tuning 59
4.4 ^{55}Fe measurements 63
4.4.1 Energy calibration 64
4.4.2 Variants comparison 67
4.5 Testbeam 77
4.5.1 Charge distribution 78
4.5.2 Detection efficiency 80
4.6 Summary 83

5 Simulation of charge collection process in MAPS 85
5.1 Simulation structure 86
5.2 Device simulation - TCAD 87
5.2.1 Geometry 87
5.2.2 Doping profiles and meshing 88
5.2.3 Sentaurus Device simulation 90
5.3 Charge collection simulation - Garfield++ 91
5.3.1 Charge transport mechanism 93
5.4 Simulation of the chip response to X-rays 94
5.5 Results 95
5.5.1 Carrier lifetime investigation 96
5.5.2 Variants comparison 103
5.6 Summary 105

6 Outlook & Conclusions 107
6.1 Outlook 107
6.2 Conclusions 111

A Baseline autocorrelation 115

B $\mathrm{I_{reset}}$ effect on the signal extraction **117**

C Comparison between Garfield++ and Allpix2 simulations **119**

Bibliography **121**

List of Figures **131**

List of Tables **141**

Acknowledgements **145**

Chapter 1

ALICE at the LHC

In this chapter an overview of the ALICE experiment at the LHC is provided. This is followed by an outline on the primary physics motivations driving the experiment, and a description of ALICE's unique capabilities and significant contributions to high-energy physics research, particularly on the physics of ultra-relativistic heavy-ion collisions. Finally, a description of the ALICE detector is given, detailing its various components and technological advancements, with emphasis on the Inner Tracking System.

1.1 ALICE and the LHC complex

A Large Ion Collider Experiment (ALICE) is one of the four large experiments located at the Large Hadron Collider (LHC) at the the European Organization for Nuclear Research (CERN).

LHC is the final component of the CERN accelerator complex [1, 2] (see Figure 1.1) and, with its circumference of 26.7 kilometers, is the largest accelerator ever built.

The first LHC collision took place in November 2009. Since then, the maximum center-of-mass energy was reached during LHC Run 3, with $\sqrt{s_{NN}} = 5.36$ TeV per nucleon for Pb ions collisions and $\sqrt{s_{NN}} = 13.6$ TeV for protons collisions [3].

The beams that collide at the LHC are accelerated through a series of machines, each raising their energy to progressively higher levels. They travel in opposite directions within separate beam pipes maintained at an ultra-high vacuum (below 1.013×10^{-11} mbar) to minimize interactions with gas molecules. They are guided by an 8.3 Tesla magnetic field, generated by 1,232 main dipoles, with 392 quadrupoles ensuring a focused collimation.

From LHC Run 3, protons are produced in Linear Accelerator 4 (Linac 4) [4], where negative hydrogen ions are accelerated to 160 MeV. These ions are then sent to the Proton Synchrotron Booster (PSB), which strips their electrons, leaving only protons. The protons are further accelerated in stages by the Proton Synchrotron (PS) and the

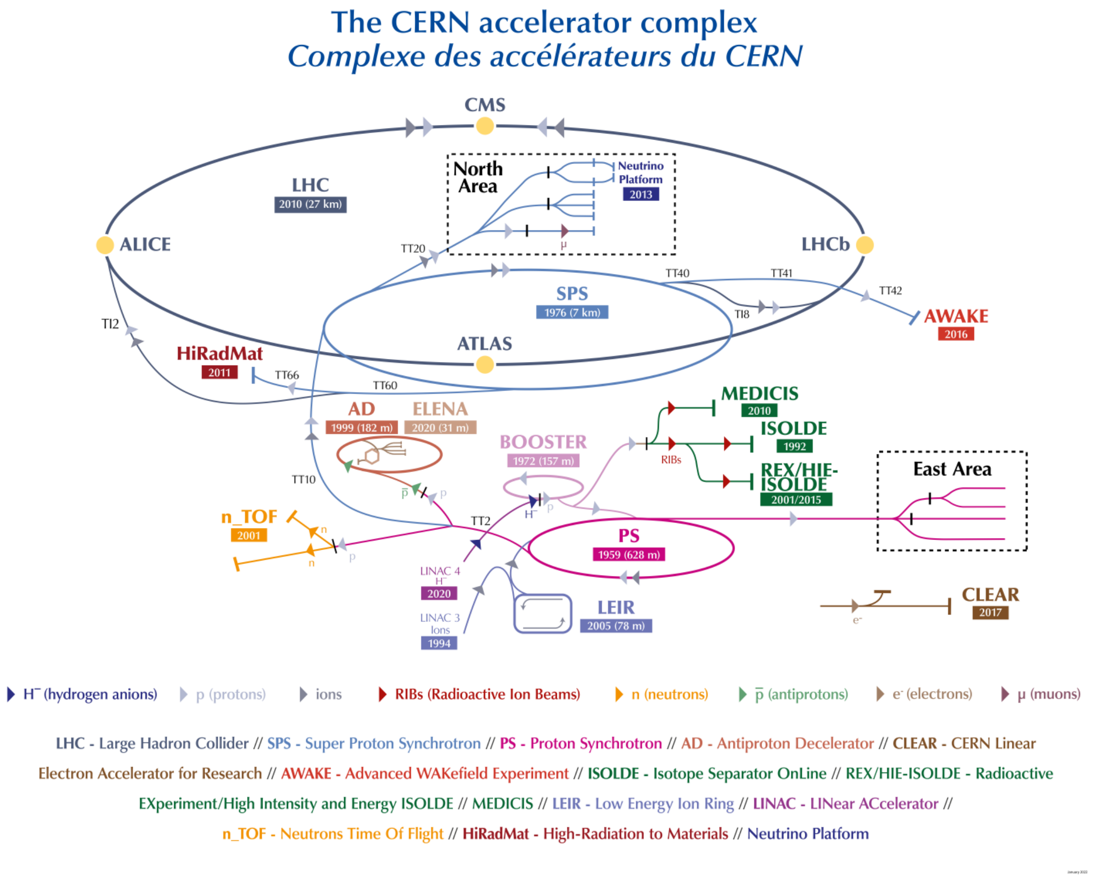

Figure 1.1: Schematic of the CERN accelerator complex and the LHC experiments. Taken from [2].

Super Proton Synchrotron (SPS) to 450 GeV before injection into the LHC, where they reach their final energy in approximately four minutes. A similar process is followed for lead ions, which are generated from vaporized lead in Linac 3, sent to the Low Energy Ion Ring (LEIR), and then transferred to the PS to follow the same path as the protons [1].

The two beams produced are brought into collision at four points, where the main CERN experiments are located: A Toroidal LHC Apparatus (ATLAS) [5], Compact Muon Solenoid (CMS) [6], ALICE [7] and LHCb [8].

ATLAS and CMS are general purpose detectors designed to measure the Higgs boson, discovered in 2012 [9][10], and to search for physics beyond the Standard Model [11]. The LHCb experiment was built to investigate the physics of beauty quark and to study the matter-antimatter asymmetry [12]. Finally, the ALICE experiment is focused on the physics of ultra-relativistic heavy-ion collisions [13].

Part of the LHC physics programme is devoted to studying the properties of the strongly interacting matter at extreme energy densities reached in ultra-relativistic heavy-ion collisions. The ALICE detector has been specifically designed to take advantage of the unique opportunities provided by the LHC heavy ion program, its main purpose is the measurement of signatures and properties of the Qark-Gluon Plasma (QGP), which is described more in detail in Section 1.2.

1.2 Physics motivations

Quantum Chromodynamics (QCD) is a fundamental component of the Standard Model of particle physics, describing the strong interaction, also known as the strong force [14]. This force governs the interactions between quarks and gluons, the fundamental constituents of protons, neutrons and all hadrons. Similar to Quantum Electrodynamics (QED), where photons mediate electromagnetic interactions, QCD features gluons as the carriers of the strong interaction and quarks as the basic building blocks of matter.

There are six flavors of quarks: up (u), down (d), strange (s), charm (c), top (t), and bottom (b). Up and down quarks have the lowest mass among all the quarks, are stable and constitute all the observable matter. The other quarks rapidly decay into up and down quarks, and generally can be observed only during high energy events like LHC collisions.

A key feature of QCD is the behavior of its coupling constant, α_S, that decreases logarithmically at short distances or high momenta and increases at long distances or low momenta. This behavior results in distinct phases of strongly interacting matter [15], sketched in a QCD phase diagram shown in Figure 1.2.

Ordinary hadronic matter is located at low temperatures T and low baryon densities, where quarks and gluons are confined. For very high energy densities, quarks are expected to become deconfined (asymptotic freedom) and can propagate freely over distances larger than the size of a nucleus, leading to the formation of a new phase known as the Quark-Gluon Plasma (QGP) [16, 17]. This phase, where quarks and gluons are not localized and constitute a hot and dense medium, is believed to have existed for approximately 10 µs after the Big Bang [18]. Ultra-relativistic heavy-ion collisions, such as those conducted at the CERN LHC, can recreate these conditions allowing to study the properties and signatures of the QGP.

Following an ultra-relativistic collision of heavy ions, the resulting system evolves

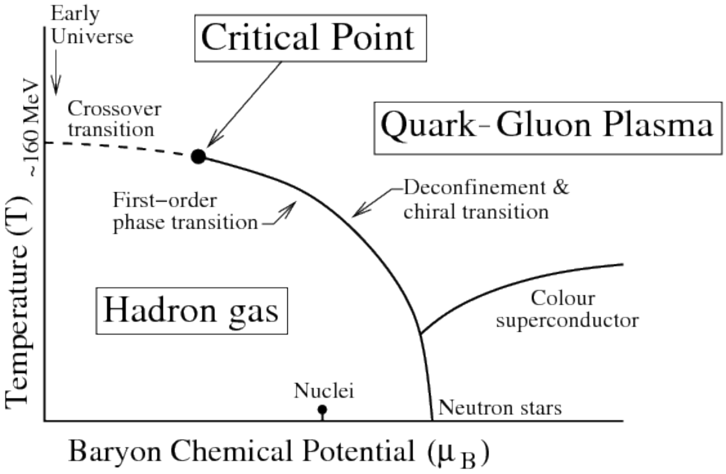

Figure 1.2: Illustration of the phase diagram of strongly interacting matter. Taken from [15].

through several distinct stages [19]. The space-time evolution of a heavy-ion collision is sketched in Figure 1.3.

Initially, during the ’pre-equilibrium’ phase, particles are produced from the energy deposited in the interaction region by the colliding ions and they are scattered through hard processes, leading to the system’s thermalization. The high energy densities present during this stage result in the formation of the QGP. This ’QGP phase’ is best described using relativistic fluid dynamics. As the system continues to expand, it cools and eventually reaches a critical temperature, transitioning into the ’hadronization phase,’ where a hadron gas is formed. During this phase, thermal equilibrium is maintained through inelastic collisions. The next stage, known as ’chemical freeze-out,’ occurs when these inelastic collisions cease, fixing the relative abundances of hadrons. Finally, the system reaches the ’kinetic freeze-out’ phase, marked by the end of elastic collisions. At this stage, the momentum spectrum of the system’s constituents becomes fixed, allowing them to move freely away from the interaction point.

The QGP features a small size and short lifetime, which is expected to be a few femtometers in diameter and less than 10 femtoseconds in duration [18]. Additionally, its signals compete with all the background deriving from the hot hadronic gas phase following the plasma hadronization. For these reasons, QGP is not easy to identify and it becomes crucial to estabilish appropriate experimental tools to observe its formation and study its properties.

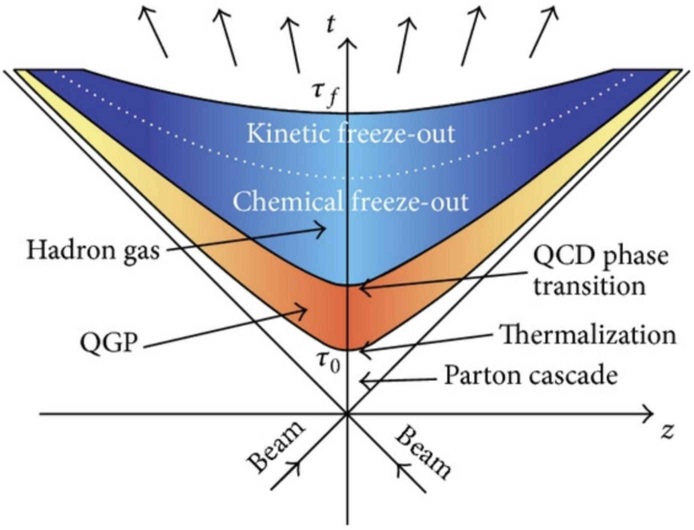

Figure 1.3: Space-time evolution of a heavy-ion collision. Taken from [20].

1.2.1 QGP probes

There are many signatures that can be investigated to probe the QGP and its properties [21].

For example, dileptons (electron-positron or muon-antimuon pairs) serve as penetrating probes of the QGP, as they do not interact strongly with the medium and thus escape without significant modification. In particular, the invariant mass spectra of dileptons can offer insights into the time-avaraged temperature of the medium that emits them. An experimental challenge of this measurement is that the region of interest of the mass spectrum has a potentially large background coming from semi-leptonic charm decays [21].

Other important probes for the understanding of the QGP are the heavy flavour measurements, which involve the study of particles containing charm or bottom quarks. These quarks are produced in the early stages of heavy-ion collisions due to their large masses, which require high-energy processes. Since they experience the entire evolution of the QGP, they serve as excellent probes of the medium's characteristics [22]. By analyzing how heavy flavour particles interact with and lose energy in the QGP, it is possible to gain insights into the medium's temperature, density, and transport properties.

Most of the heavy quarks hadronize into open heavy flavor mesons (e.g. D mesons) and baryons (e.g Λ_c), thus the measurements of these particles are crucial for understanding the properties of the QGP.

1.3 The ALICE detector

The ALICE apparatus is a highly sophisticated and comprehensive instrument designed to investigate the physics of strongly interacting matter at extreme energy densities, in particular the QGP. ALICE is specifically optimized for heavy-ion collisions but also conducts significant research using proton-proton and proton-lead collisions.

The study of the QGP properties requires to track charged particles down to very low momenta (about 80 MeV/c for pions [23]) in an environment characterised by a large number of charged particles produced in the collision. For these reasons detectors with high granularity and low material budget, such as the Time Projection Chamber (TPC) and the Inner Tracking System (ITS), were adopted. In addition, a key feature of ALICE is the possibility to determine the particles species in a wide momentum range (up to 20 GeV/c), using the information provided by different particle-identification (PID) detectors, and exploiting several techniques [23].

The ALICE detector is 16 m tall, 16 m wide and 26 m long, and weighs approximately 10 000 tonnes. It was designed and upgraded over almost three decades by a collaboration that currently includes over 2000 scientists and engineers from more than 160 institutes in 40 different countries. The experiment consists of 12 different detection systems, each with its own specific technology choice and design constraints [24]. A schematic of all ALICE detectors is shown in Figure 1.4.

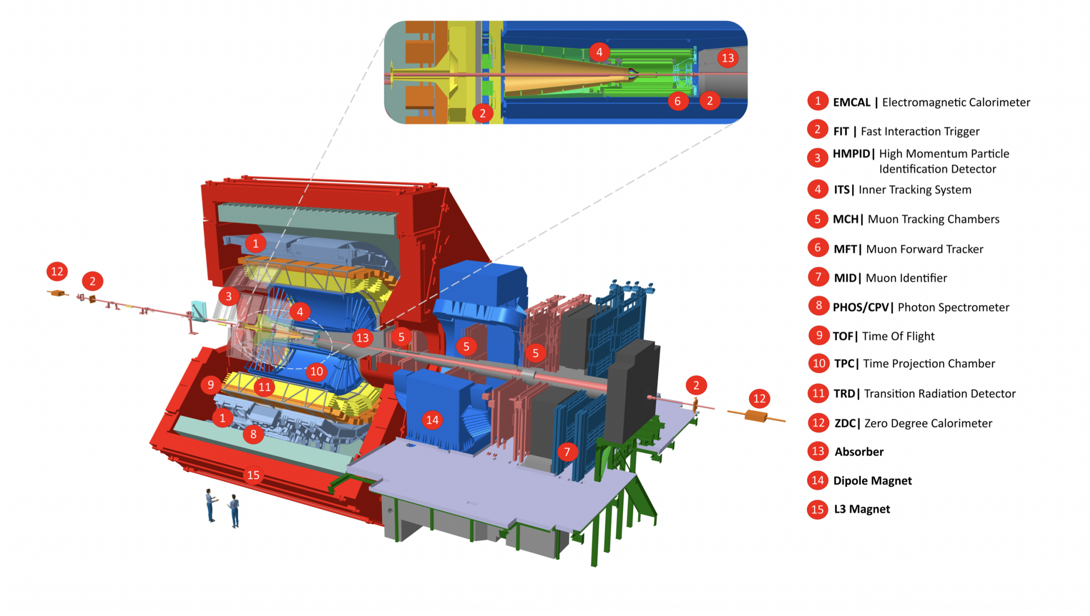

Figure 1.4: Schematic view of all ALICE detectors. Taken from [24].

It consists of a central part, which measures hadrons, electrons and photons, and a forward single arm spectrometer that focuses on muon detection. The central barrel part spans polar angles from 45° to 135° (angle from the beam direction) and is located inside a large solenoid magnet, with a maximum field of 0.5 T.

At the heart of ALICE is the Inner Tracking System (ITS), which provides high-resolution tracking of particles close to the interaction point, and is crucial for vertex reconstruction and identification of short-lived particles [25]. This system will be described more in detail in Section 1.3.1.

Surrounding the ITS is the Time Projection Chamber (TPC), the main device for pattern recognition, tracking, and identification of charged particles [26]. It is a 90 m^3 gas-filled cylinder with two drift regions separated by a central electrode, with a uniform electric field along the beam-axis. As charged particles pass through the TPC, they ionize the gas, causing electrons to drift towards the end plates where Gas Electron Multiplier (GEM) detectors amplify the signal. The TPC also provides particle identification through specific energy loss measurements in the gas.

The Transition Radiation Detector (TRD) is located outside the TPC and consists of multiple layers of radiators and drift chambers [27]. It provides additional space points for tracking, and the detection of transition radiation for electron identification [24].

The subsequent detector is the Time-of-Flight (TOF) system, which measures the time it takes for particles to travel from the interaction point to the detector. This information, combined with the path length and momentum of the particles, allows for accurate particle identification. The TOF system is composed of Multigap Resistive Plate Chambers (MRPCs) that provide excellent time resolution (80 ps) [28].

The High-momentum particle identification (HMPID) detector aims at enhancing the ALICE PID capabilities by identifying hadrons at $p_{\mathrm{T}} > 1$ GeV/c. It consists of seven modules of Ring Imaging Cherenkov (RICH) counters, able to detect Cherenkov photons emitted by fast charged particles traversing the radiator.

The Electromagnetic Calorimeter (EMCal) and the Photon Spectrometer (PHOS) are designed to measure the energy of photons and electrons. The EMCal covers a large area and provides information on the energy and spatial distribution of electromagnetic showers, playing a critical role in jet quenching studies. The PHOS, with its high granularity and resolution, is optimized for detecting low-energy photons and neutral mesons.

Additionally, ALICE features a Muon Spectrometer located at the far end of the experiment, which includes a complex arrangement of absorbers to remove hadrons and identify muons, a dipole magnet, and tracking chambers, enabling precise measurement of muons produced in the collisions. During Long Shutdown 2 a new addition to the muon detectors was installed: the Muon Forward Tracker (MFT), designed to improve the vertexing capabilities of the current detector [29]. It consists of tracking stations with the ALPIDE silicon pixel sensors: the same technology proposed for the concomitant upgrade of the ITS, described in detail in Section 1.3.1.

To complement these primary systems, ALICE also incorporates several other detectors and subsystems (ZDC, PMD, FMD, T0, V0) for global event characterization and triggering [30].

1.3.1 The Inner Tracking System

The ALICE experiment underwent a major upgrade phase during the LHC Long Shutdown 2 (LS2, from the end of 2018 to 2022). During this time the Inner Tracking System was replaced with a new detector, the current ITS2 [24][31]. This upgrade comprises seven cylindrical, concentric layers of silicon pixel detectors, based on Monolithic Active Pixel Sensors (MAPS), arranged around the beam pipe. The ITS2 spans an active surface of about 10 m^2, containing approximately 12.5 GPix with a pixel pitch of 29.24×26.88 μm^2. These features makes it the largest silicon pixel detector ever built: for comparison the STAR PXL detector at RHIC (Brookhaven National Laboratory - BNL), which was the first application of thin MAPS technology in a collider environment, covered a surface area of 0.16 m^2 with 356 MPix [32].

The ITS2 layout is shown in Fig. 1.5. The detector is divided into two main sections: the Inner Barrel (IB) and the Outer Barrel (OB). The IB consists of the innermost three layers, positioned close to the beam pipe. These layers are characterized by a very low material budget of 0.36% X_0 per layer. The OB includes two middle layers and two outer layers, maintaining a material budget of around 1.1% X_0 per layer.

The radii of the inner, middle and outer layers range from 23 to 393 mm and their lengths are 30 cm, 90 cm and 150 cm, respectively.

The ITS2 design consists in a modular structure where sensors are mounted on staves (see Figure 1.6). Each stave is composed of a lightweight carbon fiber support (Space Frame), a thermally conductive carbon plate with embedded water cooling pipes (Cold Plate), ALPIDE pixel sensors (see next paragraph for more details), and a flexible printed circuit board for sensor readout, control, and power supply. These staves are arranged with slight overlaps to ensure full azimuthal coverage, forming a hermetic half-barrel that is combined to create a full barrel.

The material budget and the distance from the interaction point are two parameters that influence the pointing resolution of a tracking system.

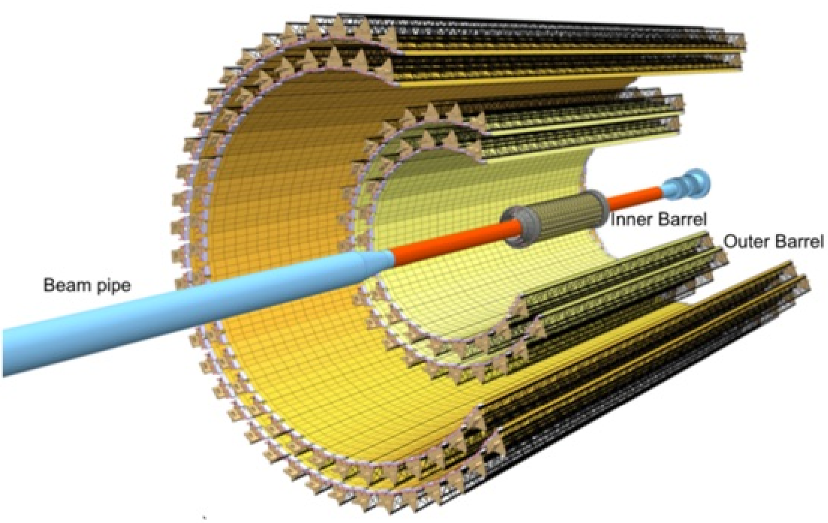

Figure 1.5: Schematic view of the Inner Tracking System currently installed in ALICE. Taken from [31].

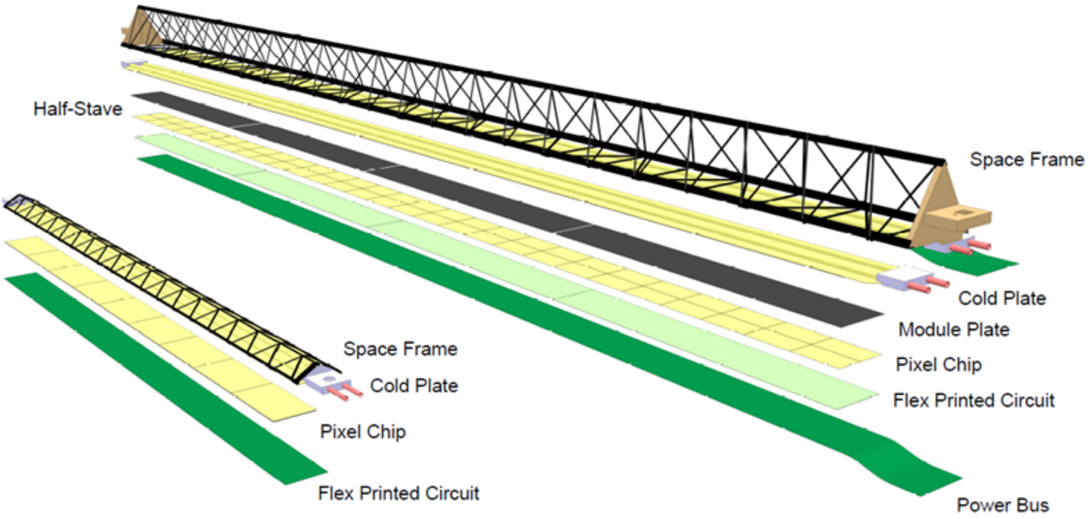

Figure 1.6: Schematic drawing of the IB (left) and OB (right) staves. Taken from [31].

The pointing resolution is given by the sum in quadrature of two contributions (Equation 1.1): the intrinsic one, which is given by the intrinsic spatial resolution σ_i and position r_l of the detector elements l; and the uncertainty σ_p^{ms} introduced by multiple

Coulomb scattering occuring in the beam pipe and in the detector layers (especially the one closest to the interaction point).

$$\sigma_p = \sigma_p^i \oplus \sigma_p^{ms} \tag{1.1}$$

For a configuration of two layers the intrinsic resolution is defined as [33]:

$$\sigma_p^i = \sqrt{\left(\frac{r_2}{r_2 - r_1}\sigma_1\right)^2 + \left(\frac{r_1}{r_2 - r_1}\sigma_2\right)^2} \tag{1.2}$$

While the multiple scattering contribution is given by:

$$\sigma_p^{ms} \approx r_1 \theta_{RMS} \tag{1.3}$$

θ_{RMS} is the RMS of the Gaussian that describes the distribution of the angular deflection due to scattering [34], which is described by the following equation:

$$\theta_{RMS} = \frac{13.6[\mathrm{MeV}]}{\beta cp} z \sqrt{\frac{x}{X_0}} \left[1 + 0.038 \ln \frac{x}{X_0}\right] \tag{1.4}$$

where p, βc, and z are the momentum, velocity and charge of the incident particle, and x/X_0 is the thickness of the material in terms of radiation length X_0.

This dependecy indicates that a better pointing resolution can be achieved by minimizing the inner radii (r_1) and the material budget (x/X_0), especially for the innermost layers.

The ITS upgrade; with an improved spatial resolution of the sensors, a thinner and lighter inner tracker, and a first layer closer to the interaction point; improves the pointing resolution by a factor of 3 in the transverse direction and a factor 6 in the longitudinal direction. This provides more effective suppression of backgrounds in the reconstruction of decays of heavy-flavour mesons and baryons as well as in the dielectron emission measurements.

Moreover, ITS2 is able to handle higher collision rates, capable of recording Pb-Pb collisions at up to 100 kHz (ITS featured a maximum read-out rate of 1 kHz) and p-p collisions at up to 400 kHz. The increased readout rate leads to improved statistical precision for all measurements, even in the presence of large backgrounds.

The ALICE Pixel Detector

The ALice PIxel DEtector (ALPIDE) is the sensor developed for the ITS2 upgrade. It is a Complementary Metal Oxide Semiconductor (CMOS) Monolithic Active Pixel Sensor (MAPS) fabricated in 180nm TowerJazz technology [35]. A photograph of the ALPIDE chip is shown in Figure 1.7. It measures 15 mm × 30 mm and contains a matrix of 512 rows and 1024 columns of pixels, each one measuring 29.24×26.88 µm^2. The chip contains a peripheral region of 1.2×30 mm^2 in which analog biasing, control, readout and interfacing functionalities are implemented.

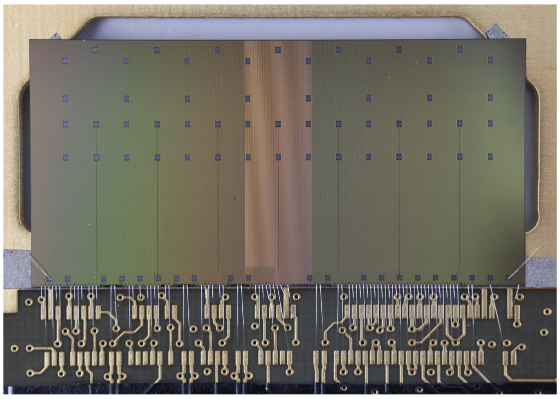

Figure 1.7: Photograph of the ALPIDE chip. Taken from [24].

Each pixel cell contains a sensing diode, a front-end amplifier and a shaping stage, a discriminator and a digital section. The in-pixel multiple-event memory is read out asynchronously by means of priority encoder circuits. This is both fast and power efficient as the expected occupancies are low and only hit pixels are read out in a hit-driven fashion [36]. This approach results in a very low power consumption: around 40 nW for the single pixel, with a total power density of about 47 mW/cm^{-2} [24].

An innovative feature of the ALPIDE design is the presence of a deep p-well (shown in Figure 3.10) which allows PMOS transistors to be fabricated on a p-type epitaxial layer without penalizing the charge collection, by shielding their n-well from the epitaxial layer [37][38] (see Section 3.4). This innovation allows for a more complex in-pixel circuitry, thanks to which ALPIDE is not limited to the traditional rolling shutter readout [38][39].

Another significant advantage is the use of high-resistive (> 1 kΩ cm) epitaxial layers, which allows for an improved charge collection performance. Additionally, the TowerJazz process allows the application of a moderate negative bias (up to 6 V) to the substrate, also referred to as back-bias. This voltage further depletes the high resistivity epitaxial layer, making the charge collection process faster, as explained in detail in Section 3.1.2.

The sensor technologies developed by ALICE for the ITS2 detector are now being used or considered for other applications in high-energy physics and beyond, such as the vertex detector of the sPHENIX experiment at RHIC [40].

Chapter 2

ITS3

During the next Long Shutdown period of the LHC (LS3, from 2026 to early 2029), the three innermost layers of ITS2 will be replaced with a novel vertex detector called ITS3, consisting of curved wafer-scale ultra-thin silicon sensors arranged in truly cylindrical layers.

This upgrade will achieve significant improvements by reducing the material budget to an unprecedented value of 0.07% X_0 per layer. Furthermore, the innermost layer will be positioned just 19 mm from the interaction point and only 2 mm from the beam pipe.

Thanks to the reduction of the material budget and its closeness to the interaction point, the ITS3 detector will provide unprecedented spatial resolution, improved by a factor 2 compared with the one of the current ITS detector, and a higher efficiency for the track reconstruction of low-momentum particles.

2.1 A novel vertex detector

An analysis of the material budget of ITS2 reveals that further optimization is possible. Figure 2.1 depicts the azimuthal distribution of the material budget of an ITS2 layer: an inhomogeneous distribution over the azimuth is visible. More importantly it can be observed that the main contributions come from electrical substrate, mechanical support structures and the cooling systems, which add considerable mass and complexity. By simplifying the detector to predominantly silicon components, the material budget can be significantly reduced by a factor 5, achieving a total value below 0.07% X_0.

The realization of such detector requires several progressive strategies, some of which are unprecedented in High Energy physics.

2.1.1 Low-speed air-flow cooling

To ensure a stable operation the sensor's operating temperature must be under 30°C. A cooling system is essential to dissipate the heat generated by the sensors and guarantee

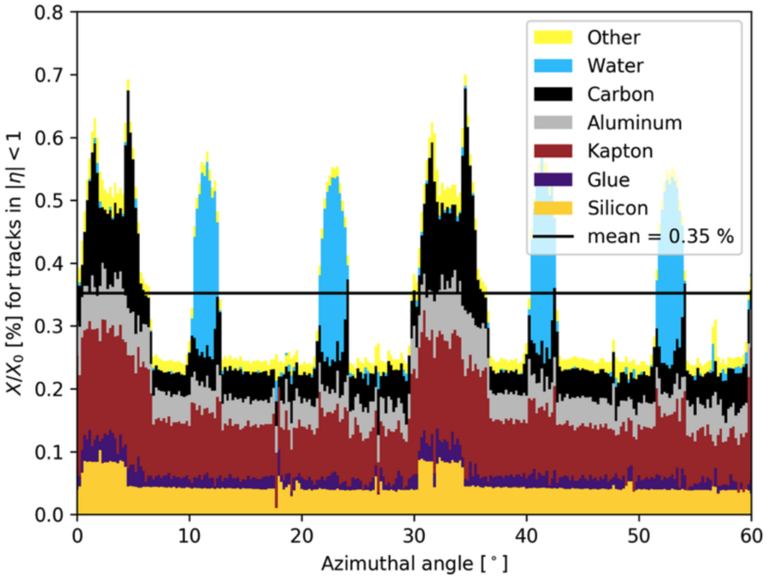

Figure 2.1: Azimuthal distribution of the material budget of ITS2 layer 0 averaged over $|\eta| < 1$. Taken from [41].

these temperature conditions. Simultaneously, it is important to minimize the material budget. The most suitable method that can satisfy both these requirements is a low-speed air-flow cooling system. This allows to remove the produced heat by convection while keeping the vibrations of the sensor smaller than the intrinsic spatial resolution.

Additionally, to enhance the heat exchange in the region of the chip periphery (where the power consumption is higher), carbon foam half-rings are included. They have a double functionality as they act as both thermal and structural parts of the detector.

Carbon foam with high thermal conductivity is used for the half-rings located at the A-side's high power dissipation region. Carbon foam with lower density and slightly worse thermal properties is used for support purposes only, i.e. for the half-rings on the C-side and the longerons running along the sensor's long edges.

Figure 2.2 shows an Engineering Model (used for design developments) manufactured during the R&D phase to simulate the mechanical structure of ITS3.

Experimental tests showed that with an average airflow freestream velocity between the layers of about 8 m/s, the detector can be operated at a temperature of 5° above the inlet air temperature, with an uniformity along the sensor kept within 5°C [42].

The surface power density of the matrix and end-cap regions are 25 mW/cm^2 and 1000 mW/cm^2, respectively; but the conditions above will be respected even if higher power dissipation values are reached in the matrix region (< 50 mW/cm^2 average).

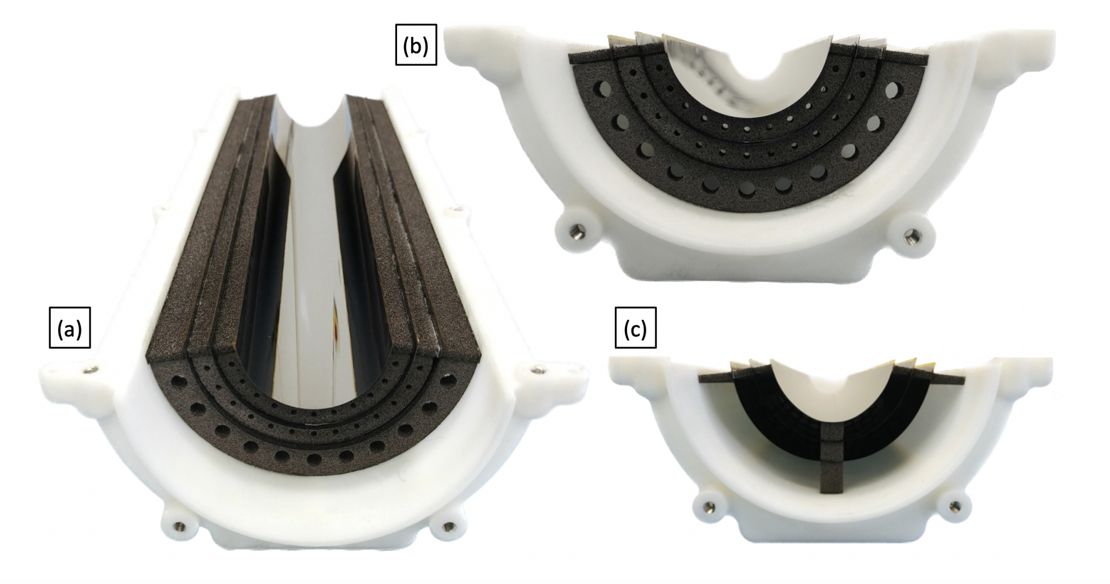

Figure 2.2: Engineering Model of ITS3. (a) Perspective, (b) A-side and (c) C-side views of the prototype. Three wafer-size blank silicon pieces (40 µm thin, 280 mm long), simulating the half-layers are kept bent by half-rings (A-side), longerons and wedges (C-side) made from carbon foam. Taken from [42].

The short-term stability of the sensor, which must be < 2 µm to be smaller than the sensor resolution, was tested as well. The results predicted a value within 1.3 µm, compatible with the requirement [42].

2.1.2 Bent silicon

The bending of silicon sensors allows for the near-total elimination of mechanical support structures. The idea is to make use of the flexible nature of thin silicon by reducing the sensor thickness to 50 µm, then bend the sensors to the target radii (19, 25.2 and 31.5 mm) and mechanically support them using the carbon foam spacers.

The bending procedure was tested with different techinques and at different radii using ALPIDEs and no degradation in performance was observed [43]. Similar studies were performed on the smaller prototypes designed for the validation of the 65 nm CMOS technology (Section 2.1.4), confirming that the bending does not significantly alter the performance of the chips [42].

2.1.3 Stitching

Stitching is a technology that enable the creation of wafer-scale sensors, and is capable of covering the entire active area of the half-barrels. In standard CMOS processes, the reticle size is limited by the lithographic field of view, typically covering areas of $\sim 2 \times 3\text{cm}^2$. The reticle is simply stepped and repeated across the wafers to create multiple identical images of the same circuit or group of circuits. Instead of producing individual chips of this reticle size, separated by thin areas of unused silicon, stitching allows the connection of otherwise unconnected reticles on a wafer already at wafer production stage. During production, selected parts of the reticle, the repeated sensor units (RSU), are placed next to each other on the wafer to create a segment. At the two short edges of each segment, the design is completed with the stitching of end-cap frames, the left end cap (LEC) and the right end cap. In the layout of the ALICE experiment, the left end cap of the sensor is located on the A-side of the apparatus and the right end cap on the C-side. The electrical interconnections to the external systems are made via pads located in the left and right end cap. The power supply needs to be from both edges, while the signalling interfaces are only on the LEC.

In order to provide sensor sizes adapted to the three ITS3 layers, three, four or five sensor segments, respectively, are diced out from the wafer and form the corresponding half barrels (a visualisation of this stitching plan is shown in Figure 6.2). In this way, wafer-scale sensors can be manufactured.

The concept diagram of a stitched prototype is shown in Figure 2.3.

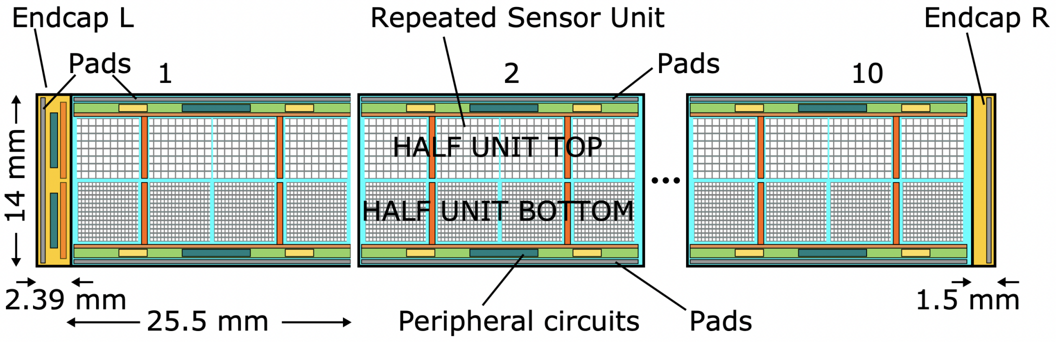

Figure 2.3: Concept diagram of the MOSS chip. Taken from [42].

Two prototypes were designed to validate the stitching technology for the ITS3 application: the MOnolithic Stitched Sensor (MOSS) and the MOnolithic Stitched Timing

(MOST). They consist of 10 units stitched together for a total length of about 260 mm. A smaller version of the MOSS prototype was produced as well, called baby-MOSS, which maintains the same functionalities but consists of only one unit (1/10th in size). An overview on this development is presented in Chapter 6.

2.1.4 65 nm imaging process

To take advantage of commercially available 300 mm wafer sizes, the chips for the ITS3 are going to be produced using the 65 nm TPSCo CMOS imaging process [35]. Compared to the 180 nm technology used for the ALPIDE chip, the 65 nm process offers lower power consumption, which is crucial for enabling air-cooling, and higher integration density, which provides opportunities for implementing in-pixel signal processing. Transitioning to a 65 nm process requires a technology qualification phase, dedicated to process optimisation and quantification of performance parameters with respect to charge collection. The dependence of the sensitivity on pixel pitch, pixel design and radiation level was assessed. Process modifications were introduced to optimise the sensor for charge collection for particle detection, detailed in Section 4.1, based on general principles already applied for the optimisation of designs in the 180 nm technology.

The first production of these prototypes is referred to as the 'Multi Layer Reticle 1 (MLR1) submission' and consists of several different test structures. Among these, three different pixel test structures were extensively characterised for ITS3, their characteristics are summarized in Table 2.1. The first one, called Analogue Pixel Test Structure (APTS), contains a matrix of 4×4 pixels optimized for a detailed characterisation of the analogue signal output. The second one is the Circuit Exploratoire 65 (CE65), which houses a pixel matrix with different pixel architectures dedicated to the investigation of different sensing node geometries as well as different amplification schemes. And finally, the Digital Pixel Test Structure (DPTS) which consists of 32×32 pixels and contains a full in-pixel circuitry and a dedicated digital readout scheme.

Name	**Matrix**	**Pixel pitch [µm]**	**Readout**
APTS	4×4	10, 15, 20, 25	analogue
CE65	64×32	15	rolling shutter analogue
	48×32	25	
DPTS	32×32	15	asynchronous digital

Table 2.1: Characteristics of the MLR1 test structures developed for ITS3.

This thesis will focus mainly on the characterization of the APTS: its characteristics and a comprehensive set of measurements are described in detail in Chapter 4, while a simulation study of its charge collection performance is presented in Chapter 5.

2.2 Detector Layout

The concept of this novel detector relies on cylindrical, bent silicon layers. The design will feature two sections, referred to as half-barrels, enabling the detector to be mounted around the beam pipe. Each half-barrel will comprise three separate half-layers. The half-layers will consist of a single large pixel chip curved to a cylindrical shape.

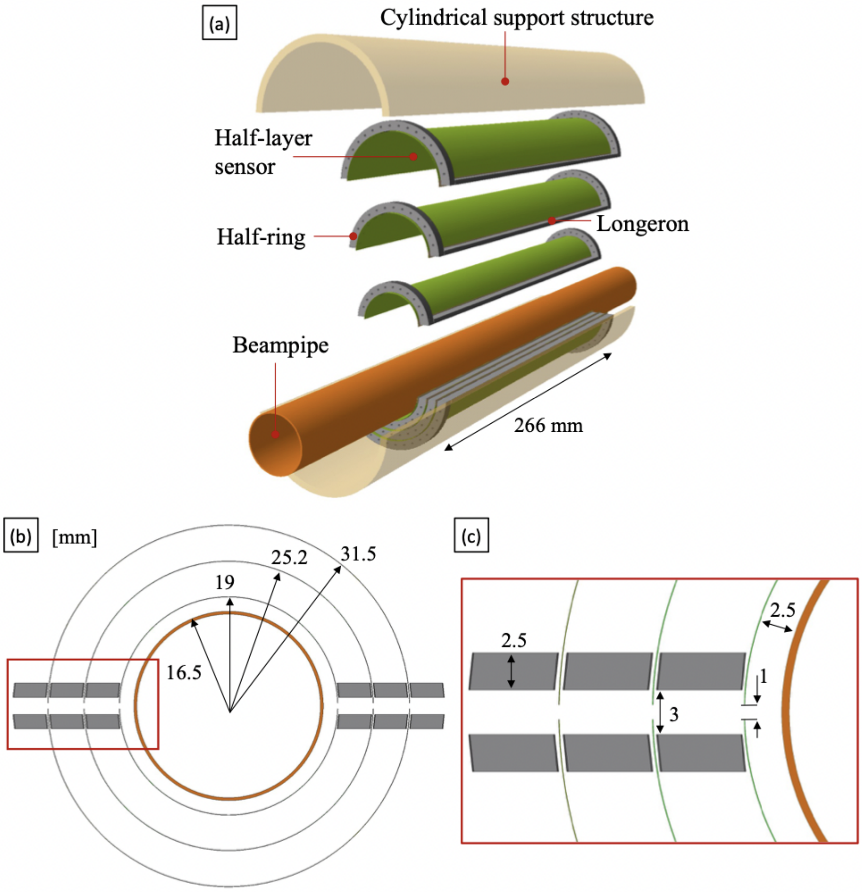

Figure 2.4: Simplified ITS3 Detector layout, (a) 3 top and 3 bottom half layers around the beam pipe within the cylindrical support structure supported by carbon foam half-rings and longerons, (b) radial distance of beam pipe and layers 0, 1, 2, (c) zoom of supporting carbon foam structures. Taken from [42].

A sketch of this structure is shown in Figure 2.4 and the parameters associated with each layer are reported in Table 2.2.

Layer parameter	**Layer 0**	**Layer 1**	**Layer 2**
Radial position (mm)	19.0	25.2	31.5
Length (sensitive area) (mm)		260	
Pixel sensor dimensions (mm^2)	266 × 58.7	266 × 78.3	266 × 97.8
Pixel size (µm^2)		20.8 × 22.8	

Table 2.2: Geometrical parameters of ITS3 Layers.

The outermost layer is attached to an external CYlindrical Structural Shell (CYSS), which provides the main mechanical support to the entire assembly.

The half-detector presents a mechanical interface for the connection to the service support structure and power/data connectivity at the A-side. From here, power lines along the CYSS connect to the C-side FPCs (see Figure 2.5).

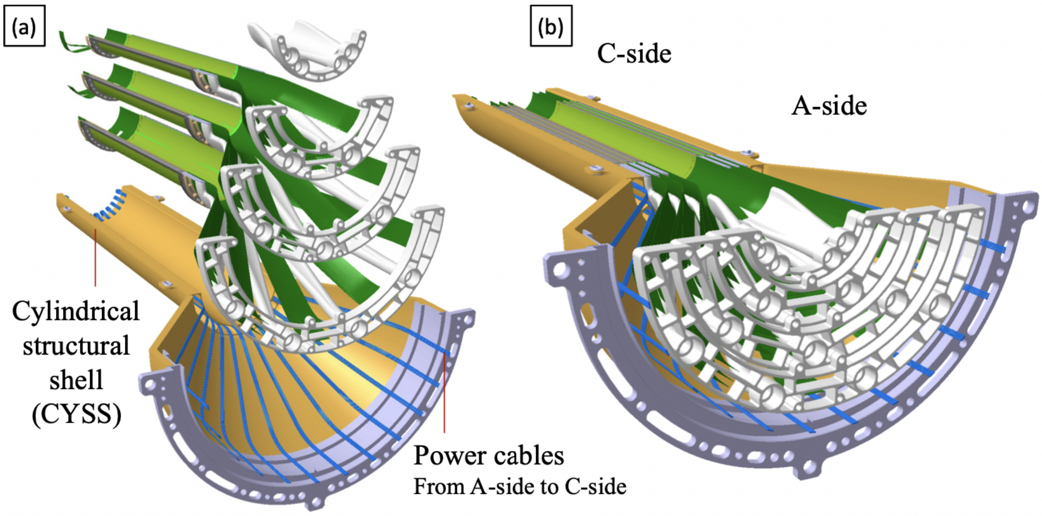

Figure 2.5: Half-detector: (a) Exploded and (b) assembled view. Taken from [42].

2.3 Physics performance

The improved vertex resolution and reduced material budget of ITS3 will be beneficial for several physics measurements. In particular, it will significantly extend the physics capability for the study of heavy-flavour production, notably in the baryon sector, and for the study of low-mass dielectrons. Extensive discussions of the ITS3 physics goals and the achievable performance for several observables can be found in the Expression of Interest (EoI) [44], Letter of Intent (LoI) [41], and most recently in a dedicated ALICE Public Note [45].

In order to quantitatively assess the impact ITS3 will have on the ALICE physics programme, this section will outline the expected improvements in performance for the measurements of the Λ_c and thermal dielectrons. Additionally, it will provide the simulated tracking performance of ITS3 in comparison with ITS2.

2.3.1 Tracking performance

A simulation was conducted to assess the pointing resolution and tracking efficiency as functions of transverse momentum using both a Fast Analytic Tool (FAT) and a full Monte Carlo (MC) simulation [42].

An important parameter to evaluate the capability of a vertex detector to separate secondary vertices of heavy-flavour decays from the interaction vertex is the track impact-parameter resolution, which is defined as the dispersion of the distribution of the Distance of Closest Approach (DCA) of the reconstructed (primary) tracks to the interaction vertex.

The comparison of the impact parameter resolution in the transverse plane is shown in the left plot of Figure 2.6. An improvement by a factor of 2 across most of the momentum range is visible with ITS3. Additionally, the tracking efficiency, illustrated in the right plot of Figure 2.6, shows a more significant enhancement at low transverse momenta ($p_{\mathrm{T}} < 100$ MeV/c). Improving the pointing resolution and tracking efficiency at low transverse momenta allows for a clear separation of the secondary vertex from the primary vertex even for short-lived particles decays [46]. The capabilities in resolving secondary vertices are fundamental for the measurement of heavy-flavour hadrons based on their decay topologies.

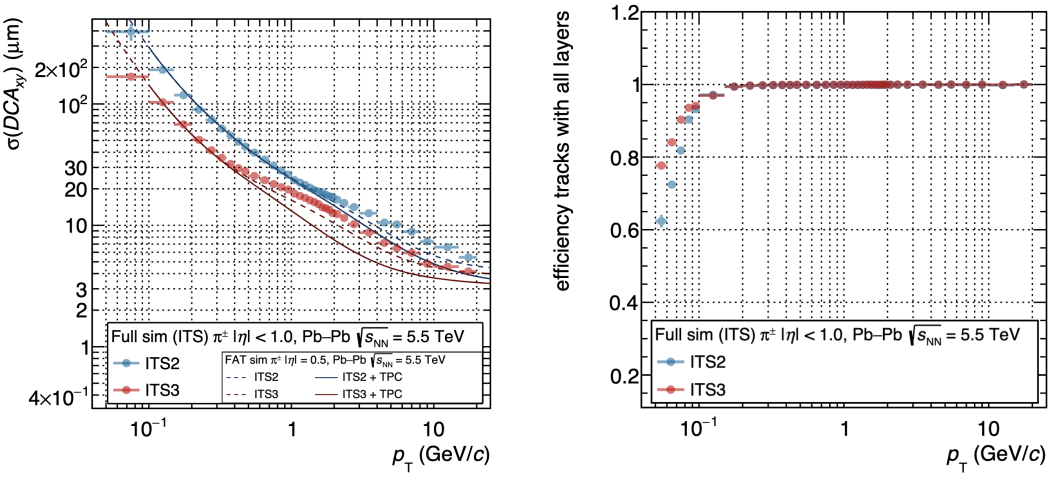

Figure 2.6: (left) Impact parameter resolution and (right) tracking efficiecy as a function of the transverse momentum for ITS2 (blue) and ITS3 (red) in the transverse plane. Dashed lines show the results with ITS only, solid lines show the results with ITS+TPC. The lines represents the results obtained with a fast analytic tool, while circles show the results obtained with full MC. Taken from [42].

2.3.2 Measurement of Λ_c

The measurements of heavy-flavor baryons is crucial for the study of the hadronization mechanisms of heavy quarks (i.e. charm and beauty quarks) from the QGP medium. In fact, if heavy quarks hadronize via recombination with light quarks close in space and momentum from the deconfined medium, an enhancement of the relative abundance of charm and beauty baryons compared to mesons in heavy-ion collisions with respect to proton-proton collisions, where an extended QGP phase is not formed, is expected. The hadronization via recombination is expected to happen mostly at low and intermediate momentum region (below 10 GeV/c), where the heavy quarks undergo a diffusion motion in the QGP and possibly reach at least partial thermal equilibrium via multiple low-momentum transfer interactions with the medium constituents [47].

Initial measurements by ALICE [48], CMS [49], and STAR [50] suggest a possible modification of the p_{T} distribution of the Λ_c/D^0 ratio for $p_{\mathrm{T}} < 10$ GeV/c, but these measurements have a limited statistical precision (error of around 30% [51]). The ITS3 upgrade aims to address the challenges of this measurement.

The measurement of the Λ_c is based on its decay topologies, and the primary challenge is its short lifetime ($c\tau$ = 59 µm). This requires very precise tracking and impact parameter resolution, because the decay tracks are typically displaced from the main interaction vertex by only a few tens of microns. The ITS3 upgrade aims to address this, promising improved measurement capabilities for Λ_c via channels such as $\Lambda_c^+ \rightarrow \mathrm{pK}^-\pi^+$.

ITS3 performance studies were carried out using the same method used for ITS2 in [31] but corrected for ITS3 resolutions (Figure 2.6). The comparison of performances between ITS2 and ITS3 is shown in Figure 2.7, where statistical significance $\mathrm{S}/\sqrt{S+B}$ and signal-to-background S/B are shown as a function of p_T for the decay channel. Where S an B are the signal and background yields in an invariant-mass range of $\pm 3\sigma$ around the Λ_c mass, where σ is the invariant-mass resolution [45].

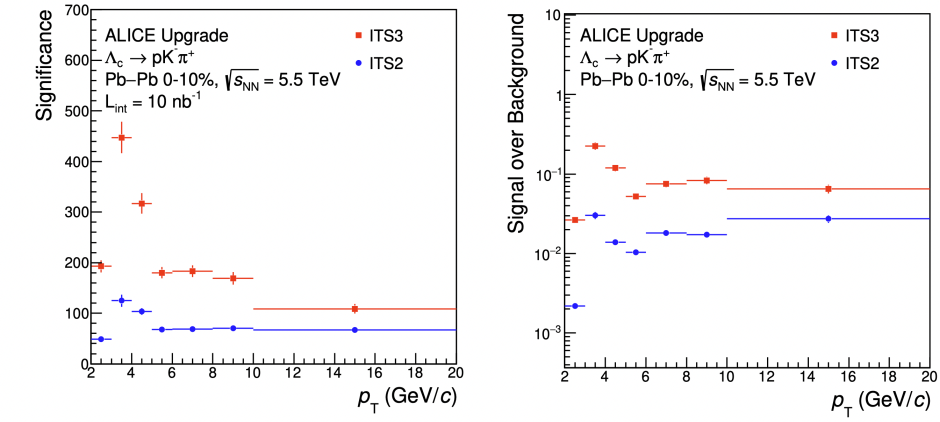

Figure 2.7: $\Lambda_c \rightarrow \mathrm{pK}^-\pi^+$ in central Pb-Pb collisions at $\sqrt{s_{NN}}$ = 5.5 TeV: statistical significance (left) and signal-to-background ratio (right). Taken from [45].

This results show an improvement of a factor 4 for the significance and of a factor 10 for the S/B ratio, which is due to the better pointing resolution and consequent larger rejection of combinatorial background.

The large improvement of the significance at low p_T with ITS3 will also impact the quarkonium (hadrons formed by quark and anti-quark with the same flavour) studies. For instance, in order to measure the total $c\bar{c}$ production cross section it is necessary to measure the production of all the single charm hadron species, including the charmed baryons [52]. For this reason, it is crucial to have a precise determination of the p_T-integrated Λ_c production yield down to $p_\mathrm{T} = 0$.

2.3.3 Measurement of thermal dielectrons

Electromagnetic radiation produced in heavy-ion collisions can be detected using direct photons with low momentum or virtual photons yielding low invariant-mass dilepton pairs. The measurement of dielectron pairs in the ALICE central barrel requires acceptance for e^+e^- pairs at invariant masses and transverse momenta as low as possible, at least at $M_{ee} \approx p_{\mathrm{T,ee}} \approx T \approx 150$ MeV, which implies electron detection down to $p_{\mathrm{T}} < 100$ MeV/c [41]. An accurate electron identification is crucial due to the low production rate of thermal dileptons, because it suppresses significant background from hadron misidentification and photon conversions.

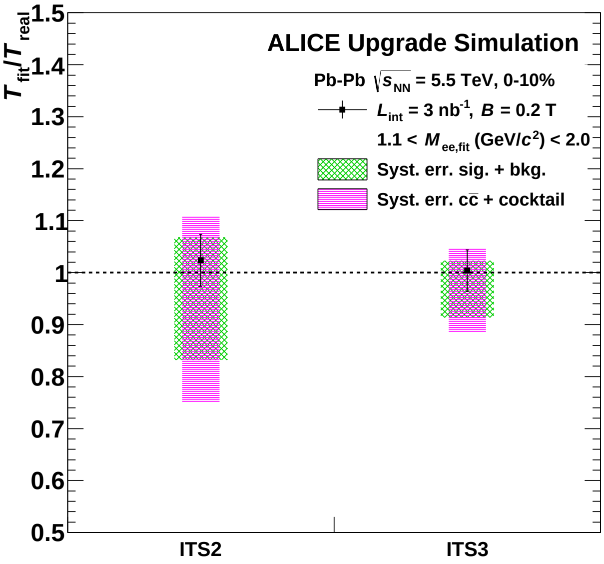

ALI-SIMUL-306864

Figure 2.8: Expected relative uncertainty of the extraction of the T parameter from a fit to the invariant mass excess spectrum in $1.1 < M_{ee} < 2.0$ GeV/c^2. The results are shown for the ITS2 and ITS3 scenarios, with a tight cut on the quadratic sum of the impact parameters of the lepton pair. Error bars show the statistical uncertainties. The green boxes show the systematic uncertainties from the combinatorial background subtraction, the magenta boxes indicate systematic uncertainties related to the subtraction of the charm-decay electron contribution. Taken from [41].

The ITS3 upgrade will be beneficial for the thermal dielectrons measurement for the following reasons:

- Material budget reduction, which will cut electron backgrounds from photon conversions by a factor of about three.
- Improved low-p_{T} tracking capability, which helps reduce combinatorial background.
- Improved pointing resolution, which enables efficient tagging of electrons from semi-leptonic charm decays and reduces the charm background by a factor 2.

All these improvements decrease systematic uncertainties and enhance the precision of dielectron measurements. In Figure 2.8 a comparison of the systematic uncertainties between ITS2 and ITS3 is shown.

This plot was obtained applying an exponential fit to the simulated invariant mass spectra in the region $1.1 < M_{ee} < 2.0$ GeV/c^2, and comparing the relative uncertainty of the fit parameter extraction. The ITS3 upgrade is expected to reduce statistical uncertainty by 1.3 times and systematic uncertainties from background subtraction by a factor 2 [41].

2.3.4 Complementarity with other LHC experiments

ATLAS and CMS are expected to achieve, after their upgrades planned for LS3 [53–56], a performance for the low-momentum tracking and vertexing close to that of the ALICE detector before the LS2 upgrade. Regarding the particle identification capabilities for charged hadrons, with the combination of the TPC and TOF information, the ALICE experiment will maintain its superior performance. Antoher key aspect is that, while other experiments select the events by means of a trigger reducing the event rate, ALICE will be able to inspect practically all heavy-ion collisions, which is important for measurments that rely on the inspection of high event statistics.

In Table 2.3 a summary of the major LHC vertex detectors operating during Run 4, their sensor technology, material budget per layer, innermost layer radius (r_{IB}) and impact parameter resolution σ_d at $p_{\mathrm{T}} = 1$ GeV/c is shown.

It is evident from this considerations that ALICE is essential for many measurements in heavy-ion collisions due to its unique capabilities. Firstly, the measurement of low-p_{T} dileptons, which is uniquely accesible by ALICE ITS2 and that can be substantially improved with the ITS3. But also for the measurement of charmed and beauty hadrons, which can be precisely measured at very low-p_{T} ($p_{\mathrm{T}} < 2$ GeV/c and $p_{\mathrm{T}} < 5$ GeV/c, respectively) only by ALICE. The ATLAS and CMS experiments will measure these observables at higher p_{T} values, as recently described in [62]. The Λ_c production was measured by the CMS experiment for $p_{\mathrm{T}} > 10$ GeV/c in Pb-Pb collisions [63]. The

Vertex detectors	**Material budget** [$\%X_0$]	**r$_{IB}$ [mm]**	$\sigma_{d,p_{\mathbf{T}}=1\ \mathbf{GeV}/c}$ **[µm]**
ALICE ITS3 (MAPS)	0.07	19	10
CMS Phase-2 (Hybrid pix. and strips) [53]	∼2	29	∼50
ATLAS ITk (Hybrid pix. and strips) [54–58]	∼2	33	∼70
LHCb VELO (Hybrid pixels) [59–61]	∼0.94	5	∼30

Table 2.3: Summary of LHC vertex detectors and their features.

LHCb experiment might be able to measure these observables at forward rapidity, but the tracking performance for central Pb-Pb collisions was not yet studied.

Chapter 3

Monolithic Active Pixel Sensors

In the 1980s, the advent of semiconductor-based sensors and highly integrated CMOS (Complementary Metal-Oxide-Semiconductor) based readout electronics revolutionized particle detection, in particular vertexing and tracking detection systems. This technology addressed many of the stringent requirements of HEP detectors, such as granularity, material thickness, read-out speed, power consumption, and radiation hardness [64]. The rapid advancement of the semiconductor industry continues to drive technological innovations [65].

The first widely used silicon-based devices were silicon strip detectors [66], which provided a good spatial resolution but could only measure one-dimensional tracking.

Hybrid pixel detectors emerged in the 1990s, consisting of separate sensor and readout electronics layers (see Figure 3.9(a)). These detectors are characterised by excellent radiation hardness and high spatial resolution, making them well-suited for the extreme environments near the interaction points. For this reason they are widely employed in experiments like ATLAS and CMS, enabling precise particle tracking in harsh environments [67]. However, they require complex techniques to interconnect the sensor and the readout electronics.

To go beyond these limitations and build detection systems with higher granularity and less material thickness, one solution is to merge sensor and read-out electronics into a single piece of silicon. This is the approach taken with Monolithic Active Pixel Sensors (MAPS), a technology capable of reducing material thickness and costs while improving the tracking performance.

This chapter serves as an introduction to the fundamental principles of semiconductor physics, with a particular focus on the key characteristics and behavior of silicon detectors. In addition, it delves into the operational principles of MAPS, offering an overview of their underlying mechanisms and functional properties.

3.1 Silicon properties

3.1.1 Band structure

Silicon is a semiconductor material with atoms arranged in a crystalline lattice. The periodic lattice of crystalline materials establishes the allowed energy bands for electrons that exist within that solid. The energy of any electron within the pure material must be confined to one of these energy bands that are separated by ranges of forbidden energies called "gaps" [68].

A schematic of the band structrure of a semiconductor is shown in Figure 3.1. The low-energy band is the valence band, where the electrons are bound to the atoms. The high-energy band is the conduction band, where the electrons are free to move and conduct electricity. The separation between these two bands, known as the band gap, is a key determinant of a material's behavior. For silicon, this band gap is $E_g = 1.12$ eV at room temperature (300 K) [69], placing it in the category of semiconductors. This relatively small band gap allows electrons to be thermally or electrically excited from the valence band to the conduction band, leaving behind a vacant orbital called "hole" in the valence band. Both the electrons in the conduction band and the holes left behind in the valence band contribute to the electrical conductivity.

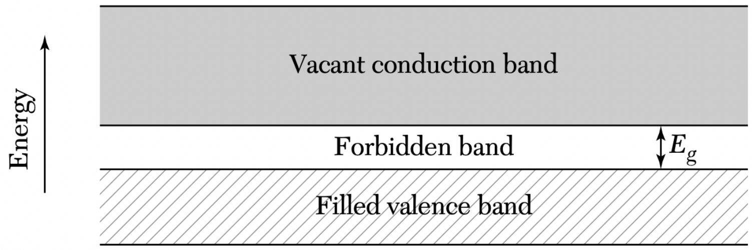

Figure 3.1: Band scheme for intrinsic conductivity in a semiconductor. At 0 K the conductivity is zero because all states in the valence band are filled and all states in the conduction band are vacant. As the temperature is increased, electrons are thermally excited from the valence band to the conduction band, where they become mobile. Taken from [70].

In intrinsic (pure) silicon, the concentration of electrons n in the conduction band is equal to the concentration of holes p in the valence band [71]:

$$n = p = n_i \tag{3.1}$$

where n_i is the intrinsic carrier density.

Electrons are constantly being thermally excited, but some of them can recombine. Under stable conditions, there is an equilibrium between the two processes and the concentration n_i is proportional to $\mathrm{T}^{3/2}e^{-\mathrm{E}_g/2\mathrm{kT}}$, where k is the Boltzmann constant and T is the absolute temperature [72].

3.1.2 Doping and junctions

The electrical properties of semiconductors can be modified by introducing impurities into the crystal lattice that add additional energy levels between valence and conduction band. The controlled insertion of impurities close to the two bands is referred to as doping.

There are two types of doping: n-type and p-type. The n-type introduces atoms with more valence electrons than silicon (called donors e.g. Phosphorus). Because they are not part of the regular lattice, the extra electrons associated with donor impurities can occupy a position within the normally forbidden gap. These very loosely bound electrons will have an energy near the top of the gap. The energy spacing between these donor levels and the bottom of the conduction band is sufficiently small so that the probability of thermal excitation is high enough to ensure that a large fraction of all the donor impurities are ionized.

The p-type introduces atoms with less valence electrons than silicon (called acceptors e.g. Boron). These acceptor impurities create electron sites near the bottom of the gap. Because the energy difference between typical acceptor sites and the top of the valence band is small, a large fraction of all the acceptor sites are filled by thermally excited electrons. To a good approximation, an extra hole is created in the valence band for every acceptor impurity that is added.

A schematic of the energy band structure for doped silicon with the corresponding doping levels created in the bandgap is shown in Figure 3.2.

In thermal equilibrium, the concentration of positive and negative charge carriers is constant in time and follows the mass action law [72]:

$$n \cdot p = n_i^2 \tag{3.2}$$

which says that the product of the concentration of electrons and holes is equal to the square of the intrinsic carrier density and it is not altered by doping. In n-type silicon electrons are majority and holes minority carriers, while in p-type silicon electrons are minority and holes are majority carriers.

A locally restricted placement of dopants in a bulk material is referred to as implant. Implants are often characterised by a high doping concentration, which is indicated by

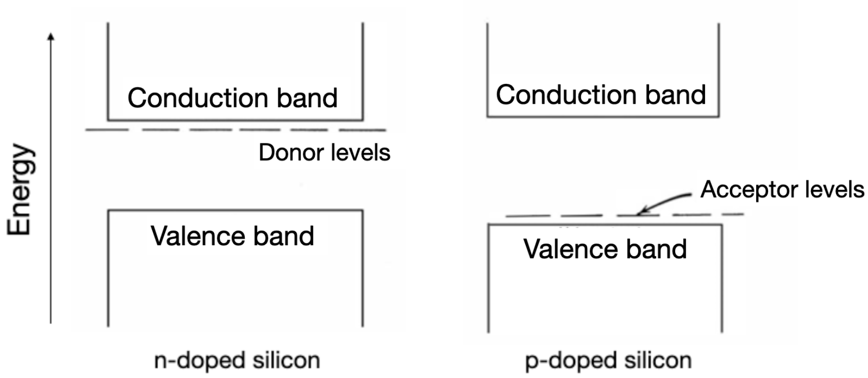

Figure 3.2: Band scheme for doped silicon, with the corresponding donor/acceptor levels created in the silicon bandgap. Adjusted from [73].

the symbols n^+ or p^+.

Doping can significantly affect the silicon properties. For instance the carrier mobility, discussed more in detail in Section 3.1.3, can be reduced due to the increased scattering from ionised impurities. Consequently, the resistivity is also influenced, as it is directly dependent on carrier mobility:

$$\rho = \frac{1}{e(n\mu_e + p\mu_h)} \tag{3.3}$$

where e is the elementary charge, μ_e and μ_h are electron and hole mobilities (1350 and 480 $\mathrm{cm}^2/(\mathrm{V}\cdot\mathrm{s})$ respectively [70]), and n and p are negative and positive charge carrier concentrations.

When a p-type and a n-type region are brought together, a p-n junction is formed. At the interface of these two regions, electrons from the n-type region diffuse into the p-type region and recombine with holes, while holes from the p-type region diffuse into the n-type region and recombine with electrons. This diffusion process creates a depletion region, a zone devoid of free charge carriers, near the junction interface. In Figure 3.3 the p-n junction structure is depicted, together with its internal space charge, electric field and potential.

In the depletion region, the immobile ionized donor atoms in the n-type region and the ionized acceptor atoms in the p-type region create an electric field. This electric field diminishes the tendency for further diffusion, establishing a balance known as the built-in potential or barrier voltage. This potential can be evaluated as:

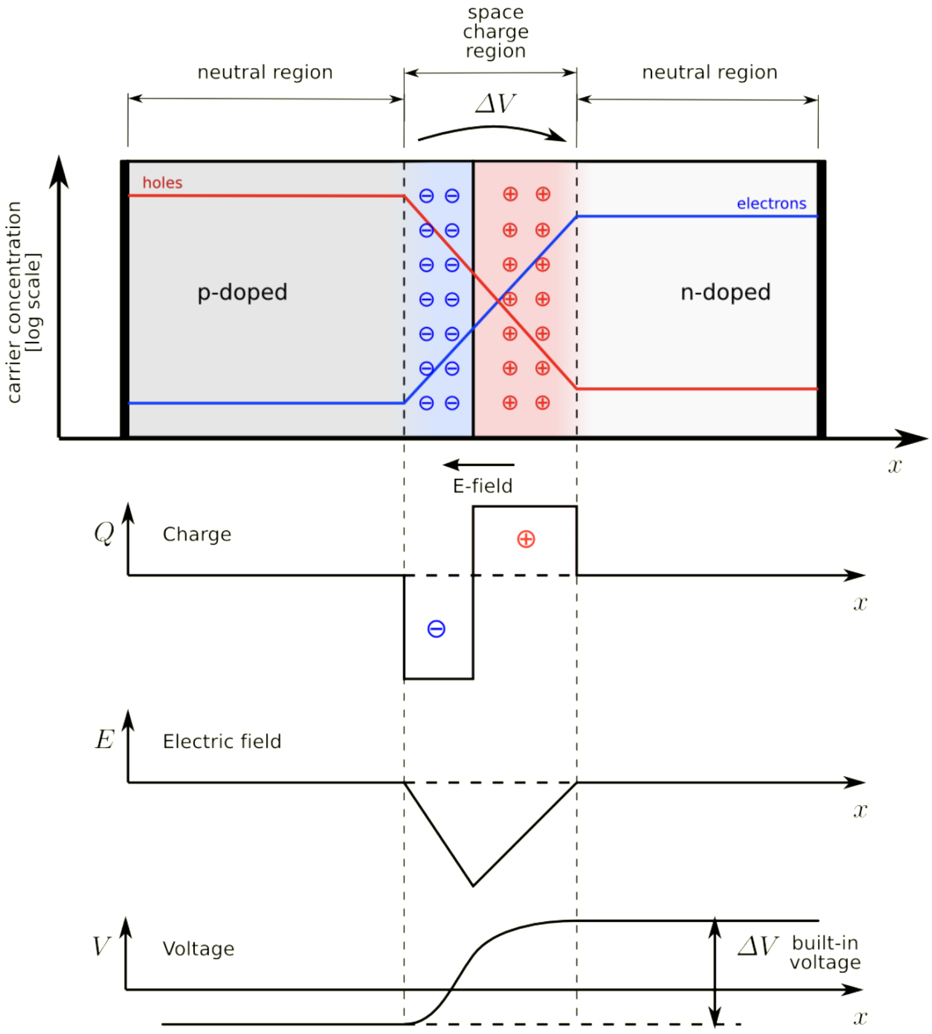

Figure 3.3: A visualization of a p-n junction atomic configuration (top), together with the space charge, electric field and potential along the junction (bottom). Adjusted from [74].

$$V_{bi} = \frac{kT}{e} \ln\left(\frac{N_A \cdot N_D}{n_i^2}\right) \tag{3.4}$$

Where N_A and N_D are the acceptor and donor concentrations, respectively.

The depleted region can be further increased by applying an external reverse bias V_R. In the case of a planar junction, the width W of the depletion region can be written as [67]:

$$\mathrm{W} = \sqrt{\frac{2\epsilon_s}{e}\left(\frac{\mathrm{N}_A + \mathrm{N}_D}{\mathrm{N}_A\mathrm{N}_D}\right)(\mathrm{V}_{bi} + \mathrm{V}_R)} \tag{3.5}$$

Where ϵ_s is the permittivity of silicon.

Because of the fixed charges that are built up on either side of the junction, the depletion region exhibits some properties of a charged capacitor [73]. The junction capacitance can be easily calculated starting from $\mathrm{C} = \epsilon_s \frac{\mathrm{A}}{\mathrm{W}}$ with A the junction area:

$$\mathrm{C} = \mathrm{A}\sqrt{\frac{e\epsilon_s}{2(\mathrm{V}_{bi} + \mathrm{V}_R)}\frac{\mathrm{N}_A\mathrm{N}_D}{\mathrm{N}_A + \mathrm{N}_D}} \tag{3.6}$$

These formulas clearly demonstrate that applying a reverse bias results in a decrease in capacitance.

When a charged particle passes through the p-n junction, it generates electron-hole pairs in the silicon lattice. The number of these pairs is proportional to the energy deposited by the particle.

When an electron in the valence is excited to the conduction band, the process often involves interaction with phonons (lattice vibrations). A consequence of this is that in silicon the avarage energy required to create a e-h pair is not equal to the energy gap, but it is larger [72]. The e-h pair creation energy for silicon is $\mathrm{E}_g = 3.6$ eV [75], meaning that for every 3.6 eV of deposited energy, one electron-hole pair is generated.

3.1.3 Charge carrier migration

Charge carriers propagating through silicon are constantly subject to scattering processes with lattice vibrations, impurities or other imperfections. In the transport equations, the charge carrier mobility is used to account for these microscopic effects. The mobility μ depends on various macroscopic parameters such as the temperature and electric field. It can be parametrised by the Canali model [77]:

$$\mu = \frac{v_m}{E_c\left(1 + \left(\frac{E}{E_c}\right)^{\beta}\right)^{1/\beta}} \tag{3.7}$$

where v_m, E_c and β are phenomenological temperature-dependent parameters.

Once electron-hole pairs are generated in silicon, they begin to move due to two primary mechanisms: drift and diffusion. The movement of charge carriers is described by the current density equation, which consist of a drift term and a diffusion term [72]:

$$J = J_{\text{drift}} + J_{\text{diff}} \tag{3.8}$$

Drift

Drift is the motion of charge carriers in response to an electric field. Charge carriers propagate with an average drift velocity v_{drift} that results from acceleration caused by the electric field E and microscopic scattering events. The velocity is therefore expressed by:

$$v_{\text{drift, e/h}} = \mu_{e/h} E \tag{3.9}$$

where $\mu_{e/h}$ is the electron/hole mobility.

The macroscopic current density is given by:

$$J_{\text{drift},e/h} = n_{e/h} \mu_{e/h} q E \tag{3.10}$$

where $n_{e/h}$ is the electron/hole concetration and q is the charge.

Diffusion

Diffusion is based on random walk of charge carriers in the material. In case of a non-uniform distribution of charge carriers, a diffusion along the charge carrier gradient takes place. Diffusion can be parametrised by introducing a diffusion constant $D_{e/h}$ for electrons/holes, that is related to the charge carrier mobility according to the Einstein relation:

$$D_{e/h} = \frac{kT}{q} \mu_{e/h} \tag{3.11}$$

where k is the Boltzmann constant and T is the temperature.

The diffusion current density is then given by the concentration gradient Δn and the diffusion constant:

$$J_{\text{diff},e/h} = -q D_{e/h} \Delta n \tag{3.12}$$

Charge carrier recombination

Semiconductors are constantly subject to generation-recombination mechanisms that take place to keep a state of equilibrium. However, the generation of electron-hole pairs by ionising radiation causes a disturbance in the system. To return to equilibrium, a net recombination occurs, which depends critically on semiconductor properties such as temperature or doping concentration.

The carrier lifetime τ is the average time that an electron or hole exists before recombining. It is a key parameter that determines the efficiency with which charge carriers are collected in a sensor. A longer carrier lifetime increases the probability that charge carriers will reach the electrodes before recombining.

The main contributor to this recombination is the Shockley-Read-Hall (SRH) recombination [78]. It appears if an electron transitions from the conduction band to the valence band bypassing an intermediate energy state in the bandgap. This energy state is created by a dopant or a defect in the lattice and is typically called a trap.

The carrier lifetime can be reduced by the presence of impurities that act as recombination centers, and since the most common source of impurities is doping, τ and N_D are strictly related as described by the empirical Scharfetter relation:

$$\tau(\mathrm{N}_A + \mathrm{N}_D) = \tau_{min} + \frac{\tau_{max} - \tau_{min}}{1 + \left(\frac{\mathrm{N}_A + \mathrm{N}_D}{\mathrm{N}_{ref}}\right)^{\gamma}} \tag{3.13}$$

The lifetime also depends on the temperature, increasing with rising temperature and decreasing with lower temperature. It can be modelled as it follows:

$$\tau(T) = \tau_0 \cdot exp\left[C\left(\frac{T}{300K} - 1\right)\right] \tag{3.14}$$

The standard parameters from the Sentaurus TCAD SDEVICE manual are displayed in Table 3.1.

Carrier type	τ_{min} [s]	τ_{max} [s]	N_{ref}[cm^{-3}]	γ	C
Electrons	0	1×10^{-5}	1×10^{16}	1	2.55
Holes	0	3×10^{-6}	1×10^{16}	1	2.55

Table 3.1: Default parameters for doping- and temperature-dependent SRH lifetime.

Recombination only plays a role at doping levels higher than $1 \times 10^{18}\mathrm{cm}^{-3}$, reached only in the collection electrode, the p-wells and the substrate. As the substrate is the only of these regions where carriers move around freely, this is the only region of interest for carrier lifetime considerations.

3.2 Radiation damage

Silicon sensors in a particle physics experiment are by definition exposed to a level of radiation depending on the interaction rate, the distance of the sensor to the interaction point, and the material between interaction point and sensor. The radiation consists in general of charged and neutral particles, as well as of gamma and X-rays, which can generate radiation damages in the sensor impacting its performance. Radiation damage on silicon detectors can occur following two main mechanisms [33]: non-ionising and ionising damage.

3.2.1 Non-ionising radiation damage

Non-ionising radiation damage is linked to Non-Ionising Energy Loss (NIEL) which depends on the particle type and energy. NIEL is expressed as equivalent fluence Φ of 1 MeV neutrons per square centimetre (1 MeV n_{eq} cm^{-2}). In this case, incident radiation displaces silicon atoms from their lattice sites. The resulting defects alter the electrical characteristics of the crystal. Figure 3.4 shows a sketch of the energy level structure of different possible lattice defects.

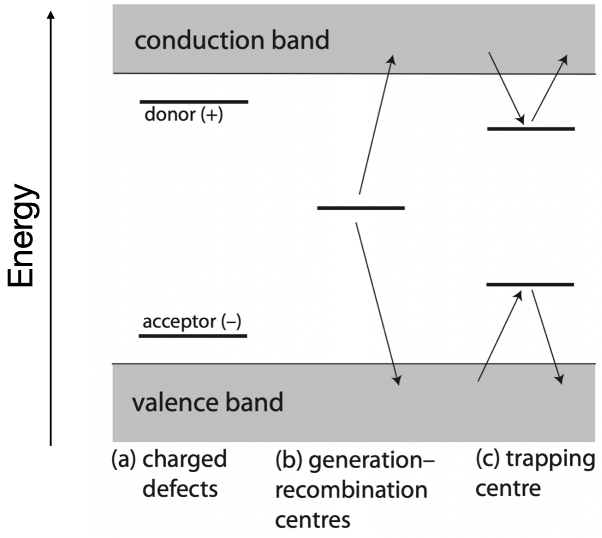

Figure 3.4: Sketch of typical additional energy level locations due to lattice defects. Adjusted from [79].

The consequences of displacement damage manifest in three important ways:

(a) Generation of donor or acceptor centers that causes a change in doping characteristics. Four processes are responsible for effective doping changes [80]: the removal of donors due to the formation of defect complexes containing donors, the removal of acceptors due to the formation of defect complexes containing acceptors, the creation of defect complexes assuming positive charge states in the space-charge region and the creation of defect complexes assuming negative charge states in the space-charge region. The following fluence dependence of the effective doping concentration is expected from an independent occurrence of these processes:

$$N_{eff} = N_{a0}e^{-c_a\Phi} - N_{d0}e^{-c_d\Phi} + b_a\Phi - b_d\Phi \tag{3.15}$$

where N_{a0} and N_{d0} are donor and acceptor concentrations before irradiation and c_a, c_d, b_a and b_d empirical constants. The effective doping concentration in a p-type silicon as a function of neutron fluence is shown in Figure 3.5.

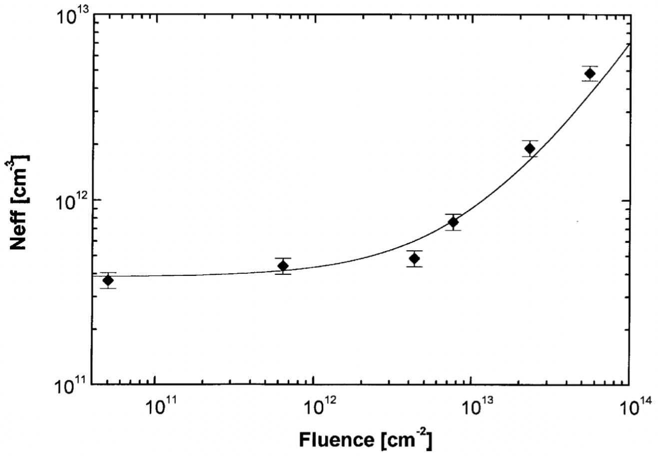

Figure 3.5: Effective doping concentration in a p-type silicon as a function of neutron fluence. Taken from [81].

(b) Formation of mid-gap states, which facilitate the simultaneous transition of electrons to the conduction band and of holes to the valence band. In depletion regions this leads to a generation current called 'leakage', i.e. an increase in the current of reverse-biased p-n junctions. In forward biased junctions or non-depleted regions mid-gap states facilitate recombination, i.e. charge loss. Leakage current increase is proportional to the fluence Φ and is described by the following equation [33]:

$$\mathrm{I}_d = \mathrm{I}_0 + \alpha \mathrm{V}\Phi \tag{3.16}$$

where I_0 is the current before irradiation, α is a current damage factor and V is the volume of the depleted region of the junction.

(c) Generation of traps, which capture charge and release it after some time. This significantly affects the carrier lifetime, which decreases with the presence of impurities, thus at higher fluences. The correlation between lifetime and fluence is given by [82]:

$$\frac{1}{\tau} = \frac{1}{\tau_0} + \frac{\Phi}{K} \tag{3.17}$$

where τ_0 is the lifetime before irradiation and K is the silicon damage constant ($K \approx 2 \cdot 10^6$ s/cm^2 [83]).

During the operation time of ITS3 non-ionising radiation damage is expected, and the total radiation hardness requirement for NIEL is of 10^{13} 1 MeV n$_{eq}$ cm^{-2} [41]. This level is expected to result in no significant performance degradation, as supported by the findings presented in Chapter 4.

3.2.2 Ionising radiation damage

Ionising radiation damage is relevant especially in the integrated circuitry, in particular in MOS transistors. It essentially affects the surface oxide layers, the critical material is silicon dioxide (SiO2). In the oxide, charged particles and sufficiently energetic photons produce electron-hole pairs. Electrons and holes in SiO2 have very different mobility; hence if an electric field is applied, the two are quickly separated. In absence of electrons, the holes can not recombine and are trapped in the oxide, where they can originate two types of defects. In the oxide itself, the trapped holes generate positive charges. At the interface between the oxide and the crystalline silicon they can generate the so-called interface states, which can behave as donors or acceptors. This can give rise to leakage currents between drain and source of NMOS transistors and in between neighbouring transistors. A reduction of these effects has been observed when moving to smaller technology nodes [84–86].

This type of irradiation is linked to the Total Ionising Dose (TID) and is expressed in Gy. The ITS3 radiation hardness requirement for TID is of 10 kGy [41], a level at which a small but not dramatic effect is expected.

3.3 Energy loss of particles in silicon detectors

The two main types of charge deposit relevant for this work are energy loss of charged particles and absorption of photons in silicon. A brief overview of these will be provided in this section.

3.3.1 Charged particles

Charged particles, such as protons and heavy ions, lose energy as they pass through silicon primarily through ionization and excitation of the silicon atoms [73, 87–89].

When a charged particle travels through silicon, it interacts with the electrons in the material. These interactions can excite the electrons to higher energy levels or ionize the silicon atoms by completely removing an electron from the atom.

The equation used to determine the mean rate of energy loss of relativistic charged particles other than electrons is called the Bethe-Bloch equation:

$$-\frac{dE}{dx} = \frac{4\pi N_A r_e^2 m_e c^2 z^2 Z}{A\beta^2}\left[\frac{1}{2}\ln\left(\frac{2m_e c^2\beta^2\gamma^2 T_{\mathrm{max}}}{I^2}\right) - \beta^2 - \frac{\delta}{2}\right] \tag{3.18}$$

where: N_A is Avogadro's number, r_e is the classical electron radius, m_e is the electron mass, c is the speed of light, z is the charge of the incident particle, Z is the atomic number of the material, A is its atomic mass, β and γ are the velocity and Lorentz factor of the particle, T_{max} is the maximum kinetic energy transferable to an electron in a single collision, I is the average excitation and ionisation potential of the absorber (normally treated as an experimentally determined parameter for each element [73]) and δ is the density correction, relevant at high energies. The density effect takes into

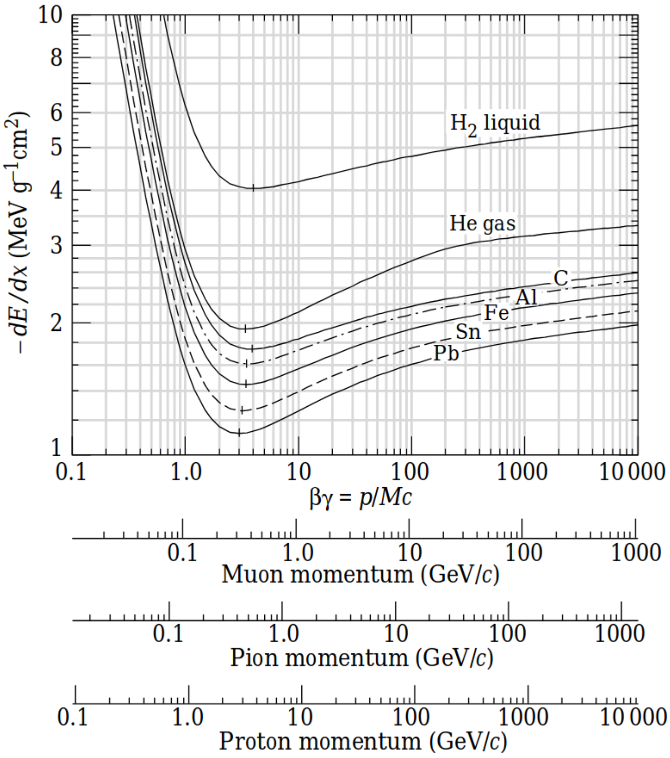

Figure 3.6: Stopping power curve for different materials versus momentum of various particles. Taken from [90].

account that as the particle energy increases, its electric field flattens and extends, so that the distant-collision contribution increases. However, real media become polarised, limiting the field extension. Collisions with these outer lying electrons will therefore contribute less to the total energy loss [90].

Since electrons moving through a medium are indistinguishable from electrons in the outer shells of atoms in the medium and because the energy loss of electrons is mainly through bremsstrahlung, they are described by the Berger-Seltzer equation.

Figure 3.6 shows the stopping power curve for different materials versus momentus of various particles.

The energy loss, at non-relativistic energies, is dominated by the $1/\beta^2$ factor and decreases with increasing velocity until a minimum is reached (Minimum Ionising Particle (MIP)).

For energies below MIP each particle exhibits a curve which, in most cases, is distinct from the other particles. This characteristic is often exploited in particle physics to identify particles in this energy range. As the energy increases, $1/\beta^2$ becomes almost constant and dE/dx rises again due to the logarithmic (γ) dependence.

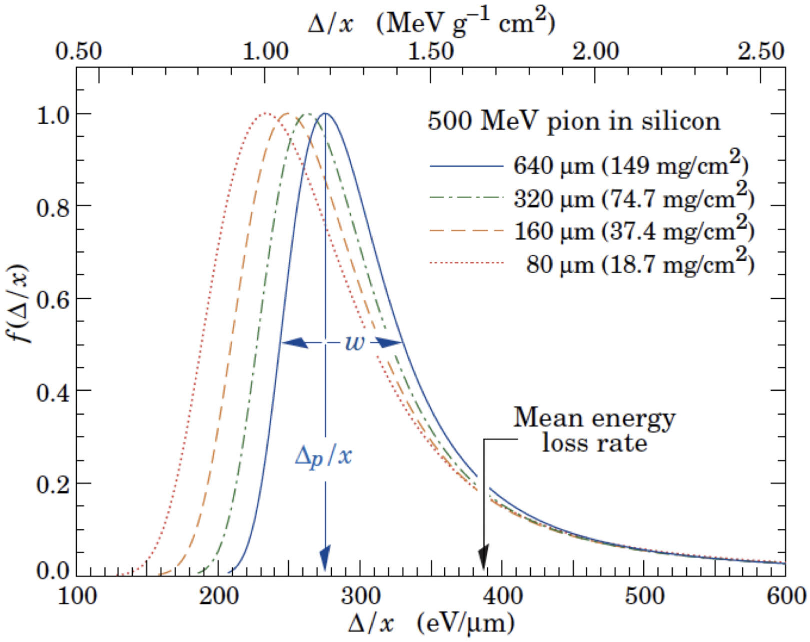

Figure 3.7: Energy loss distribution in silicon for 500 MeV pions, normalised to unity at the most probable value Δ_p/x, for different sensor thicknesses. Taken from [91].

The fluctuations of energy loss depend strongly on the medium's thickness. For thin sensors (around 200 - 300 µm), the Landau distribution [92] describes the fluctuations of energy loss quite well.

The Landau model fails to describe the energy loss distribution in very thin ($d < 160$ µm) silicon absorbers; the most probable value (MPV) is underestimated while the distribution FWHM is overestimated [93]. A much better description is given by Bichsel functions [94]: Bichsel calculations indicate that for increasing absorber thicknesses the MPV increases and the ratio FWHM/MPV decreases. This effect is shown in Figure 3.7, representing the energy loss distribution for 500 MeV pions incident on thin silicon detectors of different thickness.

An even more accurate way of treating the energy deposition is the PAI model [95].

3.3.2 Electromagnetic radiation

Photons interacts with silicon primarily through four mechanisms [87]: the photoelectric effect, coeherent or incoherent scattering, and pair production. The cross sections for these four interaction processes are reported in Figure 3.8.

A beam of photons of initial intensity I_0 passing through a thickness of material x, is attenuated in intensity as it follows:

$$I(x) = I_0 e^{-\mu x} \tag{3.19}$$

where μ is the absorption coefficient, characteristic of the absorbing material.

Photoelectric effect In the photoelectric effect, a photon is absorbed by an atom, resulting in the ejection of an electron. The energy of the ejected electron is equal to the energy of the incident photon minus the binding energy of the electron in the atom. The probability of the photoelectric effect occurring is higher for photons with energies just above the binding energy of the electron and decreases rapidly for higher energy photons.

In silicon, the photoelectric effect is most significant for photons with energy lower than 50 keV. In the context of this thesis, this region is the most relevant one, as it includes the energies of the X-rays frequently used for MAPS characterization (see next paragraph on ^{55}Fe source).

Compton scattering Compton scattering occurs when a photon interacts with a free or loosely bound electron in the material, transferring part of its energy to the electron

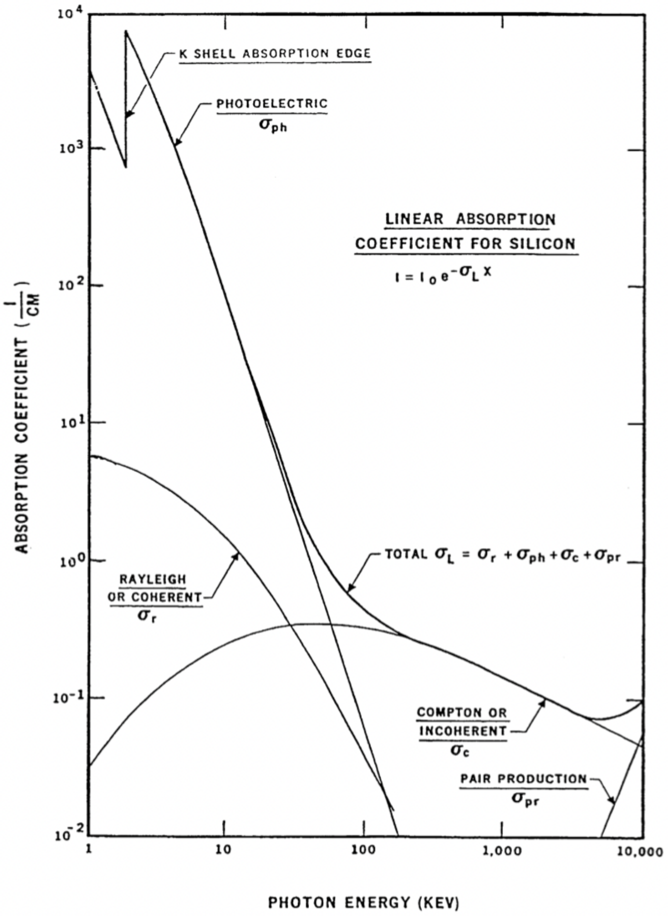

Figure 3.8: Energy dependent cross section of the three dominant energy loss mechanisms for photons in silicon. Taken from [96].

and scattering the photon in a different direction with reduced energy. The energy transferred to the electron is related to the angle at which the photon is scattered.

Compton scattering is the dominant interaction mechanism for medium-energy (between 50 keV and 10 MeV) photons in silicon detectors.

Pair production Pair production is a process in which a high-energy photon (above 1.022 MeV, which is twice the mass of the electron) interacts with the strong electric field near the nucleus of an atom, resulting in the creation of an electron-positron pair. Photon energy greater than this amount is converted into motion of the electron-positron pair.

In silicon detectors, pair production is significant for high-energy (higher than 10 MeV) photons.

^{55}Fe X-ray source

In the characterization of MAPS, a ^{55}Fe source is frequently employed due to its ability to perform precise energy calibrations.

The ^{55}Fe isotope decays via electron capture to ^{55}Mn with a half-life of 2.747 years, resulting in the emission of Auger electrons, X-rays, and γ-photons. The ^{55}Fe emissions, along with their energies and number of emitted particles per 100 disintegrations of the parent nuclide are reported in Table 3.2.

	Energy (keV)	**Emissions per 100 disint.**
Auger electrons	0.47 - 0.67	140.2
	4.95 - 6.53	60.1
X-rays	0.56 - 0.72	0.524
	5.888 (K_α)	8.45
	5.899 (K_α)	16.57
	6.490 (K_β)	3.40
	6.535 (K_β)	
γ	125.959	1.3×10^{-7}

Table 3.2: Emissions of ^{55}Fe [97].

Only the X-ray emissions are relevant for this work. The main ones have energies of 5.9 keV and 6.5 keV, corresponding to K_α and K_β transitions in manganese Mn.

The mean free paths for the energies 0.639 keV, 5.895 keV and 6.490 keV in air correspond to 2 mm, 323 mm and 435 mm [98]. At a distance of, for example, 2 cm the photons below 1 keV will be absorbed, while the photons with energies around 6 keV make it to the sensor. In silicon the mean free path for the Mn-K_α and the Mn-K_β lines are 27 µm and 36 µm respectively [98].

The intrinsic energy resolution can be estimated as $R = 2.35\sqrt{\frac{F \cdot w}{E}}$ where F is the Fano factor in silicon (F $\approx$ 0.118 for 5.895 keV [99, 100]), w is the energy required to excite an electron-hole pair (3.6 eV) and E is the photon energy. This result in an energy resolution of approximately 2% or about 118 eV. Therefore, while the difference between Mn-K_α and Mn-K_β can still be resolved, the resolution is not enough to resolve the sub-peaks 5.888 - 5.899 keV and 6.490 - 6.535 keV. For this reason it is expected to observe only two peaks in the ^{55}Fe spectrum, from the photoelectric absorption of 5.9

and 6.5 keV photons in silicon.

The electrons produced by the absorption of 5.9 and 6.5 keV X-rays in silicon generate electron-hole pairs along their paths. Since the average energy required to produce an electron-hole pair in silicon is about 3.6 eV, the absorption of these X-rays typically results in the creation of approximately 1640 and 1800 electron-hole pairs, respectively.

When an X-ray photon strikes a silicon atom, it ejects an electron from one of its shells, creating a vacancy. This vacancy is filled by an electron from an outer shell. By going to a state of lower energy there is the chance that the outer electron's excess energy will be released as a photon with an energy corresponing to the difference between the shell energies. These are called characteristic X-rays and are specific to the absorber material [101]. The other and the far more likely option is that the excess energy will ionise the atom by releasing an electron from the outer shells as an Auger electron. For silicon, focus is primarily on vacancies in the K-shell, which can be filled by electrons from the L or M shells, producing Si-K_α and Si-K_β photons with energies of 1.74 keV and 1.84 keV, respectively. The L-shell filling is much more likely than the M-shell [102]. However, since Auger electron emission is more probable (over 95%) and since these two peaks usually overlap, high-statistics measurements are needed to observe the Si-K_α and Si-K_β lines in the spectrum. If these X-rays escape the detector, also an escape peak appear at the difference between the incoming photon energy and the Si-K_α or Si-K_β energy.

3.4 Working principles of Monolithic Active Pixel Sensors

Silicon pixel detectors and also the associated integrated readout electronics rapidly became standard building blocks for detector systems and broke the way to the precise measurement of short-lived particle decay vertices. They find important applications in particle physics experiments, most notably in the detectors which are currently being built for the LHC [67].

The most common implementation of this technology is the 'hybrid' pixel detector, which is widely used in the tracking systems of many LHC experiments. While highly effective, hybrid sensors have some limitations, primarily due to the separation of the sensor and readout electronics into distinct components. This separation requires complex interconnection techniques, such as bump-bonding, which adds to the material budget and limits the potential for finer granularity. Additionally, the bump-bonding process can be costly and impact the overall yield of sensor production, further complicating the manufacturing process. A schematic of its cross section is shown in Figure 3.9(a).

Monolithic Active Pixel Sensors (MAPS), a direct evolution of Charge-Coupled Devices (CCDs) [104], intergate both the sensor and a CMOS-based readout electronics onto a single silicon substrate. This monolithic approach (shown in Figure 3.9(b)) overcomes some of the limitations of traditional hybrid detectors by eliminating the need for separate sensor and readout components, thus reducing material thickness.

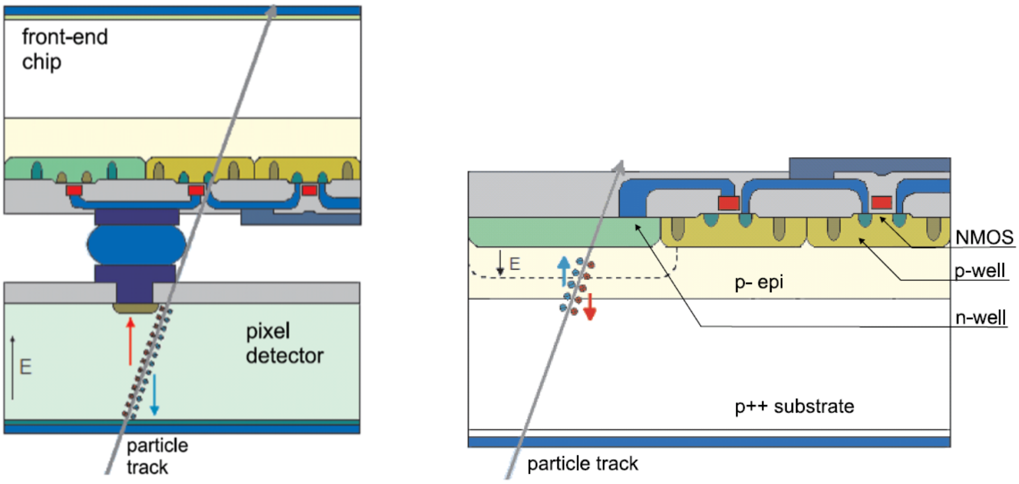

(a) Hybrid pixel.

(b) MAPS pixel.

Figure 3.9: Cross section scheme of a hybrid and a MAPS pixel. The hybrid pixel (a) consist of Si sensor bump-bonded to CMOS read-out electronics while MAPS (b) combines the two in a single volume. Taken from [103].

The cross section of a typical Monolithic Active Pixel Sensor designed for high-energy physics experiments is shown in Figure 3.10.

It consists of three layers: a highly p-doped p^{++} (typical doping concentration around 10^{18} cm^{-3}) substrate at the back of the chip, a thin (few tens of µm) p^{-} (typical doping concentration around 10^{14} cm^{-3}) epitaxial layer built on top of the substrate that serves as the sensitive volume, and n-type and p-type implants on top of the epitaxial layer, known as wells. The epitaxial layer has lower doping concentration compared to the substrate, which results in higher mobility and longer carrier lifetime. The central n-type implant function as collecting electrode for the electrons coming from the electron-hole pairs produced by the particle crossing, while the deep p-wells host the associated circuitry.

In the first implementations of monolithic technology, only NMOS electronics was possible (see Figure 3.9(b)). As mentioned in Section 1.3.1, more recent implementations

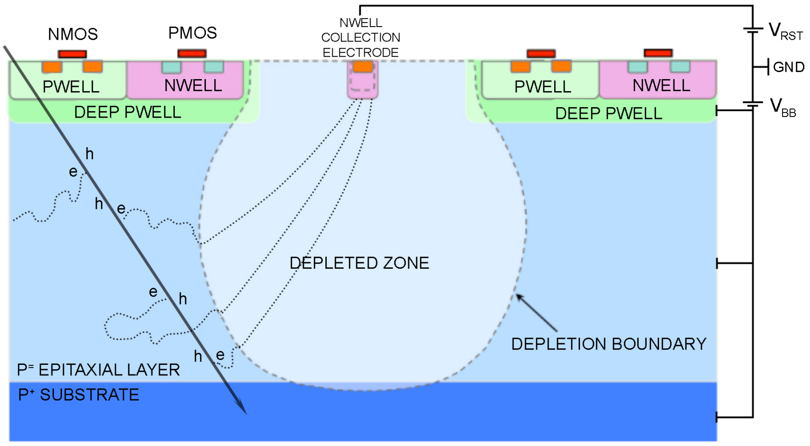

Figure 3.10: Schematic view of the well-structure used for ALPIDE and the corresponding charge collection.

like ALPIDE, include an innovative process feature that allows both NMOS and PMOS. To prevent the n-wells hosting the PMOS transistors from inadvertently collecting electrons and thus competing with the collection diode, these components are isolated from the epitaxial layer by incorporating a deep p-well beneath the n-well.

When a charged particle traverses the silicon detector, it loses energy through ionization, generating electron-hole pairs along its path. Electrons produced within the epitaxial layer are generally confined within it due to reflective barriers formed by the p^-p^{++} and p^-p-well junctions. These electrons diffuse within the epitaxial layer until they reach a depleted region where they are collected mainly by drift. Electrons originating in the p-wells or substrate that thermally diffuse into the epitaxial layer are also collected.

The application of a small voltage enlarges the depleted region, although the majority of the epitaxial layer remains undepleted. The depletion region can be further expanded by applying a negative reverse bias voltage to the substrate, as indicated by the V_{BB} in the schematic in Figure 3.10.

As shown in Figure 3.11 metal layers are built above the implants, forming the in-pixel circuitry and propagating the signal and bias from the chip periphery.

Moving forward, new implementations were developed featuring different variants of the implant geometry. This progressive development, described in detail in Section 4.1, is based on an additional low-dose deep n-type implant (see Figure 4.2) which results in a much faster charge collection and significantly improved radiation hardness. Furthermore, thanks to the advances in the density of CMOS digital electronics that enable to

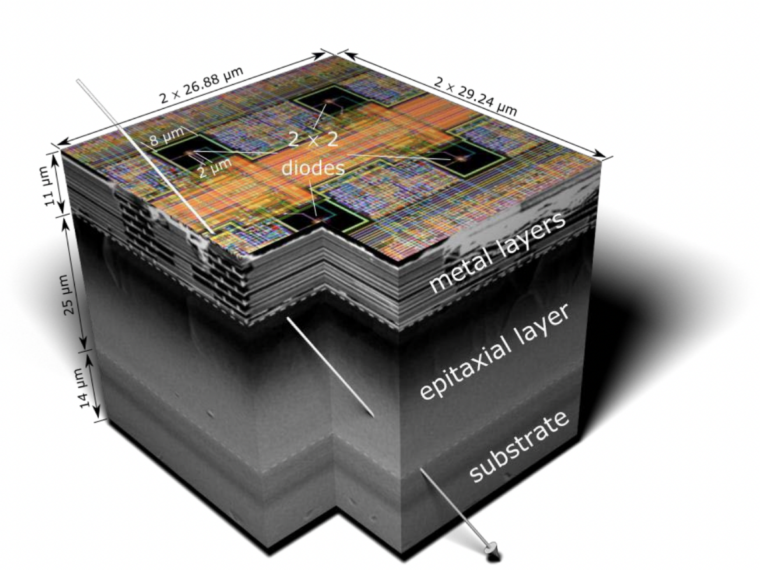

Figure 3.11: MAPS 3D schematic rappresentation - A matrix of 2 × 2 pixels belonging to the ALPIDE chip. Taken from [105].

pack more and more electronics into each pixel, these new developments will transition from a 180 nm to a 65 nm technology node. This will also allow a reduction in pixel pitch for improved timing and spatial resolution as well as a smaller collection electrode, which will results in a lower sensor capacitance and consequently a higher signal to noise ratio.

These modern MAPS are capable of delivering exceptional spatial resolution (below 5 μm), even in high-occupancy environments, due to their small pixel size (few tens of μm of pixel pitch).

In summary, MAPS technology emerged as an attractive option for future tracking systems as it offers low cost high precision tracking sensors with simplified interconnections compared to hybrid pixel detectors. Additionally, MAPS provide superior spatial resolution and low material budget. Their monolithic design allows for compact, lightweight detectors which reduces scattering of particles and improves tracking precision. Finally, their low power consumption (consequence of the small capacitance) and ability to cover large areas also make them highly efficient for large-scale tracking systems.

Chapter 4

The Analogue Pixel Test Structure

As already mentioned in Section 2.1 validating the TPSCo CMOS 65 nm ISC process is a crucial step for the advancement of the ITS3 R&D. Several prototype structures have been produced to characterise and qualify this process and to optimise the sensor for the next generation of Monolithic Active Pixels Sensors for high-energy physics.

In this chapter a detailed desctiption of the analogue prototype (APTS) is given, together with an overview of the characterisation conducted using data collected from both laboratory measurements and charged particle beam tests. Initially, it provides an introduction to the sensor and its various available variants. Subsequently, the discussion focuses on the description of the set-up used for the measurements, the analysis methodology employed, and the findings from this chip characterisation.

A substantial portion of the work presented in this thesis is included in a published paper [106]. However, this thesis offers a more comprehensive study, including additional material and measurements.

4.1 The APTS chip

The APTS serves as the perfect testing ground for the 65 nm technology because it can provide a comprehensive understanding of the charge collection performance of the chip.

It has an area of 1.5 mm × 1.5 mm and contains a matrix of 6 × 6 square pixels, of which only the 4 × 4 central ones are read out, with very fast (rise and fall times of a few 100 ps) analog outputs directly buffered to output pads for off-chip real-time observation of all pixels in parallel [107]. A more detailed description of the front-end chain is presented in Section 4.1.1.

Several variants of the APTS chip were produced, variating: the implant geometry design, to study different carge collection processes; the so-called 'split', which correspond to gradually modifying the doping levels [108]; the pixel pitch, going from 10 to 25 µm; and finally the geometry of p-well and n-well electrodes. Additionally, all the chip variants that were tested were also irradiated at different levels of radiation, both for NIEL and TID.

The design of APTS offers the possibility to supply a negative bias both to the substrate, V_{sub}, and to the deep pwells, V_{pwell}, hosting the circuitry (see Figure 4.4). For the measurements presented in this thesis, they were always kept at the same potential ($V_{\text{sub}} = V_{\text{pwell}}$). Increasing this reverse bias results in a reduction of the sensor capacitance due to the increased depletion around the collection electrode, as explained in Section 3.1.2.

In Figure 4.1 and Table 4.1 a photo of the chip under the microscope and its main characteristics and different variants are reported.

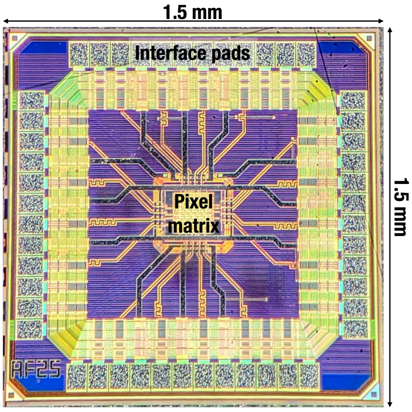

Figure 4.1: The APTS chip.

	APTS
die size	1.5 mm × 1.5 mm
matrix	6×6 pixels
readout	direct analogue of central 4×4 pixels
pitch	10, 15, 20 or 25 µm
design	standard, mod., mod. with gap
split	1, 2, 3, 4
variant	ref., larger n-well, smaller p-well, finger p-well

Table 4.1: Main characteristics and variants of the APTS silicon sensors.

Similar to what was implemented in ALPIDE [109] in a 180 nm process, the pixel sensor design consists of a small nwell collection electrode and a high-resistivity p-type epitaxial layer grown on p-type substrate, with the in-pixel circuitry located in deep p-wells. There are three different implant geometries (shown in Figure 4.2) implemented as APTS variants and used to test different charge collection processes:

- The **standard** process, where the high-resistivity epitaxial layer is typically not fully depleted 4.2(a). The depletion region is balloon-shaped extending from the junction at the collection electrode without reaching the pixel edges. The charge generated outside the depletion region is collected primarily by diffusion, for this reason the collection can be relatively slow.
- The **modified** (or modified with blanket) process, with a deep low-dose n-type implant under the full pixel area. With the application of a reverse substrate bias,

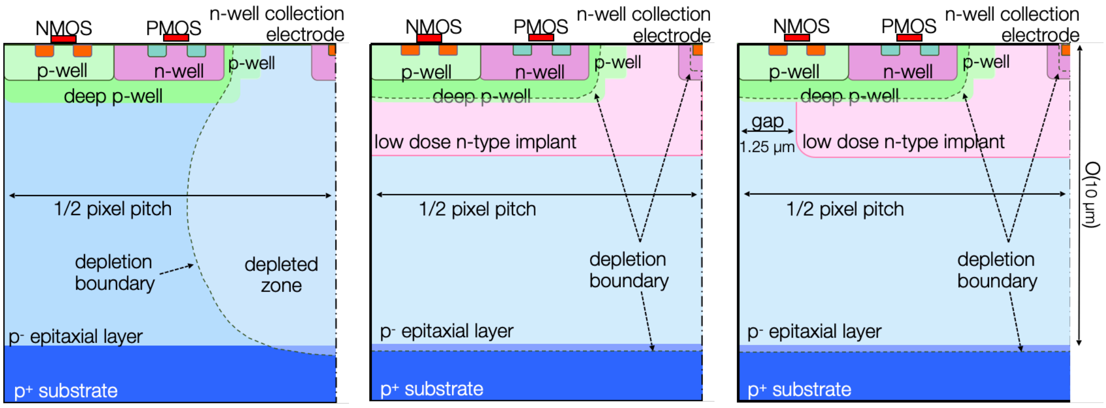

(a) Standard process.
(b) Modified process.
(c) Modified with gap process.

Figure 4.2: Half cross-sections of the three different pixel designs implemented: (a) standard: no additional low-dose implant, (b) modified: with deep blanket low dose n-type implant, and (c) modified with gap: with a gap in the deep low dose n-type implant at the pixel borders. Taken from [106].

this allows full depletion of the epitaxial layer and a faster charge collection by drift 4.2(b).

- The **modified with gap** process, where the same low dose n-type implant features a gap of 2.5 µm (1.25 µm per side) at the pixel boundaries 4.2(c). This prevents low-field regions between pixels and creates a vertical junction to increase the lateral electric field pushing the charge from the pixel boundary towards the collection electrode, thus reducing the charge sharing among neighbouring pixels.

Moving from process 4.2(a) to 4.2(c) the charge sharing among pixels is expected to decrease, with more and more charge collected by a single pixel and, as a consequence, with a potential increase of the operating margin.

The APTS was also produced in four process splits (named 1, 2, 3, 4), that gradually modify the doping levels of the implants, with the purpose of improving the isolation between the sensor and the circuitry and preventing local potential wells retaining the signal charge [110].

In addition, to explore the influence on capacitance and charge collection, the geometry and size of both n-well collection electrode and the p-well were implemented in four different variants (in Figure 4.3 two of them are depicted):

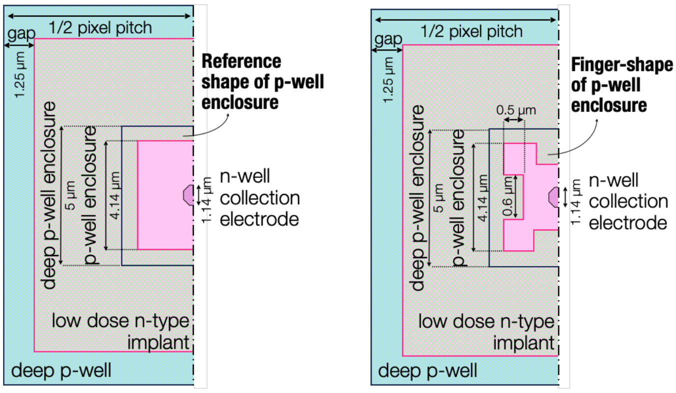

(a) Reference. (b) Finger-shaped enclosure.

Figure 4.3: Top view of half a pixel of a modified with gap pixel design for different shapes of the deep p-well: (a) reference shape and (b) finger-shaped p-well enclosure. Taken from [106].

- **Reference**: n-well collection electrode size of 1.14 µm and a square p-well enclosure of 4.14 µm, see Figure 4.3(a) for the top view.
- **Smaller p-well enclosure**: p-well enclosure of 3.14 µm.
- **Larger n-well collection electrode**: n-well collection electrode of 2.28 µm.
- **Finger-shaped p-well enclosure**: the shape of the p-well enclosure is changed as sketched in Figure 4.3(b) resulting in p-well fingers further approaching the collection electrode.

4.1.1 In pixel front-end

A schematic of the front-end chain of the APTS is shown in Figure 4.4. The circuit is responsible for buffering the electrode signal to an output pad. The buffer chain is partially implemented in the pixel and partially in the matrix periphery.

The diode D0 represents the sensor and the biasing and reset of the collection electrode are performed by the PMOS transistor M0. The DC voltage on the collection electrode is close to the voltage set on the source of M0, i.e. V_{reset}. The I_{reset} current instead defines the reset rate of the collection electrode after a hit.

The collection electrode is DC connected to the in-pixel circuit. The latter is composed by two source-follower stages, respectively a p-type (M1 and M2) and n-type follower

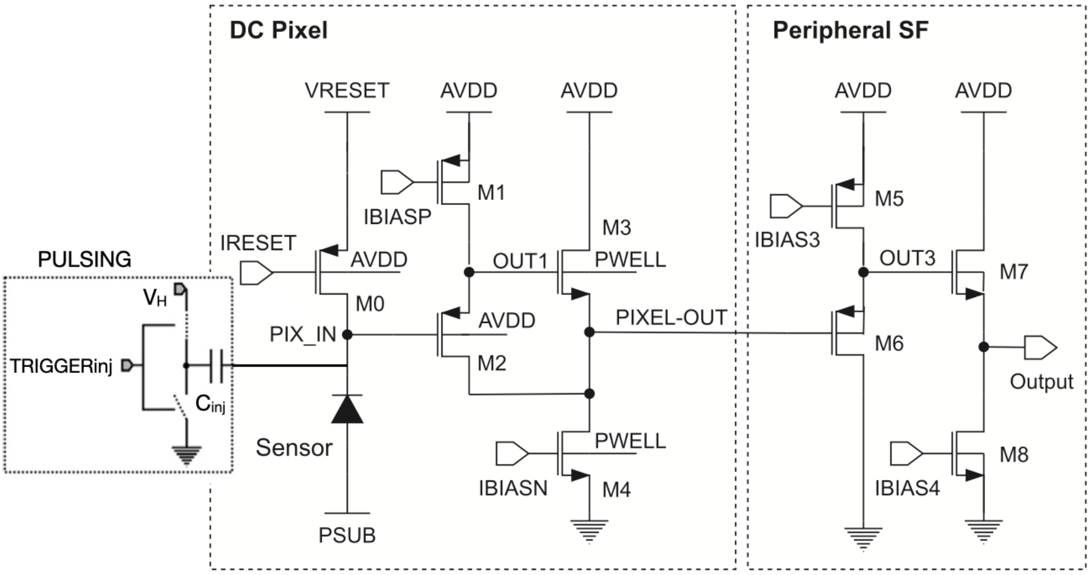

Figure 4.4: A schematic of the front-end chain of APTS. Taken from [107].

(M3 and M4), with the output of the second one connected to the drain of the input transistor in the first stage. Because of this connection, both the source and the drain of the input transistor of the readout chain follow the voltage on the collection electrode which reduces the capacitive load on the collection electrode. The two source-follower stages in the peripheral circuit buffer the output signal of each individual pixel in the matrix and send it via an analogue output pad to an off-chip ADC.

Additionally, there is an analogue pulsing circuit inside the pixel which allows the injection of a test charge through an injection capacitor $C_{\text{inj}} = 242$ aF (nominal value) into the collection electrode, when the $\text{TRIGGER}_{\text{ing}}$ is given. The injected charge can be tuned through the voltage setting V_{H}, which can go up to 1.2 V. In the leftmost part of Figure 4.4 a block diagram of the pulsing circuit is reported.

4.1.2 Test system

The chip is operated and read out by a custom test system, which was specifically developed for the MLR1 submission within the ITS3 R&D [111]. This test system is shown in Figure 4.5 and consists of three parts: a DAQ (Data Acquisistion System) board (designed based on the one developed for the ALPIDE) that provides power and 28 digital I/Os of adjustable logic voltage; a proximity card that hosts additional components that could not be retrofitted to the original ALPIDE DAQ board design; and a carrier card that hosts the chip. Edge connectors carry power and digital or analog signals.

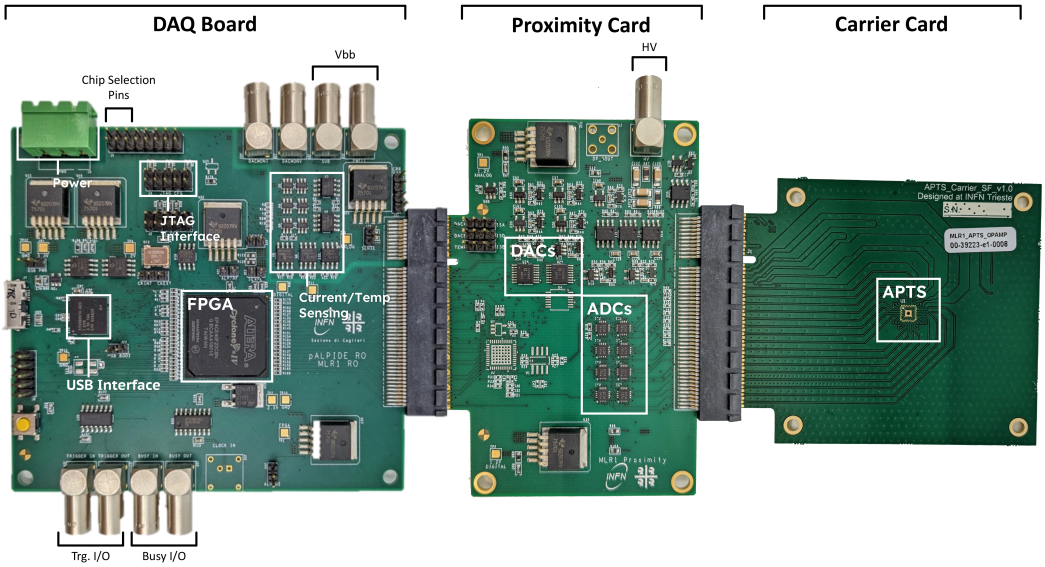

Figure 4.5: DAQ system: FPGA-based DAQ board + chip-specific proximity + chip carrier card. Taken from [111].

At the heart of the DAQ Board, an FPGA (Field Programmable Gate Array) operates the LDOs (Low Dropout Regulators), ADCs (Analogue to Digital Converters), and DACs (Digital to Analogue Converters) located on board as well as on the proximity card. Communication with a PC via the USB 3.0 interface is mediated by a USB FX3 peripheral controller, which is connected to the FPGA through a FIFO (First In First Out) interface. LEMO connectors can be used to apply back-bias voltage and operate the system on external trigger mode. Three dual-channel 10-bit ADCs monitor the currents provided to the sensor and its temperature.

The proximity card hosts the circuitry for voltage/current biasing as well as ADC conversion, as the DAQ board only supports digital readout chips. Two on-board 8-channel 16-bit DACs provide voltage and current biases to the chip directly. Readout capabilities are provided by eight dual-channel 16-bit ADCs for parallel readout of all the 16 analogue pixels up to 4 MSPS.

The readout is controlled by the FPGA and the sampling period can be adjusted with a granularity of 6.25 ns up to a maximum sampling frequency of 4 MHz. A rolling buffer can store up to 100 samples so that each event carries information on what happened before its triggering.

As mentioned in the previous section, the chip can also be pulsed, meaning the FPGA can trigger a charge injection in one or more pixels for all sorts of functional tests.

Three readout modes are implemented:

- The pulsing mode, which sends a trigger via software while simultaneously injecting charge via the in-pixel pulsing circuit. This mode is useful for the characterisation of the chip in the lab, such as the effect of different biases.
- The external trigger mode, here an event is acquired when a logic pulse is detected at the appropriate LEMO input (TRIGGER_IN port).
- The internal trigger mode, here the system acquires an event when the signal exceeds a threshold set by the user. Each pixel can be individually enabled or disabled as internal trigger source.

4.2 Signal extraction and noise

An initial investigation into the pixel response was conducted using the built-in pulsing circuit (see Figure 4.4). Thus injecting a charge into the pixels by applying V_{H} (up to 1200 mV) to an injection capacitance.

Figure 4.6 shows signal waveforms obtained at a back-bias voltage of 1.2 V ($V_{\mathrm{sub}} = V_{\mathrm{pwell}} = 1.2$ V) and pulsing the matrix with $V_{\mathrm{H}} = 1200$ mV. This value, approximately equivalent to 1800 electrons, is expected to be close to the value obtained from the ^{55}Fe source (refer to section 4.4). Each waveform is sampled at the maximum rate, with a sample period of 250 ns.

The waveforms have different baselines, but similar amplitudes and shapes for all the pixels. The signal is estimated as the difference between the baseline and the minimum of the waveform, and it increases linearly when increasing V_{H}. The baseline value is determined using the output of the 4^{th} sample before the minimum. This selection is made due to a significant short-time auto-correlation observed among nearby samples, detailed in Appendix A.

The study of the baseline fluctuations provides information about the noise, which can vary with the back-bias voltage and chip type.

To be consistent with the baseline definition, also the RMS noise was defined using a specific frame. In particular, in case of 100 frames acquired before the minimum (so the

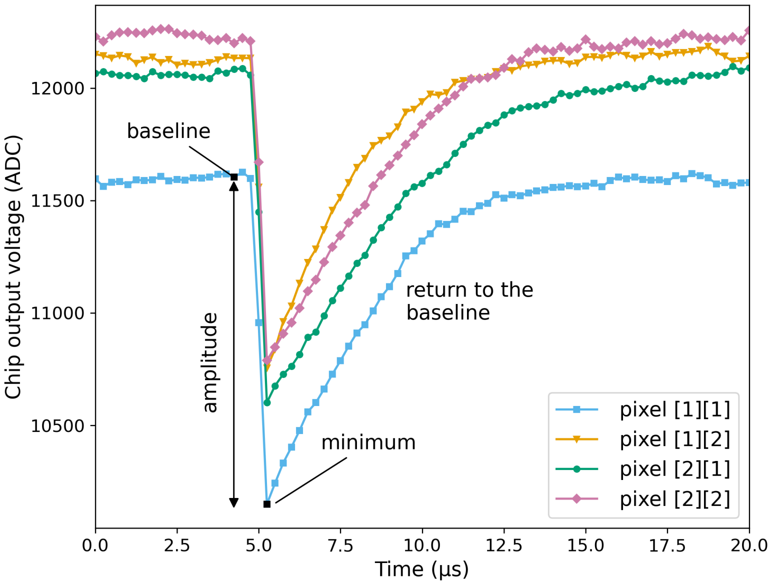

Figure 4.6: Typical waveforms from the 4 innermost pixels of an APTS chip (15 µm pitch, modified with gap, split 4). Data obtained pulsing the matrix with V_H = 1200 mV and applying a back-bias of 1.2 V. Taken from [106].

4^{th} frame before the minimum corresopnds to the 96^{th}), the noise is defined as the RMS obtained from the distribution of:

$$\mathrm{V}_{noise} = \mathrm{V}_{96} - \mathrm{V}_{2\times 96-m} \tag{4.1}$$

where m is the frame at which the minimum of the waveform is located. The substraction of the baseline (V_{96}) was done to center the distribution around zero.

An example of this distribution is shown in Figure 4.7, evaluated over a sample of about 1.5 $\times 10^5$ signals and for the 4 innermost pixels of a chip produced with the modified with gap and split 4 process.

Baseline distributions for the other pixels are not depicted as no significant pixel-to-pixel differences are observed.

From Figure 4.7 it is possible to conclude that the baseline fluctuations are similar for all the pixels, thus in the following only results obtained as an average on the 16 pixels will be reported.

Figure 4.8 shows the signal-to-noise ratio (S/N) as a function of the back-bias voltage; it was obtained by injecting a pulse with V_H = 1200 mV, for different V_sub and different chip designs. It is worth noting that the noise ranges from ∼0.6 mV to ∼ 1.1 mV, i.e.

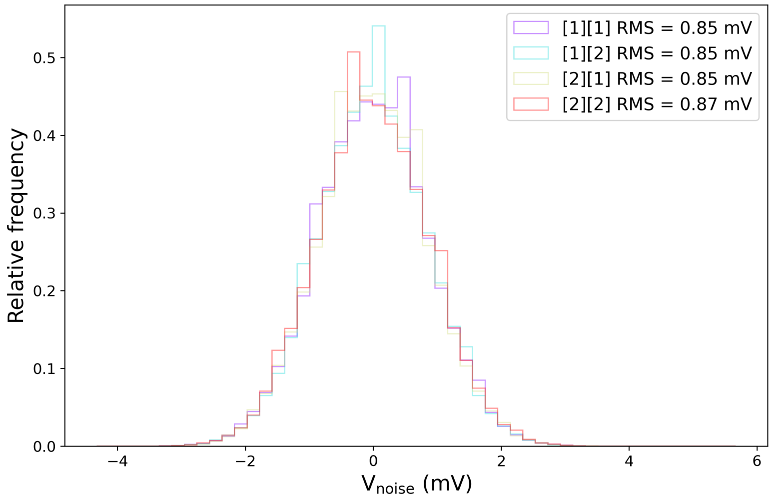

Figure 4.7: Baseline distribution for the 4 innermost pixels of a modified with gap, split 4 chip with 15 μm pitch. Data were acquired at the nominal operating point and $V_{\text{sub}} = 1.2$ V.

23 to 36 electrons, as reported in Table 4.9.

It can be observed that the S/N improves moving from 0 V to 1.2 V of back-bias voltage, in particular for modified and modified with gap, and then only slightly for higher values of back-bias. The standard chip is the variant that exhibits the highest signal-to-noise ratio, about 80, whereas the chips produced with the modified designs show a S/N ratio of around 70.

The S/N in this measurement is dominated by the capacitance at the input. A lower capacitance results in a greater excursion at the input for a given input charge, thereby reducing the noise contribution of the circuit with respect to that. The reverse bias reduces this capacitance, and in the standard version, the better depletion around the collection electrode due to the absence of the additional deep n-type implant yields a lower capacitance as well.

The conversion from mV to electrons is performed making use of the ^{55}Fe source measurements, as explained in Sect. 4.4. In the conditions under investigation, focusing on the noise values in electrons, a slight decrease of the noise with the back-bias voltage is observed, especially for chips produced with the modified processes.

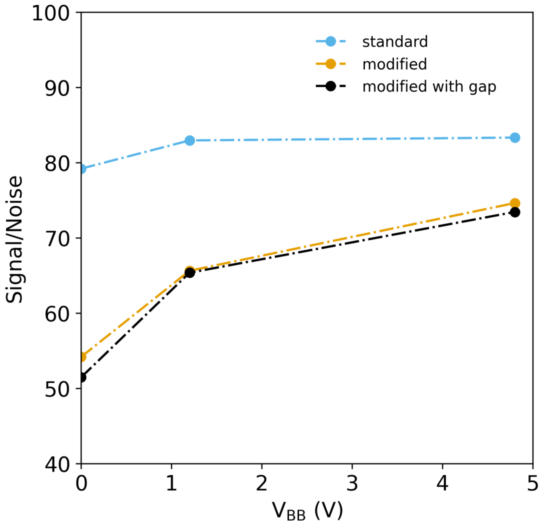

Figure 4.8: S/N ratio as a function of the back-bias voltage for the three chip designs of split 4 with a 15 μm pitch. The signal was obtained by injecting a pulse V_H = 1200 mV and it is the average of the 16 pixels response.

Noise	0 V	1.2 V	4.8 V
standard	25(0.95)	24(1.03)	23(1.11)
modified	34(0.58)	28(0.84)	24(1.13)
mod.gap	36(0.61)	28(0.85)	24(1.12)

Figure 4.9: Noise in electrons (mV) for split 4 at different V_{sub} and chip designs. The calibration in electrons was performed using data from ^{55}Fe source (see Sect. 4.4 for more details).

4.3 Front-end parameters and operating point determination

When a charge is collected by the nwell electrode, a potential drop is generated at the input node of the Source Follower (SF) circuit. This signal (V_{in}), proportional to the collected charge, is then processed through the in-pixel circuitry (see Figure 4.4), resulting in an output signal $\mathrm{V_{out}} = \mathrm{g} \cdot \mathrm{V_{in}} + \mathrm{V_o}$, where g is the overall gain of the buffering and amplifying stages and $\mathrm{V_o}$ is the offset.

The characteristics of the output signal, as well as the performance of the circuit itself, strongly depend on several currents (I_{reset}, I_{biasn}, I_{biasp}, I_{bias3}, I_{bias4}, see Figure 4.4) as well as V_{reset}, adjustable via digital-to-analogue converters (DACs) present in the proximity card (see Section 4.1.2). The I_{reset} parameter in particular requires a dedicated discussion, presented in Section 4.3.1.

A study that is crucial for the characterisation of APTS is the determination of an operating point, which corresponds to finding the most optimized set of values for the front-end parameters that can guarantee a linear response over a wide range of the input signal.

For this purpose, a systematic study of the circuit response was performed as a function of the input signal: the ouput signal was measured while V_{reset} was progressively increased from 20 mV to 900 mV.

The results are shown in Figure 4.10 for different back-bias voltages and front-end settings. Figure 4.10(a) shows the correlation between output signal, evaluated as the baseline of the signal measured at the output of the circuit, and input signal (i.e. V_{reset}).

Calculating the derivative of this correlation allows for the evaluation of the gain of the amplification stage, shown in Figure 4.10(b). Finally, Figure 4.10(c) shows the amplitude of the output signal obtained applying a pulse of $V_{\text{H}} = 1200$ mV to inject a charge in the pixels.

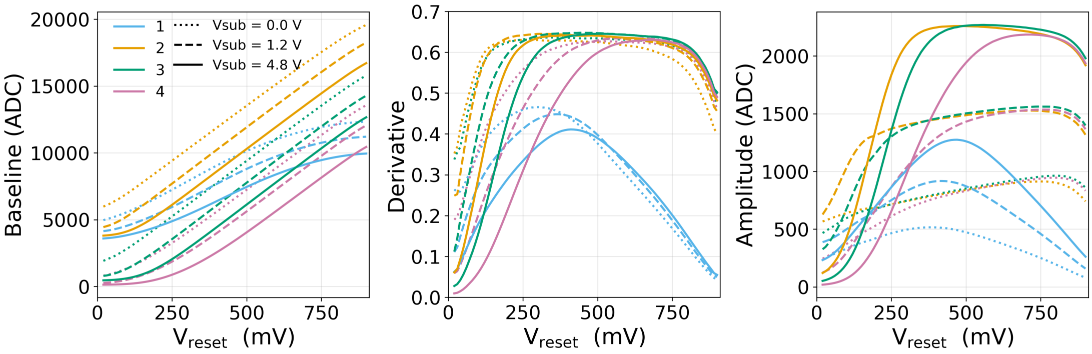

(a) Baseline vs V_{reset} (b) Gain vs V_{reset} (c) Amplitude vs V_{reset}

Figure 4.10: Output signal (a), gain (b) and signal amplitude (c) as a function of V_{reset}, for different front-end parameters settings (blue, orange, green and red) and back-bias voltages (dotted, dashed and solid). All the settings have I_{reset}=100 pA (see Section 4.3.1). The settings values are reported in Table 4.2.

The first measurements were carried out using the nominal design setting (Setting 1, see Table 4.2), but it is clear that working with these parameters does not allow the circuit to operate linearly in a wide range of V_{reset} (blue curves). This effect is even more evident looking at the plot of gain versus V_{reset} (Figure 4.10(b)). Not only the maximum gain achieved is less than 0.5, but it is not possible to find a V_{reset} range in which the gain is constant, or in other words, in which the circuit operates linearly. The amplitude of the output signal in Figure 4.10(c), at a given back-bias voltage, should be constant as a function of V_{reset}; on the contrary, in the case of the nominal design settings, no constant behaviour is observed in almost the whole range explored.

The observed behavior of the design setting can be partially explained by limitations of the simulation models used during the design phase, which lacked accuracy under certain conditions.

Settings	$I_{\textbf{biasn}}$ (μA)	$I_{\textbf{biasp}}$ (μA)	$I_{\textbf{bias3}}$ (μA)	$I_{\textbf{bias4}}$ (μA)
Setting 1	200	20	800	6000
Setting 2	5	0.5	200	150
Setting 3	5	0.5	5	150
Setting 4	5	0.5	5	1000

Table 4.2: Some of the front-end settings explored for the determiantion of the operation point of APTS.

Thanks to a systematic investigation, it was found that the linearity of the circuit was substantially improved by decreasing the supplied currents, especially I_{biasn} and I_{biasp}. Figure 4.10 reports the results for some of the settings investigated (curves in orange, green and red). Compared to the design settings, these result in a higher gain (of the order of 0.6) which is maintained constant in a larger range of V_{reset}. Among these settings, the best is the one reported in orange (Setting 2, see Table 4.2), which was chosen as an operating condition for the APTS chips: the linearity range here extends from 300 mV to 600 mV. The found operating settings differ substantially from the nominal ones, implying that this study for the determiantion of the operation point was fundamental for an optimized performance of the chip.

The settings reported in Table 4.2 and Figure 4.10 are only a small fraction of the several possible combinations. A much deeper investigation was carried out exploring large ranges for all the front-end parameters, thus moving to a larger phase space since 5 parameters were simultaneously investigated.

In total several thousands of settings were explored. This procedure was automatized and aimed at maximizing both the gain value and the range of V_{reset} in which the gain is stable. The results are reported in Figure 4.11, where the maximum gain and the V_{reset} range in which the gain is stable are shown for all the possible combinations of front-end settings. This V_{reset} range was evaluated as the range in which the gain value is inside a 1% variation from the maximum of the gain.

The region highlighted in red is the preferred one, as it ensures values of gain higher than 0.55 and a range of stability higher than 180 mV.

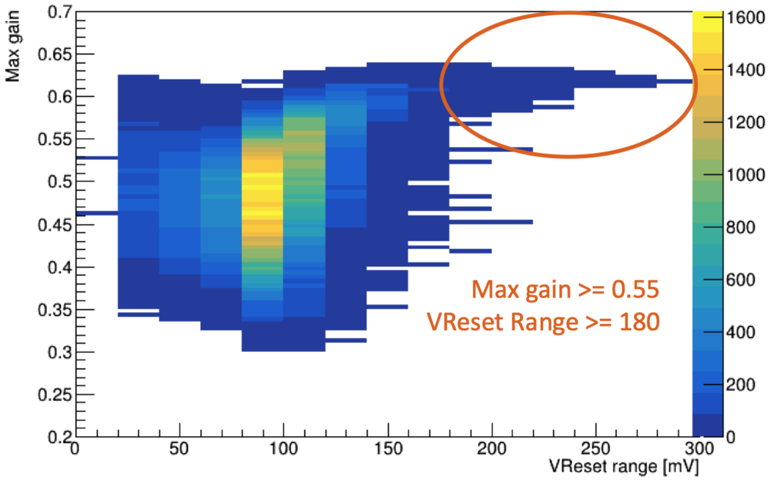

Figure 4.11: Density plot illustrating the maximum gain and the V_{reset} range in which the gain is stable across all the possible combinations of front-end settings. The region highlighted in red is the prefered one, as it ensures values of gain higher than 0.55 and a range of stability higher than 180 mV.

The final setting, chosen as operating point and already discussed, is the result of this investigation and belong to this highlighted region of the density plot.

Once the working conditions were found, a calibration procedure to correct the data for the gain was implemented. Every time a chip is connected to the acquisition system and before any new measurement, a gain curve (as the ones reported in 4.10(a) and 4.10(b)) is measured. The (V_{in}, V_{out}) points are interpolated using a cubic function, obtaining the transfer function that can be used to convert the signals from ADC counts to voltage of the collection electrode (mV). In addition, these plots turned out to be useful plots for fast data quality checks, when testing a new chip sample.

All the results that will be presented in the next sections exclusively report gain calibrated signals, acquired at the chosen operating point.

4.3.1 $\mathbf{I_{reset}}$ tuning

As shown in Figure 4.4, the front-end chain includes the possibilty to reset the collection electrode, restoring the input baseline to the V_{reset} value. At rest the current I_{reset} only compensates the sensor leakage current, and the DC voltage on the collection electrode is close to V_{reset}. Only after a hit a current I_{reset} larger than the sensor leakage is delivered: the difference between the two is then used to reset the pixel.

The I_{reset} parameter primarily controls how quickly the signal returns to the baseline (refer to Figure 4.6). Modifying the I_{reset} value has a significant impact on two key factors: the compensation of the leakage current and the energy resolution.

Leakage current compensation The leakage current of the chip is expected to increase with irradiation level and temperature (see Section 3.2). The increased leakage current effectively reduces the fraction of I_{reset} available as reset current, and influences the baseline. But if I_{reset} is increased this effect can be compensated.

To better understand this, a first set of measurements was performed with $I_{\mathrm{reset}} = 100$ pA by sending an input pulse and comparing the waveforms of the resulting signal at different temperatures, ranging from 15 to 40 °C. This was done for multiple chips irradiated at different levels of NIEL. The temperature was set using a chiller with water as coolant and the starting value was chosen as the lowest possible considering the limit given by the dew point in the laboratory environment.

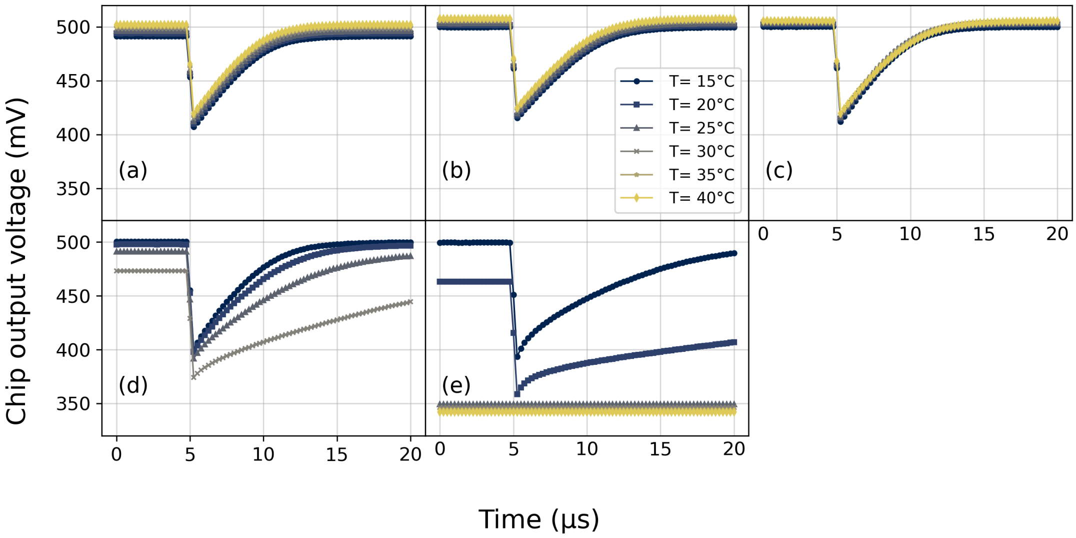

Figure 4.12: Comparison at different temperatures of the signal waveform (averaged over 1000 events) for chips at different irradiation levels: Not irradiated (a), 10^{13} 1MeV $\mathrm{n_{eq}}$ cm^{-2} (b), 10^{14} 1MeV $\mathrm{n_{eq}}$ cm^{-2} (c), 10^{15} 1MeV $\mathrm{n_{eq}}$ cm^{-2} (d), $2\,10^{15}$ 1MeV $\mathrm{n_{eq}}$ cm^{-2} (e).

As shown in Figure 4.12 the effect of the increasing leakage current starts to be visible in the waveform for levels higher than 10^{15} 1MeV $\mathrm{n_{eq}}$ cm^{-2} and it gradually increases with the temperature. In particular, the increased leakage current affects not only the baseline but also the falling edge of the waveform, making it slower.

Furthermore, as shown in Figure 4.12 some of the signals are not present at extreme conditions. This happens because at these conditions the reset current is not high enough to compensate for the leakage current. For example no signal was observed for the chip irradiated at 10^{16} 1MeV n_{eq} cm^{-2} at any temperature.

Increasing the value of I_{reset} from 100 pA to 250 pA (the maximum value supported by the present test system) the leakage current can be, at least partially, compensated and its effect on the waveform mitigated, as shown in Figure 4.13.

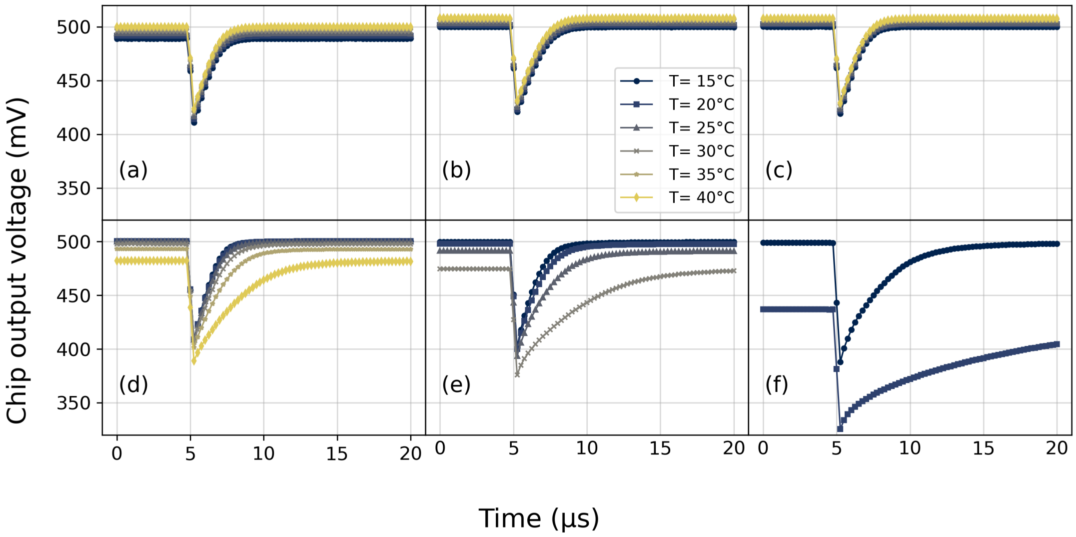

Figure 4.13: Comparison at different temperatures of the signal waveform (averaged over 1000 events) for chips at different irradiation levels, using an optimized working point (I_{reset} = 250 pA): Not irradiated (a), 10^{13} 1MeV n_{eq} cm^{-2} (b), 10^{14} 1MeV n_{eq} cm^{-2} (c), 10^{15} 1MeV n_{eq} cm^{-2} (d), $2\,10^{15}$ 1MeV n_{eq} cm^{-2} (e) and 10^{16} 1MeV n_{eq} cm^{-2} (f). Taken from [106].

This configuration also allows to recover the signal in the chip irradiated at 10^{16} 1MeV n_{eq} cm^{-2}.

From these considerations one could conclude that for irradiated chips the ideal value of I_{reset} is the highest possible, but as mentioned before there is another effect to be taken into account: the energy resolution dependecy.

Energy resolution dependecy on I_{reset} It is important to notice that changing I_{reset} impacts the energy resolution as well. Measurements of capacitance and energy resolution for different values of I_{reset} were performed using an ^{55}Fe source (see Section 4.4 for more details) and are shown in Figure 4.14. An increase of the capacitance for higher I_{reset} can be easily observed, which is not yet fully understood, as well as a degradation on the energy resolution.

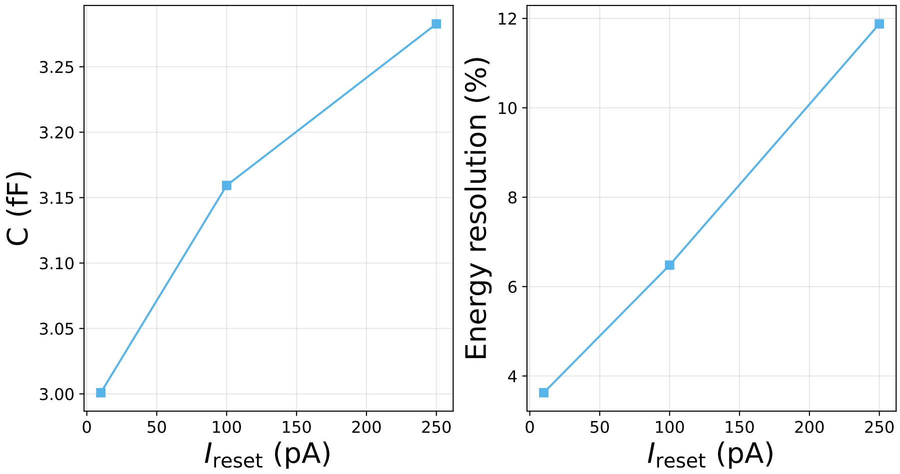

Figure 4.14: Capacitance (left) and energy resolution (right) comparison between different I_{reset}. APTS with 15 µm pitch, modified with gap, split 4, reference variant, $V_{\text{sub}} = 1.2$ V, standard readout.

As mentioned earlier the higher current affects the return to baseline of the signal, making it faster, which is an important effect on the energy resolution of the test system. This is due to the sampling frequency and to the algorithm used for the signal extraction, described in Section 4.2, which is based on the search for the minimum of the waveform. Keeping the sampling frequency constant, the definition of a minimum will be more precise when the return to baseline of the signal is slower, thus a lower I_{reset} results in a better energy resolution. A detailed study on this effect is described in Appendix B.

To conclude, it is clear that increasing I_{reset} is beneficial in terms of leakage compensation but at the expense of energy resolution. Conversely, decreasing it results in excellent energy resolution but reduces the ability to compensate for leakage current in highly irradiated chip.

Therefore, in this thesis, measurements which strongly benefit from high energy resolution were obtained with a I_{reset} of 10 pA (e.g. Figure 4.16). Other measurements were carried out at 100 pA except for radiation levels of 2×10^{15} 1 MeV n_{eq} cm^{-2} and higher that had to be carried out with a I_{reset} of 250 pA to compensate the increased leakage currents.

4.4 ^{55}Fe measurements

An extensive campaign of measurements was performed in the laboratory using a ^{55}Fe source. The source was placed at a distance of about 1 cm from the chip, thanks to a source holder that was specifically designed for this setup, shown in Figure 4.15. The data taking was performed using the internal trigger mode discussed in Section 4.1.2, which consists of triggering on the APTS signal itself. The goal of this study is to evaluate the performance of the chip in terms of charge collection and energy resolution and to compare the performances of all the available variants.

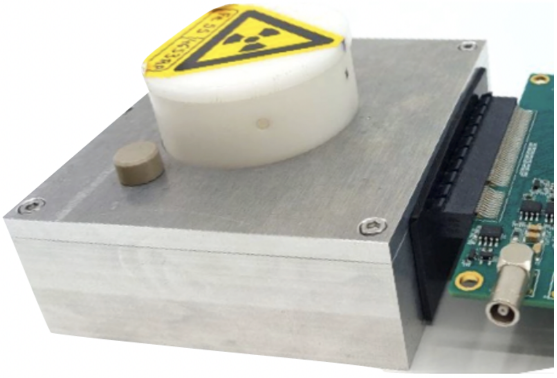

Figure 4.15: ^{55}Fe source setup. The source is placed on top of a source holder which contains the chip and covers it from the light. The distance between the source and the chip is of around 1 cm.

^{55}Fe decays via electron capture to ^{55}Mn. As discussed in detail in Section 3.3.2, the spectrum shows two main peaks corresponding to two X-rays emissions: Mn-K$_\alpha$ with an energy of 5.9 keV and a probability of about 28%, and Mn-K$_\beta$ with a nominal energy of 6.49 keV and a probability of about 2.85% [112]. The Mn-K$_\alpha$ creates an average of 1640 e-h pairs while the Mn-K$_\beta$, an average of 1800. In addition to this, for a high statistic (around $2{\cdot}10^6$ events) run it is possible to observe the Si-K$_\alpha$ peak at 1.74 keV and the escape peak at 4.16 keV in the spectrum.

The ^{55}Fe spectra reported in this study are obtained as the signal distributions of the seed pixel, which is defined as the pixel with the largest collected charge inside a cluster. The cluster is defined as a set of adjacent pixels inside a 3×3 matrix around the seed, which collected an amount of charge higher than a certain threshold. In order to avoid edge effects and have access to all pixels in the cluster, only clusters having as seed one of the central 4 pixels are considered.

4.4.1 Energy calibration

An example of a ^{55}Fe spectrum is shown in Figure 4.16(a).

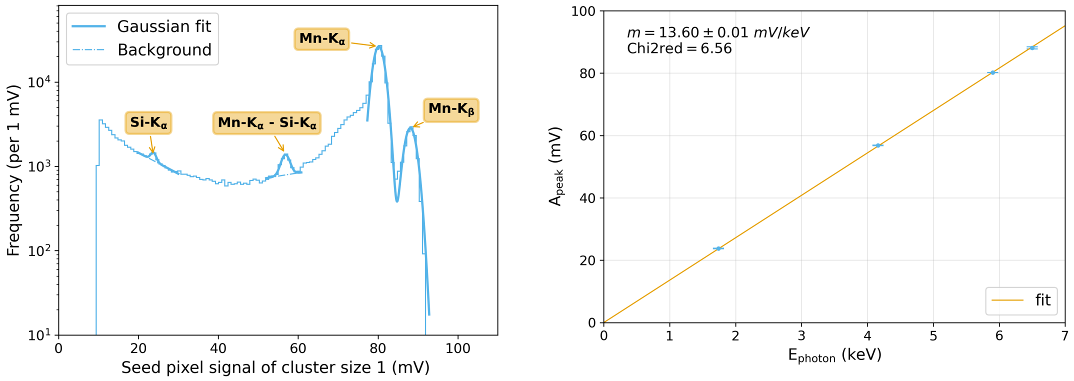

(a) Example of a ^{55}Fe spectrum and the Gaussian fits applied to its peaks.

(b) Energy calibration

Figure 4.16: (a) An example of a ^{55}Fe spectrum with the four peaks corresponding, starting from the left, to the: Si-K$_\alpha$, escape peak (Mn-K$_\alpha$ - Si-K$_\alpha$), Mn-K$_\alpha$ and Mn-K$_\beta$. The final seed distribution is filled with the seed signals of the 4 central pixels of the matrix. This plot was obtained using a modified with gap chip with a pitch of 15 µm at a back-bias voltage of 1.2 V. (b) Energy calibration obtained using the peak means from the Gaussian fits on (a). The errors on the peak amplitudes are the ones resulting from the parameter evaluation of the Gaussian fits. Data are fitted with a linear function, with the offset set at zero and m as the slope parameter. All these data were taken at $I_{\text{reset}} = 10$ pA for a better energy resolution as anticipated in Section 4.3.1. Adjusted from [106].

This particular distribution was obtained from a high-statistic dataset, in order to establish the linearity of the energy calibration by fitting all four peaks with a Gaussian function (with an additional background for the escape peak and the Si-K$_\alpha$ peak). The peak amplitudes obtained as means of these Gaussians are plotted in function of the associated photon energies in Figure 4.16(b), and the correlation is fitted with the following linear function:

$$\mathrm{A}_{peak} = m \cdot \mathrm{E}_{photon} \tag{4.2}$$

A more detailed study was performed exploiting X-ray fluorescence sources, which consist in including different targets in the setup to produce additional lines [113].

In particular, this method converts ^{55}Fe X-rays (mainly Mn-K_α) to other K_α lines using different materials as targets in between the source and the sensor . The setup used for these measurement is schematized in Figure 4.17.

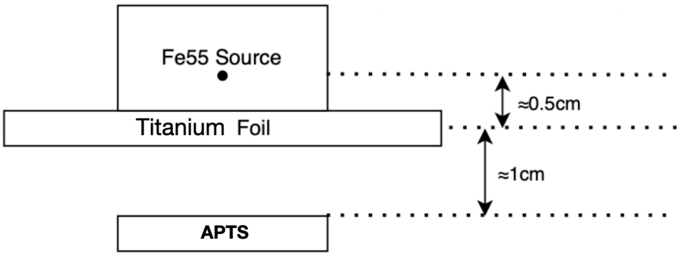

Figure 4.17: Schematic illustration of the setup used for the ^{55}Fe measurements with a Titanium foil target.

The two materials chosen for these measurements are Titanium and PVC. In the first scenario, the Mn-K_α energy is large enough to excite titanium and the photoeffect cross section for Ti-K_α is smaller than for Mn-K_α, resulting in less reabsorbtion. For this reason the Mn peaks disappear completely resulting in a clean Titanium beam. For what regards the PVC, this material is composed of a large percentage of chlorine [114], here the Cl-K_α absorbtion is stronger than the Mn-K_α one, but the chlorine peaks remains visible. For the titanium and PVC targets, foils of 75 µm and 116 µm were chosen respectively. The spectra obtained with the three different scenario of no target, titanium and PVC are compared in Figure 4.18.

As expected, in the titanium distribution the Mn peaks disappear and they are replaced by the titanium ones, while in the PVC one the Cl-K_α is visible at around 38 mV. Fitting these peaks with the Gaussian function allow to use three additional points in the energy calibration linear fit shown in Figure 4.16(b). The results of this calibration is reported in Figure 4.19 and it shows both the linear fit and the residuals.

Asserting the linearity of the energy calibration was a fundamental step in order to allow the conversion factor method explained later in Eq.4.3.

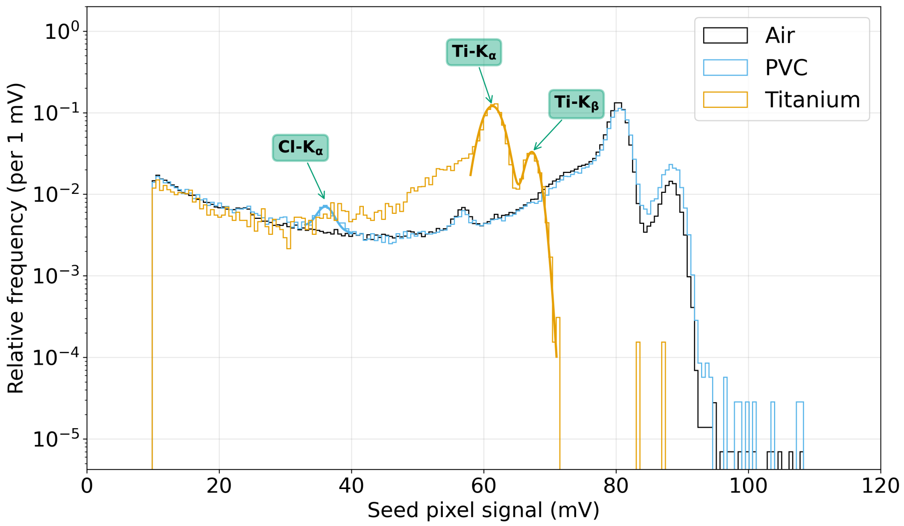

Figure 4.18: Seed signal distribution comparison among different fluorescence sources. The additional 3 peaks (of Ti-K$_\alpha$, Ti-K$_\beta$ and Cl-K$_\alpha$) are fitted with Gaussian functions. This plot was obtained using a modified with gap chip with a pitch of 15 µm, also a value of $I_{\text{reset}} = 10$ pA was chosen for a better energy resolution.

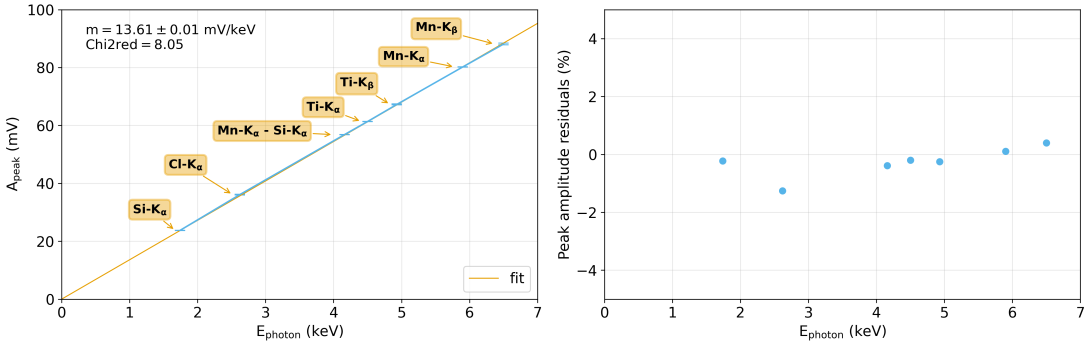

Figure 4.19: On the left the energy calibration performed using different targets scenario to add K$_\alpha$ lines. The points are fitted with a linear function with the offset set to 0 and m as the slope parameter. The errors on the peak amplitudes are the ones resulting from the parameter evaluation of the Gaussian fits. On the right the associated residuals in percentage.

Using high-statistic datasets ($2{\cdot}10^6$ events) was crucial for the energy calibration study but given the amount of measurements needed to explore all the APTS variants the statistic had to be lowered of a factor 10, in these conditions the Si-K_α and escape peak are not visible anymore. For this reason, the final seed signal distribution is usually fitted using a double Gaussian function, one for each peak of the spectrum, Mn-K_α and Mn-K_β (as visible in Figure 4.20(a)). The mean of the main peak obtained from the fit is then used to convert mV into electrons as follows:

$$\mathrm{V}_{\text{electrons}} = \frac{\mathrm{V}_{\text{mV}} \cdot 1640}{\mathrm{V}_{1640(\text{mV})}} \tag{4.3}$$

Where $\mathrm{V}_{\text{electrons, mV}}$ is a generic seed pixel signal expressed in electrons or mV and $V_{1640(\text{mV})}$ is the mean obtained using the Gaussian fit on the peak at 1640 electrons expressed in mV.

4.4.2 Variants comparison

The data taking for the ^{55}Fe measurements involved all APTS variants available and a back-bias voltage scan from 0 to 4.8V. Before each source scan the gain measurement was taken as described in Section 4.3.

Comparing the spectra of different APTS variants is extremly useful for determining the most optimized design in terms of charge collection performance. For all the comparison plots shown in this section, the distributions were normalized by the total number of events.

In Figure 4.20 a comparison among different back bias voltages is reported. From 4.20(a) is visible how the amplitude increases with the voltage; this is due to the increase of the depletion region and the consequent reduction of capacitance. If plotted in electrons, as in Figure 4.20(b), the shape of the distributions can be better appreciated, and no visible change with the back bias is observed.

In Figure 4.21 different implant geometries are compared: standard, modified and modified with gap process.

The plot shows that there is a major difference between the signal distribution of the standard process and the one of the modified. In particular, the distribution for the standard one is dominated by a charge sharing contribution, visible in the signal region around 600 electrons. This difference was expected considering that the modified processes were optimized with the exact aim of better collecting the charge both vertically and laterally.

The APTS prototypes were also produced at different process splits (1, 2, 3 and 4), as described in 4.1.

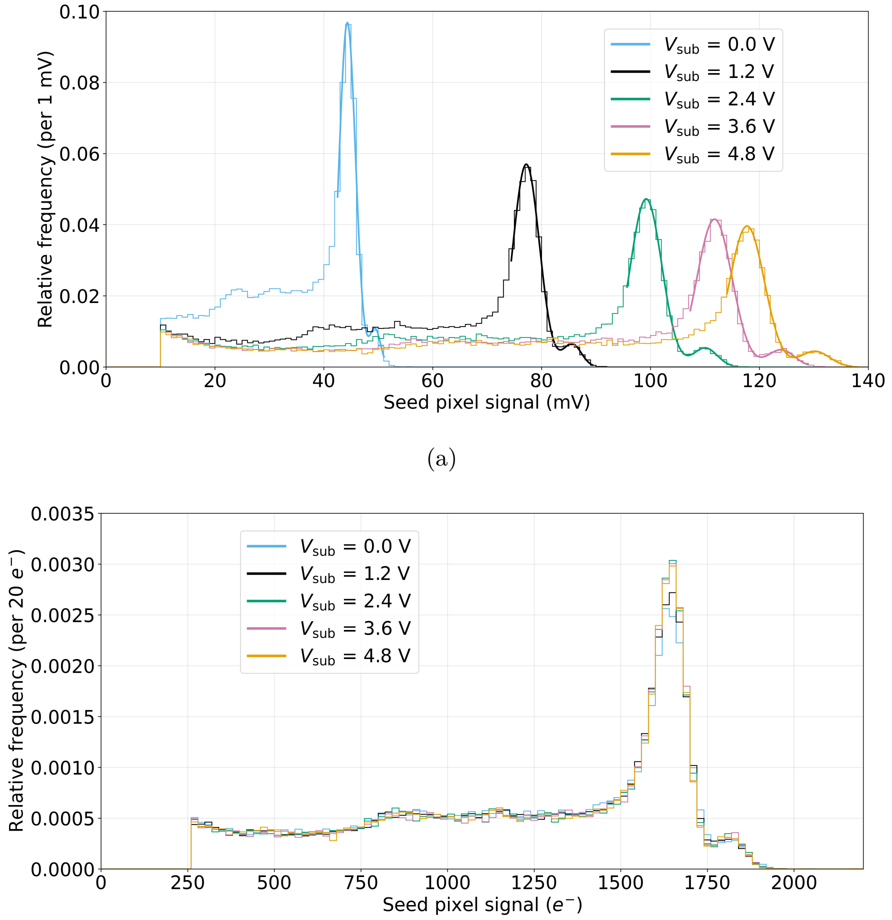

(a)

(b)

Figure 4.20: Seed signal distribution comparison between different back bias voltages, both in mV (a) and in electrons (b). This plot was obtained using a modified with gap chip with a pitch of 15 µm. Adjusted from [106].

The main difference observed between these variants is that split 1 and 2 feature a significantly lower amplitude compared to split 3 and 4, as shown in Figure 4.22(a). For these measurements the reverse substrate voltage has been fixed at $V_{\mathrm{sub}} = 4.8$ V. This was necessary because for splits 1 and 2 the signal only becomes visible at voltages larger than 3.6 V, due to the larger capacitance causing a reduction of the signal amplitude. The splits 3 and 4 are not subject to this larger capacitance and are considered better choices in terms of chip performance.

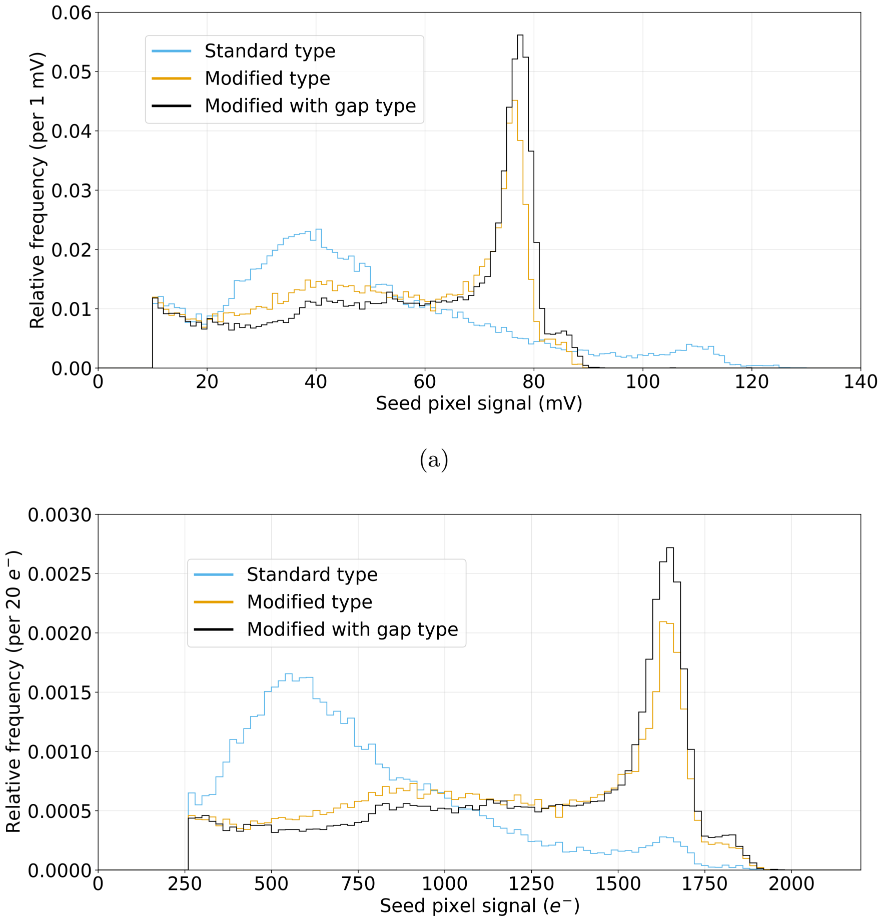

(a)

(b)

Figure 4.21: Seed signal distribution comparison between different implant geometries, both in mV (4.21(a)) and in electrons (4.21(b)). This plot was obtained using chips with a pitch of 15 µm and at a back-bias voltage of 1.2 V.

Another comparison is among different pixel pitches, represented in Figure 4.23 for all the designs. For each design, no difference in the position of the Mn-K$_\alpha$ in mV has been observed with different pitches; for this reason, only the spectrum in electrons has been reported. The different implant geometries show different results when comparing the pixel pitches.

For the standard process, smaller pitches feature better performances in terms of charge collection, with higher pitches resulting in a higher charge sharing contribution and a visible degradation of the Mn-K_α peak.

For the modified design, the charge collection is visibly improved with respect to

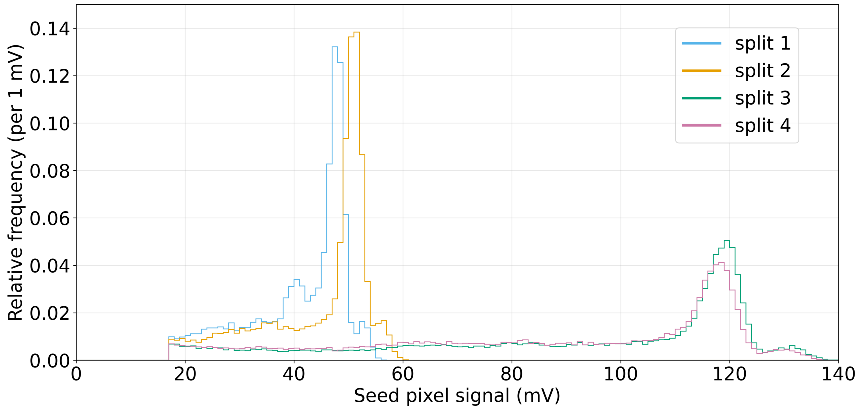

(a)

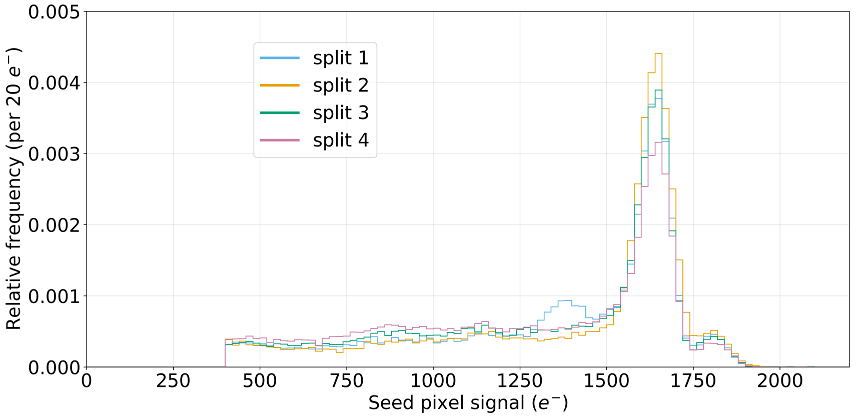

(b)

Figure 4.22: Seed signal distribution comparison between different doping profiles, both in mV (4.22(a)) and in electrons (4.22(b)). This plot was obtained using modified with gap chips with a pitch of 15 µm and at a back-bias voltage of 4.8 V.

the standard: the charge sharing contribution is smaller and the Mn-K_α peak more pronounced. The degradation is almost negligible going from 10 µm to 15 µm, while it is more appreciable moving to 25 µm pitch.

In contrast, the modified with gap has a charge collection performance that is independent of the pixel pitch. Nevertheless, this time moving from smaller to lager pitches, the charge collection performance slightly improves.

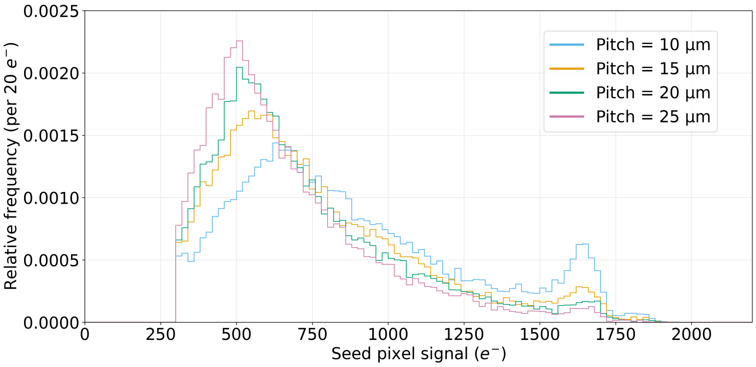

(a) Standard.

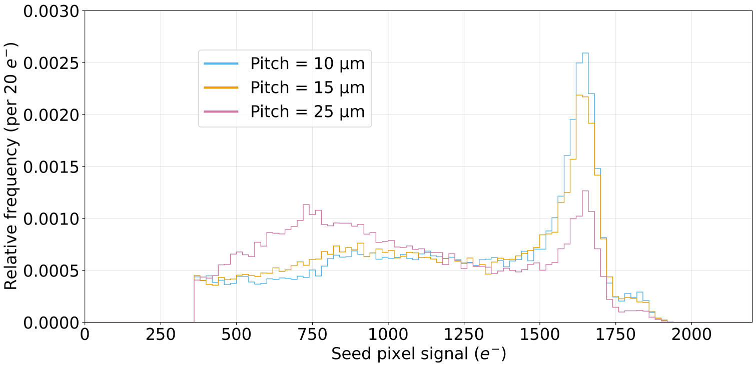

(b) Modified.

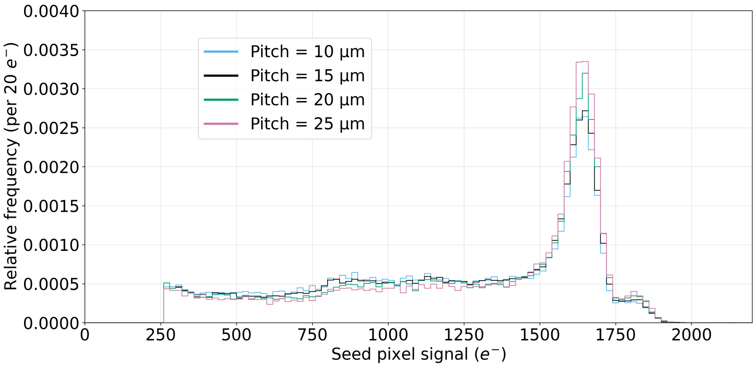

(c) Modified with gap.

Figure 4.23: Seed signal distribution in electrons compared between different pixel pitches for the standard (a), modified (b) and modified with gap (c) designs. These plots have been obtained with a back-bias voltage of 1.2 V.

Irradiation comparison

Different levels of NIEL irradiation have also been compared, see Figure 4.24, in order to assess the radiation hardness of the APTS chip. For these measurements the chips were connected to a water chiller with a temperature set to T $= 14°C$. The following measurements were taken for a modified with gap chip and, for levels of irradiation higher than 10^{15} 1MeV $\mathrm{n_{eq}}$ $\mathrm{cm^{-2}}$, at $I_{\mathrm{reset}} = 250$ pA (see Section 4.3.1).

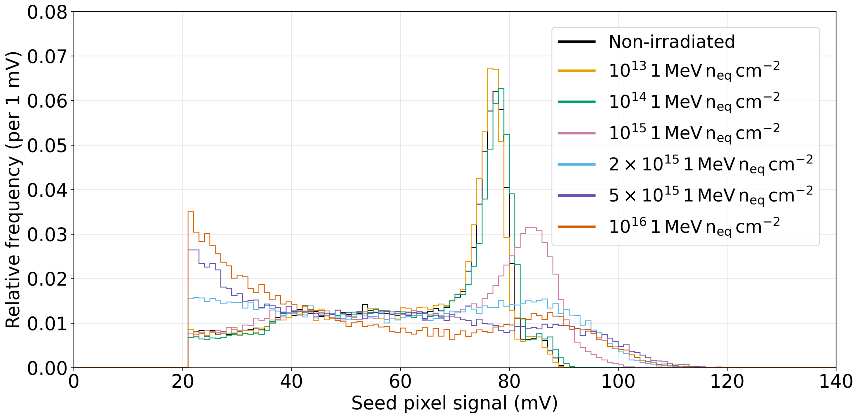

(a)

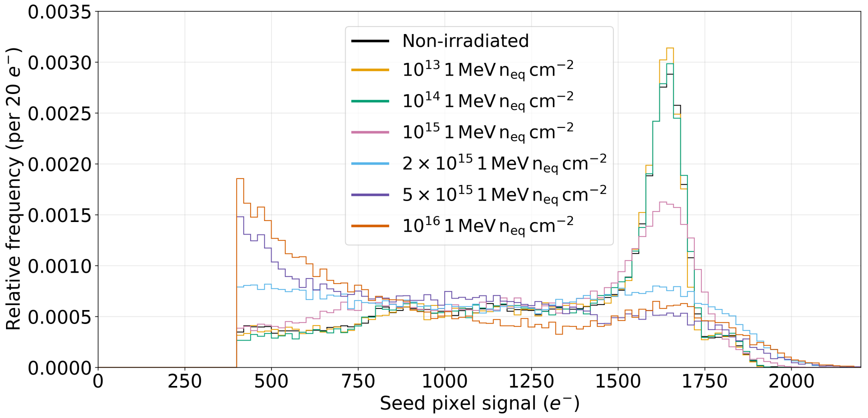

(b)

Figure 4.24: Seed signal distribution comparison between different levels of NIEL irradiation, both in mV (4.24(a)) and in electrons (4.24(b)). This plot was obtained using modified with gap chips with a pitch of 15 µm and at a back-bias voltage of 1.2 V. For irradiation levels of 2 10^{15} 1 MeV $\mathrm{n_{eq}}$ $\mathrm{cm^{-2}}$ or higher, the measurements have been taken with $I_{\mathrm{reset}} = 250$ pA (see Section 4.3.1).

Remarkably, for all the irradiation levels, the chips continue to work. More importantly, comparing the NIEL ALICE ITS3 requirement (10^{13} 1 MeV n_{eq} cm^{-2}) with the not irradiated scenario, no major difference is observed in the signal distribution, confirming that the radiation hardness requirement is satisfied for this application.

For higher levels the capacitance becomes lower (so the signal is increasing); which could be due to a reduction of the radiation-induced effective active doping (see Section 3.2). Furthermore, the peak gets broader (the energy resolution is getting worse), due to the increase of noise from leakage current and to charge losses coming from an increase of the trapping centers produced by the radiation. The lost charge could also explain the incresing contribution at lower amplitudes that dominates the highly irradiated distributions.

Another interesting result emerges when comparing the pitch among irradiated chips; in particular this measurement was performed for a 10^{15} 1MeV n_{eq} cm^{-2} level of irradiation (again at a temperature of around 14°C). The comparison is depicted in Figure 4.25

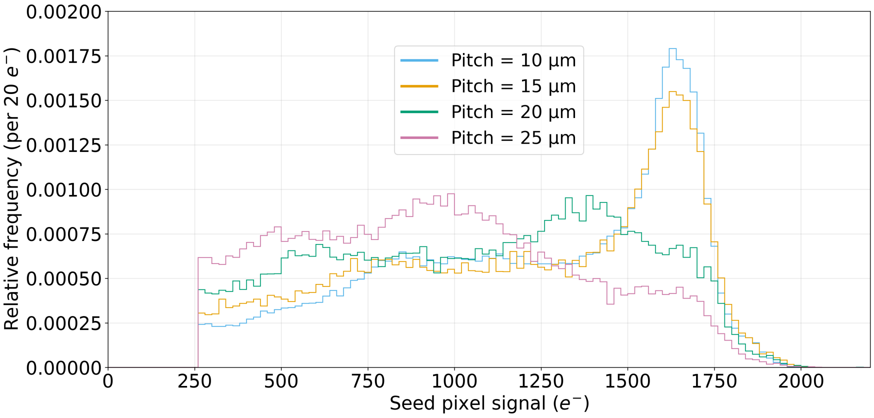

Figure 4.25: Seed signal distribution comparison between different pixel pitches of a chip irradiated 10^{15} 1MeV n_{eq} cm^{-2} in electrons. This plot was obtained using modified with gap chips and at a back-bias voltage of 1.2 V.

and shows clearly that for such irradiation level, larger pixel pitches are more affected by the irradiation compared to smaller ones. This can be concluded by looking at the deterioration of the main peak of the ^{55}Fe spectrum, a consequence of the fact that the distribution is dominated by another contribution, which probably comes from lost charge due to irradiation damages.

Summary of all variants comparisons

The variants comparisons just discussed are the most important ones for the validation of the 65 nm technology, but the number of measurements performed is much larger. Given the amount of possible combinations (different variants, voltages and irradiations) all the ^{55}Fe measurements were summarized in a single plot, shown in Figure 4.26.

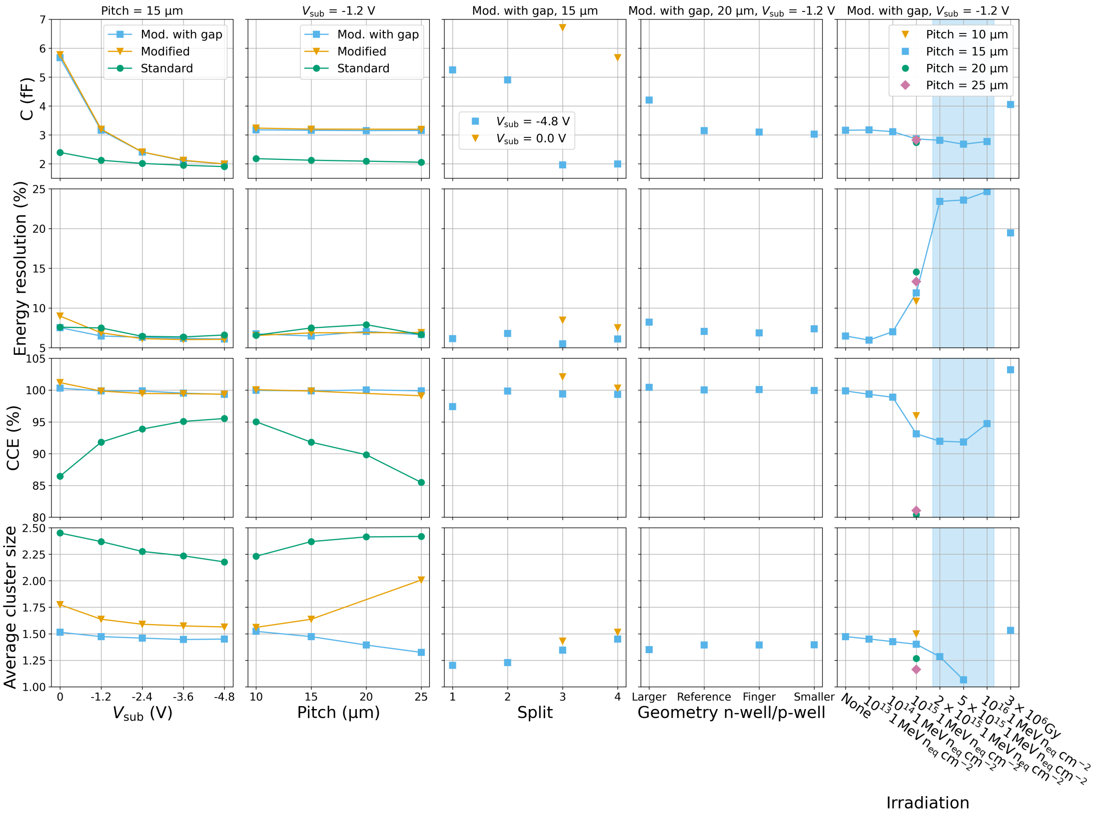

Figure 4.26: Comparison of the main characteristics extracted from the ^{55}Fe spectra. The light blue window in the last column refers to the data points acquired with $I_{\text{reset}} = 250$ pA, all the others with $I_{\text{reset}} = 100$ pA. Taken from [106].

This plot reports several quantities that were extracted from the ^{55}Fe spectrum:

- **Input capacitance** (first row): related to the measured capacitance as in Eq. 4.4.

$$C_{\text{input}} = C_{\text{measured}} - C_{\text{injection}} = \frac{n_{\text{el}} \cdot q_{\text{el}}}{V_{1640}} - C_{\text{injection}} \tag{4.4}$$

with V_{1640} (in mV) the mean of the Gaussian fit around the Mn-K$_\alpha$ peak, $n_{\text{el}} =$

1640 electrons, q_{el} the elementary charge and $C_{\mathrm{injection}}$ ~242 aF (see Section 4.1.1). This value is very important becuase a smaller input capacitance results in an higher voltage excursion at the input of the front-end circuit for a given charge. This improves the signal with respect to the noise of the front-end circuit, and also increases its reaction speed, improving S/N and power consumption.

- **Energy resolution** (second row): obtained as the FWHM (Full Width at Half Maximum) of the Mn-K$_\alpha$ peak divided by its mean, V_{1640}.
- **Charge Collection Efficiency ratio, CCE** (third row): defined as the ratio between V_{1640} and the mean of the signal distribution coming from a 3×3-pixel matrix around the seed (both obtained with Gaussian fits).
- **Average cluster size** (fourth row): calculated at a threshold of 150 electrons.

Several trends can be observed:

- The first column shows the implant geometry comparison at different back bias voltages. In the standard processes the back bias has less influence on the sensor capacitance, compared to modified processes. A possible explanation for this is that the depletion region starts extending from the junction. Therefore, in the standard design (see Figure 4.2(a)), it expands from the collection electrode outward, and reaches the p-well at low reverse bias. Due to the high p-well and n-well doping the depletion cannot extend much further. In addition, the depletion boundary extending into the epitaxial layer is at that point already significantly larger than the undepleted part of the n-well, making the dimension of the latter dominant in the capacitance calculation. This explains the small influence of the reverse bias on the sensor capacitance in the standard design.

  For the modified and modified with gap designs (see Figure 4.2(b) and 4.2(c)), the depletion starts at the junction formed by the low-dose deep n-type implant, and does not yet reach the n-well electrode at zero reverse bias. With increasing reverse bias, it extends towards the n-well electrode and significantly reduces the size of the undepleted region around the collection electrode, dominant for the capacitance value. Ultimately, the depletion also converges to near the n-well boundary as in the standard design, resulting in the same capacitance value of about 2fF.

  The energy resolution is similar for the three processes, with tendency to improve with higher voltages, still slightly better for the modified processes.
  A lower CCE is observed for the standard type, which could be due to the larger

charge sharing contribution observed in Figure 4.21. As already mentioned, the explanation for this difference lies on the optimized designs for better charge collection in modified processes. The avarage cluster size (last row) behave accordingly, resulting in higher values for the standard design.

- The second column shows the comparison of different pixel pitches. In terms of capacitance and energy resolution no pitch dependecy is observed. A better CCE is visible for smaller pitches of the standard process, in accordance to the increased charge sharing for larger pitches observed in Figure 4.23(a). Both for the standard and modified process, larger pitch results in an increase of average cluster size. Interestingly the pattern is opposite when looking at the modified with gap process. This happens because of the smaller relative size of the gap region for larger pitches, and the fact that the field induced by the gap prevents charge sharing for hits closer to the pixel center.

- The split comparison is shown in the third column at two different voltages and the only trend that is visible regards the capacitance. Split 1 and 2 have a much higher capacitance than Split 3 and 4 (lower signal amplitude as shown in Figure 4.22). For all these reasons, the split 4 variant is considered a better choice in terms of chip performance.

- Comparing the different geometries (Figure 4.3) of nwell and pwell (forth column), the only difference observed is on the capacitance (higher for the larger nwell collection electrode), otherwise all the variants show similar behaviour.

- The last column shows the comparison of different levels of NIEL irradiation (already shown in Figure 4.24) together with a TID irradaition measurement. For NIEL irradiation levels higher than $2 \cdot 10^{15}$ 1 MeV $\mathrm{n_{eq}}$ $\mathrm{cm^{-2}}$ the measurements have been taken with $I_{\mathrm{reset}} = 250$ pA, as anticipated in Section 4.3.1. If for NIEL higher levels result in a lower capacitance (increased signal), for TID the effect is the opposite and a larger capacitance is observed. The reason behind this effect is not yet fully understood but it could be found in the ionising damages described in Section 3.2. The CCE and the avarage cluster size are decreasing with NIEL, but it has to be noted that for high levels of irradiation the uncertainty on the CCE calculation method is larger due to the signal distribution deterioration observed in Figure 4.24.
  In this column also the different pitches at a fixed NIEL level, already shown in Figure 4.25, are plotted.

4.5 Testbeam

After extensive tests in the laboratory with the ^{55}Fe source, the APTS chips were also tested using beams of charged particles, in order to study the detector charge distribution and detection efficiency. This was made possible by using a telescope made of ALPIDE chips as reference planes, providing high resolution tracking reconstruction ($\sigma_{\text{track}} = 2.1\ \mu\text{m}$ [115].). In this section, results from the test beam data collected at the SPS H6 (120 GeV/c positive hadrons) will be reported.

The setup was positioned inside a box and covered, to take data in a fully dark environment. Two APTS sensors were mounted between the reference planes. A schematic illustration of the setup is shown in Figure 4.27, while a picture of the telescope box is shown in Figure 4.28.

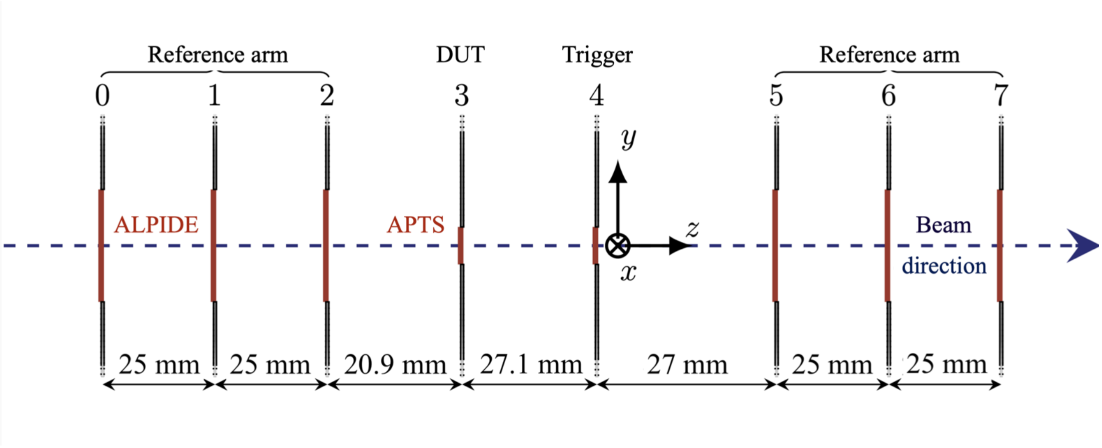

Figure 4.27: Scheme of the telescope setup used at SPS test beams in October 2022 and May 2023. Two APTS are enclosed in two groups of three ALPIDE each. The trigger is provided by one of the two APTS. Not to scale. Taken from [106].

The APTS on the third plane is the Device Under Test (DUT), while the other was used as trigger device. The DUT was operated in external trigger mode and connected with the trigger device using the DAQ board TRIGGER_IN connector, as described in Section 4.1.2.

To align the DUT with the Trigger, the DUT has been mounted on a movable stage.

The DUT temperature was kept constant using a cooling jig, which was cooled with chilled water. The water temperature was set to $T = 15$ °C; it was estimated that the effective temperature in the setup was 1 to 3 degrees higher, depending on environmental

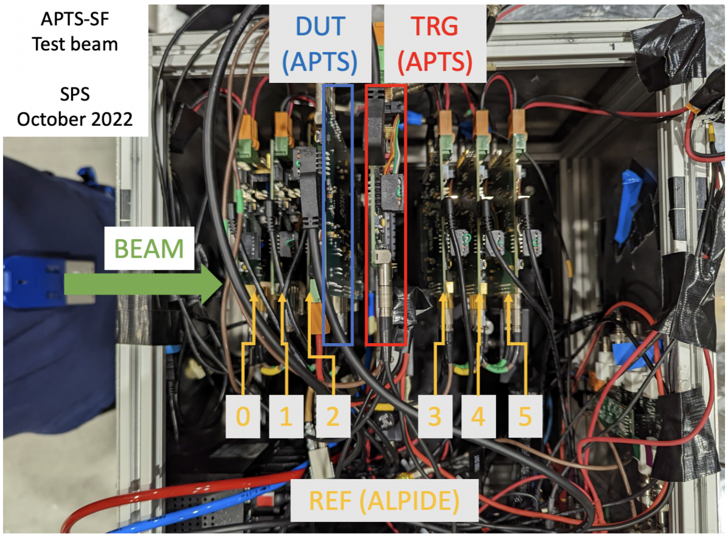

Figure 4.28: Telescope setup used at SPS test beams in October 2022 and May 2023. The setup was positioned inside a box and covered from the light.

conditions.

As a trigger device a non-irradiated, modified with gap APTS of 25 µm pitch was operated at $V_{\text{sub}} = 1.2$ V.

For each event collected, the pixels above threshold in the ALPIDEs were saved and the formed clusters are used to reconstruct the tracks crossing the DUT. In particular for the reconstruction of tracks and detection efficiency evaluation, the data were analysed using the Corryvrecan [116] framework. The analysis tools and event selection procedure are detailed in [106, 117].

4.5.1 Charge distribution

In Figure 4.29, the seed pixel signal distributions for the different APTS designs and irradiation levels at $V_{\text{sub}} = 1.2$ V are shown. A expected, their shape is similar to the Landau distribution (Section 3.3).

In the top left figure the implant geometry comparison is depicted and it shows that going from the standard design to the modified and modified with gap, the Most Probable Value (MPV) for the seed signal increases, improving the signal-to-noise ratio by a factor 2. This is in accordance with the lower charge sharing observed in the ^{55}Fe measurements (see Figure 4.21).

The same distribution for different pitches is shown in the top right figure. For higher pitches, the MPV slightly increases, which is in accordance with the decreases in average

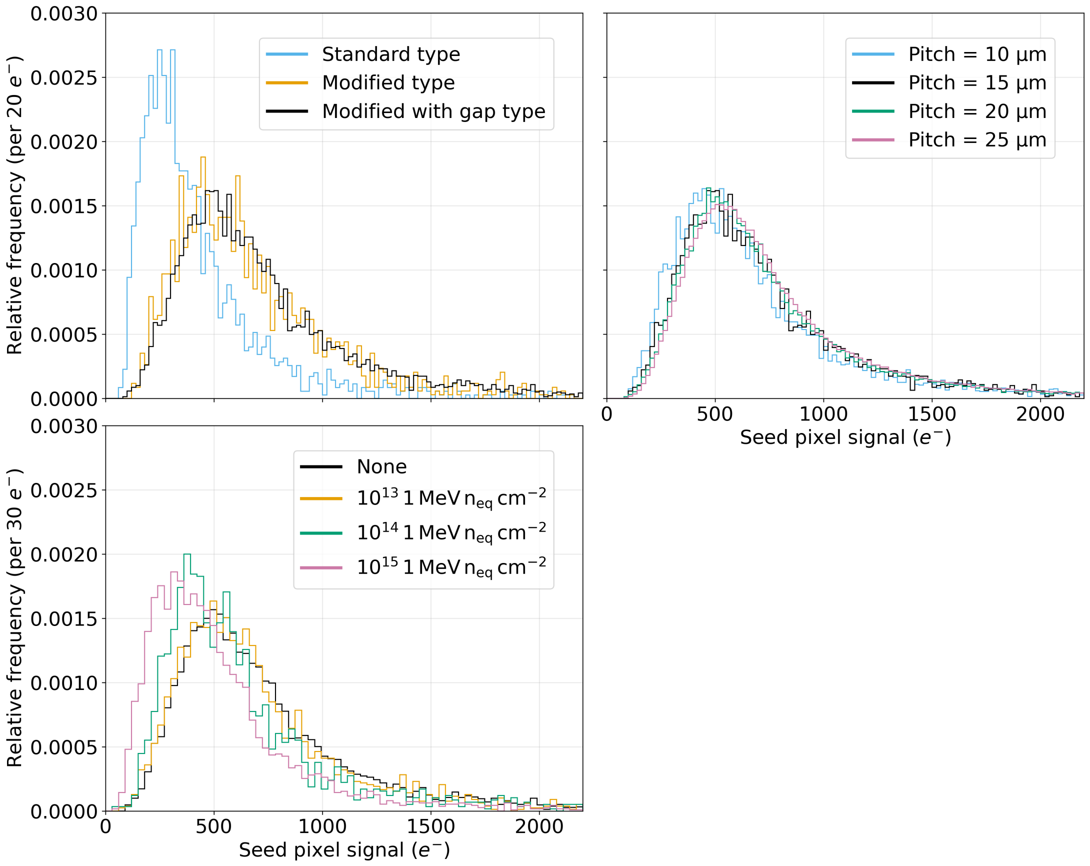

Figure 4.29: (Top left) Comparison between different designs of the seed pixel signal charge distribution for a pitch of 15 µm. (Top right) Comparison between different pixel pitch sizes of the seed pixel signal charge distribution for modified with gap sensors. (Bottom) Comparison between different NIEL irradiation doses of the seed pixel signal charge distribution for a modified with gap sensor with a pitch 15 µm. Adjusted from [106].

cluster size with increasing pitch.

Finally, different NIEL irradiation levels are compared in the bottom left figure. The main effect of increasing the irradiation is that the MPV shifts towards lower values, this is the result of the worse charge collection which becomes evident for levels higher than 10^{14} 1 MeV n_{eq} cm^{-2}. As expected also from ^{55}Fe measurements (see Figure 4.24), at 10^{13} 1 MeV n_{eq} cm^{-2} no degradation is observed.

4.5.2 Detection efficiency

The detection efficiency is evaluated as the ratio between the number of DUT clusters associated to reconstructed tracks passing through and the total number of reconstructed tracks. Only tracks passing through the 4 central pixels have been considered, in order to avoid border effects.

In Figure 4.30 the detection efficiency of 15 µm modified with gap for different values of back bias is reported as a function of the threshold. Each distribution is plotted above 3 times the noise RMS (the dotted lines indicate the threshold corresponding to this value), measured as described in 4.2. No strong dependence of the efficiency from the V_{sub} has been observed for the majority of the threhsold range. At high thresholds, a small decrease in efficiency as V_{sub} grows is visible.

Nevertheless, the threshold can be set to lower values going to higher voltages, thanks to the lower noise, as reported in Table 4.9.

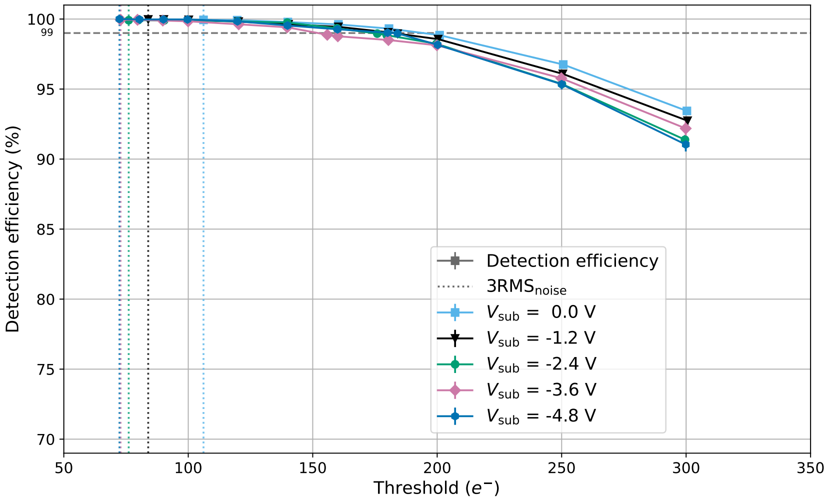

Figure 4.30: Efficiency comparison between different reverse substrate voltages as a function of the applied seed threshold. The dotted lines indicate the threshold corresponding to 3 times the RMS noise value. APTS with 15 µm pitch, modified with gap, split 4, reference variant. Taken from [106].

This has been quantitatively studied for each variant and the results are summarized in Figure 4.31. This Figure reports the following quantities (extracted from detection efficiency plots):

- **Efficiency at a threshold of 100 electrons**: if not reported, it means that 3

RMS$_{\text{noise}}$ is higher than 100 electrons.

- **Threshold** at which the chip achieves **99% detection efficiency**.
- **Noise RMS**: is the noise of the DUT. The distance between the noise and the threshold value at 99% gives an indication of the trend of the range of operability of the DUT.

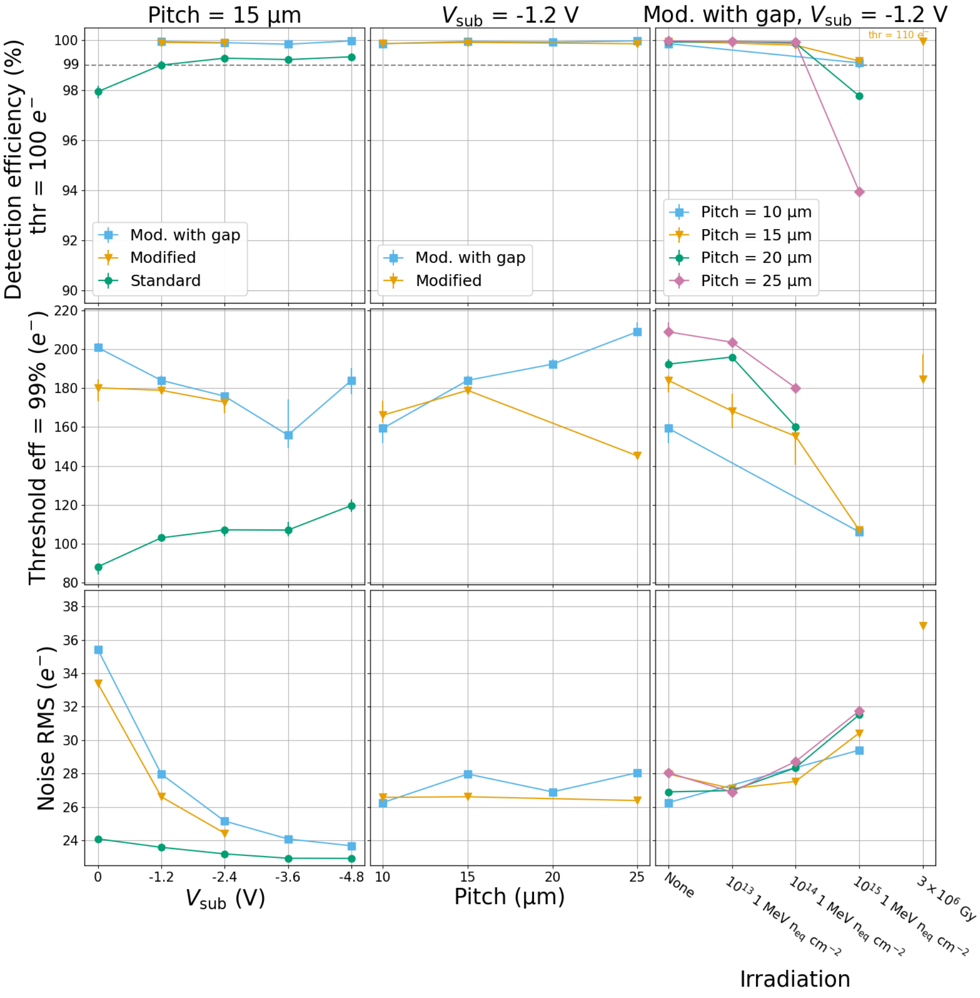

Figure 4.31: Comparison of the main characteristics extracted from the efficiency plots versus threshold. APTS with split 4, reference variant. Taken from [106].

Several trends can be observed:

- The first column depicts the comparisons between designs at different V_{sub}. The modified with gap (and similarly the modified) process, not only is able to achieve higher detection efficiencies, but also features a larger operational margin w.r.t. the standard type keeping efficiency values above 99% up to more than around 160 electrons. For the standard one instead, despite reaching an efficiency higher than 99%, the operation range is smaller. This is compatible with the results of charge collection efficiency observed in Figure 4.26.

- The influence of the pixel pitch size for the modified and modified with gap and for a fixed voltage of 1.2 V is shown in the second column. All the pitches and types reach an efficiency of more than 99%. Nevertheless a clear difference is evident going to higher pitches. In the modified design the largest pitch exhibits the smallest operational margin. Conversely, for the modified with gap the trend is the opposite, and larger pitches have wider operational margin. The reason behind this opposite behaviour is that in the modified design increasing the pixel pitch enhances the significance of charge sharing, while in the modified with gap, a larger fraction of the total number of hits will see the generated charge collected on a single pixel with increasing pixel pitch, therefore increasing the operational margin.

- All the irradiated chips tested during the testbeam campaign, regardless of the pitch, can withstand a NIEL irradiation level up to 10^{15} 1 MeV n_{eq} cm^{-2} (for all the bias voltages studied), higher than the ALICE-ITS3 requirement. In general for all the pitches, a reduction of the operation margin going to higher NIEL irradiation can be observed. Up to 10^{14} 1 MeV n_{eq} cm^{-2}, a larger operation margin can be observed for larger pitches. At 10^{15} 1 MeV n_{eq} cm^{-2} this trend is reverted, indicating a larger radiation hardness when going to smaller pitches. Indeed for a pitch of 10 and 15 µm, an efficiency higher than 99% can still be reached.
  Morever it should be noticed that up to a TID irradiation of 3 10^{6} Gy (much higher than the ALICE-ITS3 requirement and reaching the ALICE 3 requirement) the DUT has reached an efficiency higher than 99%, even if in a smaller range of operation, due to the higher noise (see last row).
  It is importnat to highlight that all these achievements with irradiated sensors are quite remarkable as the temperature was higher than 15 °C, so essentially at room temperature.

4.6 Summary

The performance of the Analogue Pixel Test Structure (APTS), developed using the TPSCo 65 nm technology, has been thoroughly investigated. The characterization of this chip aimed at validating this technology in terms of charge collection efficiency, detection efficiency and radiation hardness, and involved several variants. The different designs included variations of: implant geometries (standard, modified and modified with gap), splits, n-well/p-well geometry, and pixel pitches. These designs were subjected to testing under varying conditions of reverse substrate bias and irradiation levels, utilizing both an ^{55}Fe source and a beam test setup.

Among the designs, the modified with gap variant demonstrated superior Charge Collection Efficiency (CCE) and minimal charge sharing, resulting in smaller average cluster sizes and an enhanced signal-to-noise ratio. This design also achieved a higher operational margin in terms of detection efficiency, consistently exceeding 99% across different substrate biases and pixel pitches. An energy resolution of 5% for the Mn-K$_\alpha$ peak from ^{55}Fe was achieved.

The study revealed that both ^{55}Fe and test-beam measurements showed a deterioration of charge collection of the modified with gap design with increasing NIEL or TID irradiation doses. Nevertheless, a detectable signal peak was observed even after exposure to 10^{16} 1 MeV neq cm^{-2}. The detection efficiency remained above 99% after exposure to both TID (3×10^6 Gy) and NIEL (10^{13} 1 MeV neq cm^{-2}) requirements for ALICE ITS3. At a temperature of approximately 15°C, the design maintained an efficiency of 99% or higher for all pitches up to a NIEL of 10^{14} 1 MeV neq cm^{-2}. This efficiency was sustained up to 1×10^{15} 1 MeV neq cm^{-2} for a 15 µm pitch, and up to 2×10^{15} 1 MeV neq cm^{-2} for a 10 µm pitch.

These findings establish the TPSCo 65 nm ISC technology as a viable candidate for high-energy physics applications. The smaller feature size of this technology offers significant potential for further enhancements, and hence significant prospects for use in future high energy physics experiments.

Chapter 5

Simulation of charge collection process in MAPS

Simulation studies of MAPS are essential for understanding and optimizing their design and performance. By modeling their behavior under various conditions, these studies offer valuable insights into detector responses, which play a key part in the simulation and analysis chain in HEP experiments. Modeling the exact response of MAPS is challenging due to contributions from epitaxial layer, substrate, and well structures.

The main software tools used to generate the results for this thesis are Sentaurus TCAD [118] from Synopsys and CERN's Garfield++ [119]. This study consists of simulating the electric field of the sensor with TCAD and then use it in a Monte Carlo simulation in Garfield++ to model the charge transport mechanism and collection process. The charge collection information is then used as input in a Python program to simulate the chip response to X-rays coming from the ^{55}Fe source.

The ^{55}Fe spectrum was selected as the reference for these simulations due to its inherent complexity. This spectrum features characteristic X-ray peaks that require precise modeling to align with experimental results. Unlike simpler spectra, the ^{55}Fe spectrum challenges the simulation's ability to accurately replicate charge transport and collection mechanisms. A successful match between the simulated and experimental spectra serves as a rigorous test of the model's accuracy.

For this particular work the simulation focused on the APTS chip, but the same algorithm can be applied to different monolithic pixel prototypes. For instance, applying this framework to extract the response of the final ITS3 sensor represents a critical step. Its integration into the ALICE O^2 simulation framework [120] will enable more accurate simulations of the detector performance.

This chapter will give an overview on the simulation structure and a general introduction on the simulation tools used (TCAD and Garfield++). Additionally, it will detail the methodology and procedures employed to conduct the simulation. Finally, it will be shown that a good agreement between data and simulation of the APTS chip has been achieved for ^{55}Fe X-rays.

5.1 Simulation structure

The structure of the simulation workflow is illustrated in Figure 5.1. The first phase consists of using a TCAD (Technology Computer-Aided Design) simulation to extract the electric field of a single pixel cell of the chip. This simulation step requires as input the sensor's doping profiles and geometry parameters (such as pixel pitch and layer thicknesses), which collectively influence the electric field distribution within the pixel.

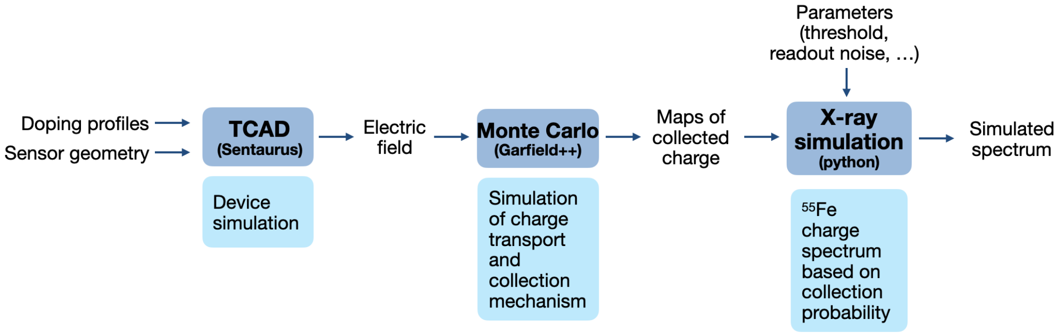

Figure 5.1: Sketch of the simulation workflow.

Following this, the electric field data serves as input to the Monte Carlo simulation in Garfield++, a specialized simulation designed to model charge transport and collection processes within the sensor. This phase simulates how the charge carriers move through the electric field and are eventually collected by the electrodes. The purpose of this step is to produce a set of charge collection maps that capture the amount of charge collected by a matrix of pixels at different deposition positions and depths across the sensor.

In the final step, these charge maps are used to model the chip's response to X-rays, specifically from the ^{55}Fe source. This involves generating a spectrum based on the charge collection behavior mapped previously and then comparing the simulated spectrum to experimental data to validate the model's accuracy.

In principle one could directly simulate the X-rays crossing the sensor using Garfield++ instead of a separate simulation algorithm, but this choice of using two separate steps has a specific purpose. By generating these charge collection maps, the simulation framework becomes more versatile and adaptable for a broad range of applications because it eliminates the need to repeat the Garfield++ simulations for each new scenario. Rather than limiting the simulation output to the specific case of X-ray photons, these maps can be reused for simulations involving different particles and conditions, making it a flexible tool for multiple experimental setups and analyses.

5.2 Device simulation - TCAD

All the simualted electric field used in this thesis were obtained using Sentaurus TCAD from Synopsys [118]. The main TCAD tools used for this purpose are:

- **SDE**, a device structure editor used to define the geometry of the sensor.
- **SNMESH**, an editor used to define the doping profiles and the meshing.
- **SDevice**, a tool used to define the physics and mathematical boundary conditions to run the simulation.
- **SVisual**, used to visualise and extract results.

5.2.1 Geometry

In order to simulate the APTS behavior under various operating conditions, it is crucial to achieve a precise geometric representation. The geometry of the pixel cell of the simulated device and its parameters are shown in Figure 5.2.

The APTS chip structure is modeled with specific dimensions for key components such as epitaxial layer, substrate and collection electrode: the dimensions of these components are predetermined based on the sensor process and are not subject to change (for example the epitaxial and substrate thicknesses and collection electrode width in Figure 5.2). But there are parameters that can be varied according to the simulated variant: for this particular work the pixel pitch and the low-dose n-type implant dimensions were varied (implant depth and gap width in Figure 5.2).

All the longitudinal parameters are defined symmetrically from the center of the collection electrode (center of the pixel). For this reason, and in order to optimize the computational resources, the simulation is performed on only one-quarter of the total pixel. This smaller region is then mirrored along both the x- and y-axes to reconstruct the full pixel, and eventually the full matrix. This approach significantly reduces simulation time while preserving the accuracy and completeness of the simulation. In principle, one eighth of the pixel is already enough to capture the behavior of the full pixel, but for

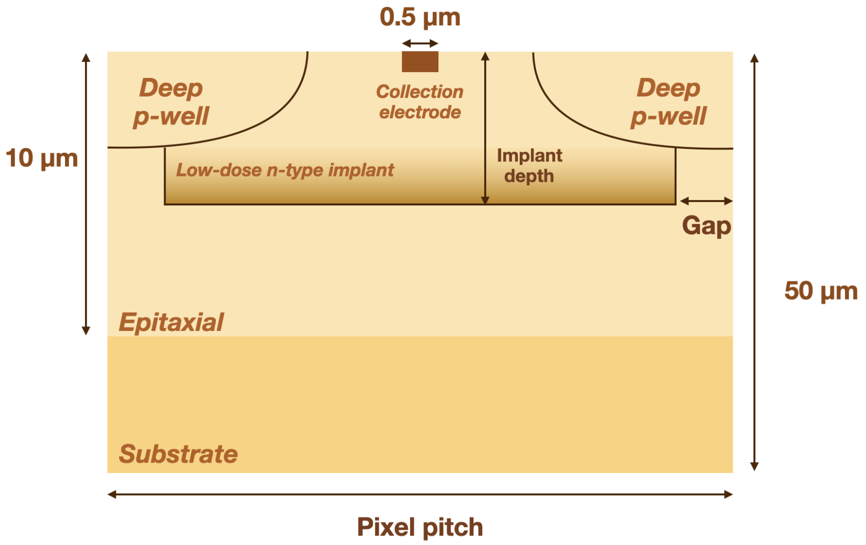

Figure 5.2: Sketch of an APTS cross section and the geometric parameters used for the TCAD device simulation. The implant depth, gap width and pixel pitch are the parameters that can be varied according to the simulated variant. Not to scale.

these studies one quarter was chosen for convenience (this applies also to the Garfield++ simulations described in Section 5.3).

To accurately model the detector, reflective boundary conditions are applied, representing the fact that each pixel cell in the actual detector is surrounded by identical neighboring pixels.

5.2.2 Doping profiles and meshing

The epitaxial layer and substrate differ not only in thickness but also in terms of charge carrier properties. These differences arise solely from the different doping concentrations of the two layers. In practice, this means higher mobility, higher diffusion coefficient, and longer carrier lifetime in the epitaxial layer. Also, the substrate is almost devoid of an electric field: the main mechanism of carrier movement here is diffusion.

For all the simulations in this study, the doping profile is known to some extent. Therefore, it is imported using SDE based on what was given to CERN by the foundry. The actual profiles are confidential.

Another key ingredient is the mesh generation (or meshing), which is the practice of dividing the simulation domain into smaller, finite elements or cells. This discretization is essential for solving the mathematical equations governing the simulated devices. Usually, the cells partition the geometric input domain to approximate the larger domain. Depending on the complexity of the domain and the type of mesh desired they are created by computer algorithms and often with human guidance through a GUI. The objective is to produce a mesh that accurately represents the geometry of the input domain, while avoiding unnecessary detail that would significantly increase simulation time. Finer meshes provide more accurate results but require more computational resources, so the mesh should be detailed in critical areas and coarser where precision is less important. Sentaurus TCAD allows automated mesh optimisation according to the device parameters like geometry or doping concentration.

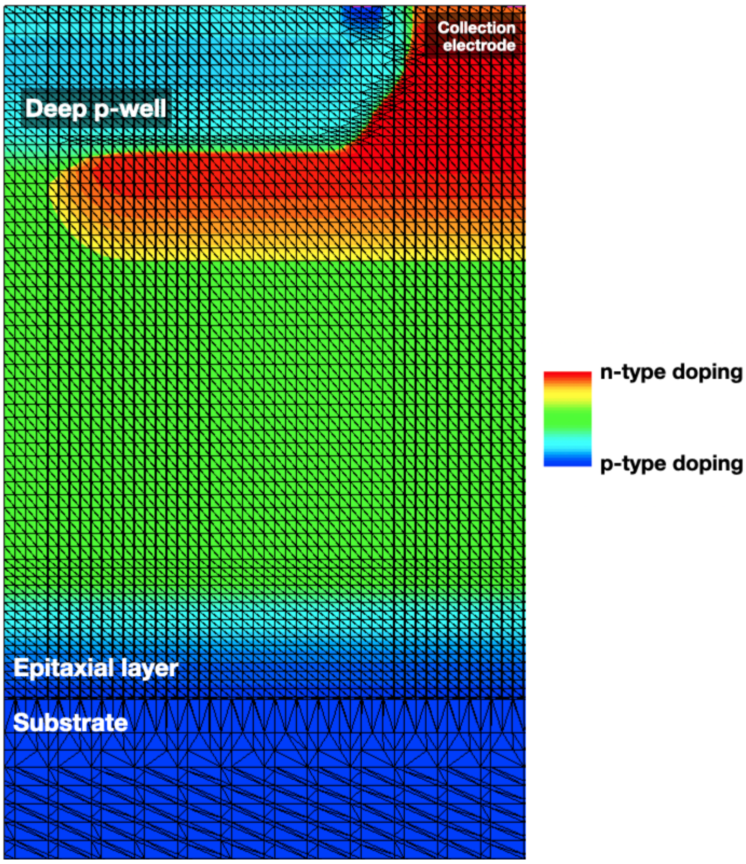

Figure 5.3: Cross section of half a pixel cell in TCAD. Here, a finer meshing is used for the epitaxial layer, and a coarser one for the substrate. Simulation not based on the actual doping profiles.

An example of both the doping profile and the meshing is shown in Figure 5.3. The simulation depicted is not based on the actual doping profiles, but it was inserted for illustrative purposes. Notably, the epitaxial layer (up to 10 µm of depth) presents a finer mesh compared to the substrate.

5.2.3 Sentaurus Device simulation

Once the geometry, doping concentration and mesh have been defined, the SDevice is used to define the physical parameters (such as material and temperature) and models the simulator should include in the differential equations.

For all the simulations performed for this study only silicon material at room temperature was considered.

The resulting electric field is computed starting from the doping profiles via the Poisson's equation:

$$\nabla E = \frac{\rho}{\epsilon} = \frac{q}{\epsilon}(-N_A + N_D) \tag{5.1}$$

Where E is the electric field, ρ is the charge density, ϵ is the permittivity, q is the elemental charge, and N_A and N_D are the acceptor and donor doping concentrations.

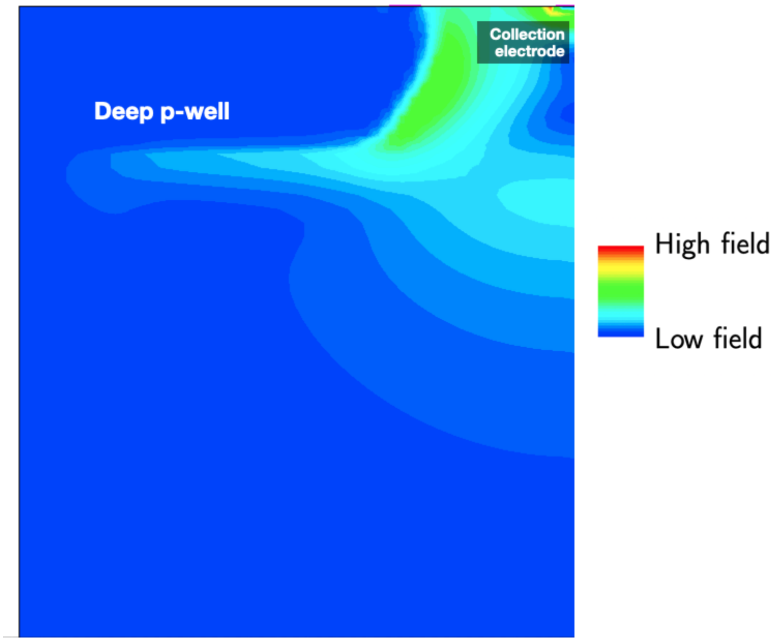

Figure 5.4: Cross section of a typical electric field (absolute value) of one pixel cell along the epitaxial layer for a modified with gap APTS with a 15 µm pixel pitch. Simulation not based on the actual doping profiles.

A typical electric field of one pixel cell along the epitaxial layer is shown in Figure 5.4. Similarly to Figure 5.3, the simulation is based on simple doping profiles that do not correspond to the real profiles.

The electric field in the substrate is not shown as this whole area is characterized by a very low field value.

SDevice also incorporates the modeling of carrier transport mechanisms, specifically addressing the dependence of carrier mobility and lifetime on electric fields and doping profiles. Regarding carrier mobility, a hybrid approach is employed, combining the Canali model (outlined in Section 3.1.3) and the Masetti model [121] (more applicable in low-field conditions). Additionally, the carrier lifetime and recombination effect are modeled using the SRH model, as detailed in Section 3.1.3.

5.3 Charge collection simulation - Garfield++

Garfield++ is an advanced, open-source toolkit designed to simulate ionization and signal formation in particle detectors, particularly gas and silicon detectors. Originally developed in FORTRAN several decades ago as Garfield for modeling gas detectors, the framework was later rewritten and expanded in C++. By building on the original code, Garfield++ takes advantage of similar numerical methods applicable to both gas and silicon detectors, allowing much of the foundational code to be reused across detector types [122]. The toolkit's flexibility and ongoing community support make it a versatile resource, suitable for both current and future detector applications.

In the simulation process developed for this thesis, the objective is to model the charge collection and sharing dynamics across a matrix of detector pixels under specific electric field conditions. The electric field for a single pixel is initially generated using TCAD and is then imported in Garfield++, where it is repeated to form a 5×5 pixel matrix, shown in Figure 5.5. This allows for realistic modeling of charge-sharing effects between adjacent pixels.

Once the electric field configuration is established, Garfield++ is used to simulate the charge collection process. In this step, electrons are systematically injected into the central pixel across various coordinates along its surface, as well as at multiple depths within the pixel. The scanning over injection coordinates is performed with a step size of 0.5 µm ranging over half the pitch size in both directions (red square in Figure 5.5), while depth steps are taken every 0.9 µm for the total vertical extension of the sensor. The selection of these step sizes is the result of a compromise between minimizing the simulation time and maintaining a high level of precision. Similarly,

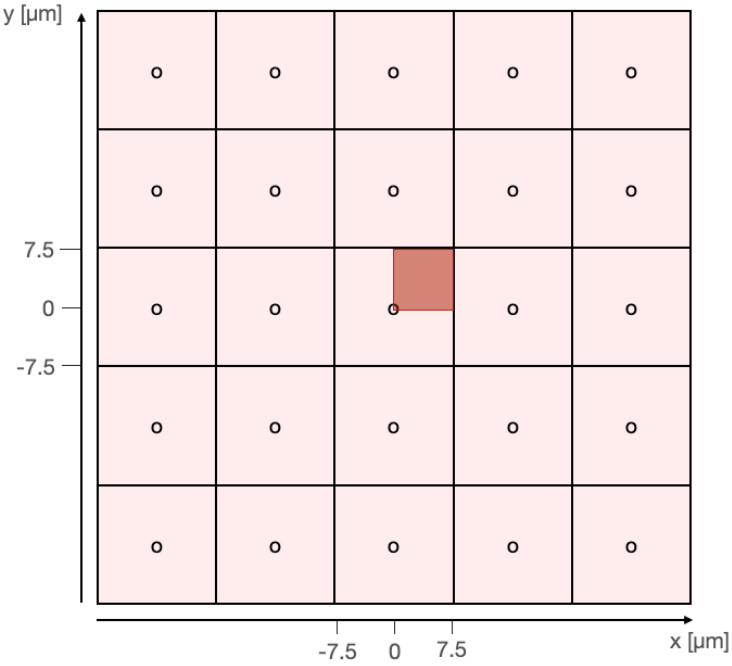

Figure 5.5: Sketch of a simulated matrix of 5 × 5 pixels with a pitch of 15 µm. In red the range of the scanned injection coordinates is highlighted.

the range of the injection coordinates was limited to only one quarter of the pixel to minimize the computational resources. Thanks to the electrode-centered symmetry the results obtained for this quarter can be mirrored in both directions to describe the whole pixel region.

This scan of different injection points captures the variability in possible charge deposition locations and depths, thereby simulating the full spectrum of realistic interaction scenarios within the detector.

The charge transport dynamics within each pixel are then modeled through a Monte Carlo-based integration in Garfield++, better described in Section 5.3.1.

Finally, the results of the simulation are consolidated into charge collection maps. Each map, produced for a specific (x, y) coordinate, record the number of electrons collected at each pixel within the matrix, providing a comprehensive view of charge sharing among pixels.

For any given injection coordinates (x, y), the charge collection map is defined as:

$$\text{Map}_{(x,y)} = \begin{bmatrix} Q_0(x,y,z_0) & Q_1(x,y,z_0) & \cdots & Q_{24}(x,y,z_0) \\ Q_0(x,y,z_1) & Q_1(x,y,z_1) & \cdots & Q_{24}(x,y,z_1) \\ \vdots & \vdots & & \vdots \\ Q_0(x,y,z_n) & Q_1(x,y,z_n) & \cdots & Q_{24}(x,y,z_n) \end{bmatrix},$$

where:

$Q_k(x,y,z_i)$ represents the charge collected by pixel k, $k = 5p+q$, $p,q \in \{0,1,2,3,4\}$.

The depth values z_i are given by:

$$z_i = 0 - i \cdot \Delta z, \quad \Delta z = 0.9\ \mu m, \quad i \in \{0,1,\ldots,n\}, \quad n = \frac{49.5}{\Delta z} = 55.$$

Thus, the full map is expressed as:

$$\text{Map}_{(x,y)} = [Q_k(x,y,z_i)]_{\substack{i\in\{0,1,\ldots,n\},\\ k\in\{0,1,\ldots,24\}}}.$$

Here:

- $k = 5p + q$ maps the 2D pixel indices $[p,q]$ in the 5x5 matrix to a single linear index k,
- z_i represents the depth, starting from $z_0 = 0$ µm and decreasing by $\Delta z = 0.9$ µm until $z_n = -49.5$ µm.

By detailing electron collection at specific positions within each pixel, these maps serve as a basis for modeling the response of the detector to diverse interactions with different particles.

5.3.1 Charge transport mechanism

The charge transport mechanism is simulated using the Monte Carlo integration of Garfield++, called *AvalancheMC* [123]. To calculate each step of the carrier migration, the AvalancheMC incorporates both drift and diffusion transport mechanisms (see Section 3.1.3). The algorithm follows the following steps:

- A step of length $\Delta s = v_d \Delta t$ in the direction of the drift velocity at the local electric field is calculated. For this purpose, the user can fix either a distance step Δs or a time step Δt and calculate the other (for this study the distance step was fixed at Δs of 0.5 µm)

- A random diffusion step is sampled from three uncorrelated Gaussian distributions with standard deviation $\sigma_L = D_L\sqrt{\Delta s}$ for the component parallel to the drift velocity and standard deviation $\sigma_T = D_T\sqrt{\Delta s}$ for the two transverse components, where D_L and D_T are the longitudinal and transverse diffusion coefficients, respectively
- The two steps are added vectorially and the location is updated

If the electric field or drift speed is zero, the algorithm switches to diffusion-only steps based on the low-field mobility.

After each step, Garfield++ will check if the carrier has reached the electrode and if it is outside the simulation boundary. If the carrier has neither reached the electrode nor the sensor boundary, the next step will be calculated. If the carrier has reached the electrode or the boundary, it checks if there are carriers left to be propagated.

5.4 Simulation of the chip response to X-rays

Once the charge collection maps are produced they are used as input to a python code specifically developed for this purpose that models the response of the sensor to X-rays. These maps provide the information on how charge spreads within the sensor for several possible injection coordinates. Interpolating these data allows to calculate the charge spread for any given X-ray interaction point within the sensor's structure.

The different X-ray energies of ^{55}Fe are simulated separately, with distinct photon counts and attenuation lengths (28.8 and 38 µm respectively for the 5.9 keV and 6.5 keV X-rays, as obtained from [124]). The results for different energies are then combined to reflect the total sensor response. To obtain the Si-escape peak the same procedure is used, with an effective attenuation length calculated with [124] starting from the energy associated to the Si-escape peak [1].

For each simulated X-ray:

- A random depth within the sensor is selected based on an exponential attenuation model, which reflects the probability of interaction at different depths.
- Random positions are chosen within the pixel area. This represents the random arrival location of the X-ray photon on the sensor surface, assuming a uniform distribution.

---

[1] It is important to note that applying this approach to the Si-escape peak is only an approximation. The underlying physical mechanism responsible for the generation of the Si-escape peak differs fundamentally from that governing the Mn-K_α and Mn-K_β peaks, as explained in Section 3.3.2.

- The charge resulting from the X-ray is extracted from a Gaussian distribution with a standard deviation given by the charge noise, a parameter used to account for statistical fluctuations and modeled using the Fano factor.

- With the random depth and lateral coordinates estabilished, the simulation retrieves the charge distribution from the precomputed charge maps. From this, it calculates how the generated charge carriers (electrons) disperse among the neighboring pixels, creating a cluster.

- To account for the electronic noise inherent in real-world measurements threshold noise and readout noise are added. These two parameters were tuned based on an optimization process aimed at aligning the simulated results with measured data. This optimization resulted in a threshold noise of 5 electrons and a readout noise of 35 electrons.

- Finally, a threshold is applied to the final charge collected from each pixel. This value is given as an input parameter of the simulation and it is in accordance with the one applied to the measured data.

5.5 Results

As a baseline to estabilish the compatibility between simulations and data, a modified with gap APTS with a pixel pitch of 15 µm and at a back-bias of 1.2 V was chosen.

The first results are shown in Figure 5.6, where the different cluster sizes are depicted as separate distributions. On the left is the measured spectrum, while on the right is the simulated one.

While the main peaks already show a good compatibility, in the lower charge region (below 800 electrons) a different contribution becomes visible in the simulated distribution.

For a better visualisation the measured cluster size distributions (continuous lines) can also be plotted separately and directly compared with the simulated one (dotted lines), as shown in Figure 5.7.

The results reveal a notable discrepancy in the lower charge region, which is significantly influenced by carriers originating from the substrate. This suggests a potential misrepresentation of the substrate within the simulation model. This discrepancy underscores the importance of accurately modeling the recombination effect, as it plays a crucial role in determining the substrate's impact on charge collection. To address this, an in-depth analysis of the carrier lifetime modeling approach implemented in the

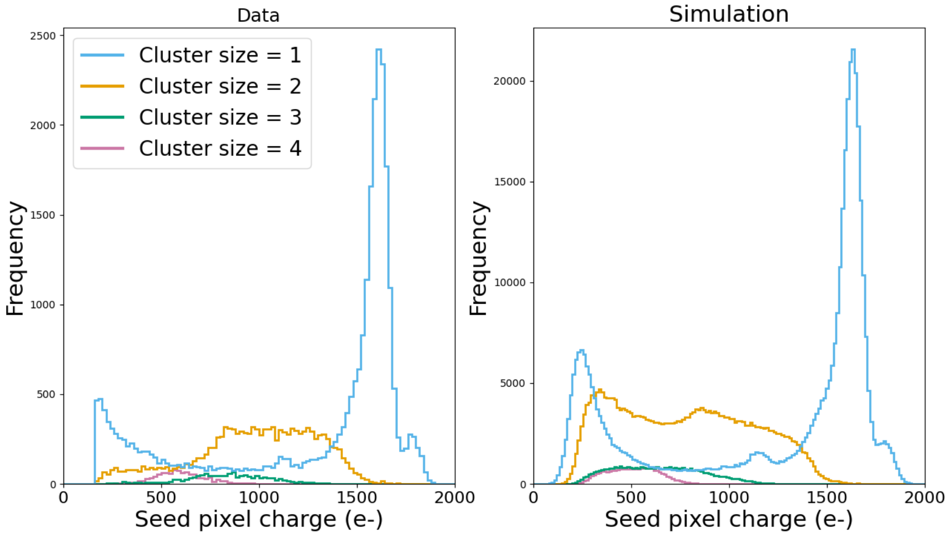

Figure 5.6: Comparison between simulated and actual ^{55}Fe spectrum for different cluster sizes. Simulations carried out without a recombination model in Garfield++. These data refer to a modified with gap APTS with a pixel pitch of 15 µm and at a back-bias of 1.2 V.

simulation was conducted. A comprehensive discussion of this analysis is presented in the following section.

Another comparison that is used to validate the simulation accuracy is the cluster size distribution, shown in Figure 5.8.

It is evident from this plot that there is a discrepancy between simulation and data in terms of charge sharing, specifically in the ratio between events of cluster size equal to 1 and 2.

5.5.1 Carrier lifetime investigation

At the onset of this simulation study, Garfield++ did not yet provide a proper implementation of the recombination effect within the sensor, an effect critical to accurately modeling the charge carrier transport in monolithic sensors. As discussed in Section 3.1.3, this recombination effect is particularly significant within the substrate region, where charge carriers tend to have a shorter lifetime due to increased recombination rates.

At the end of this section a proper implementation of the recombination effect will

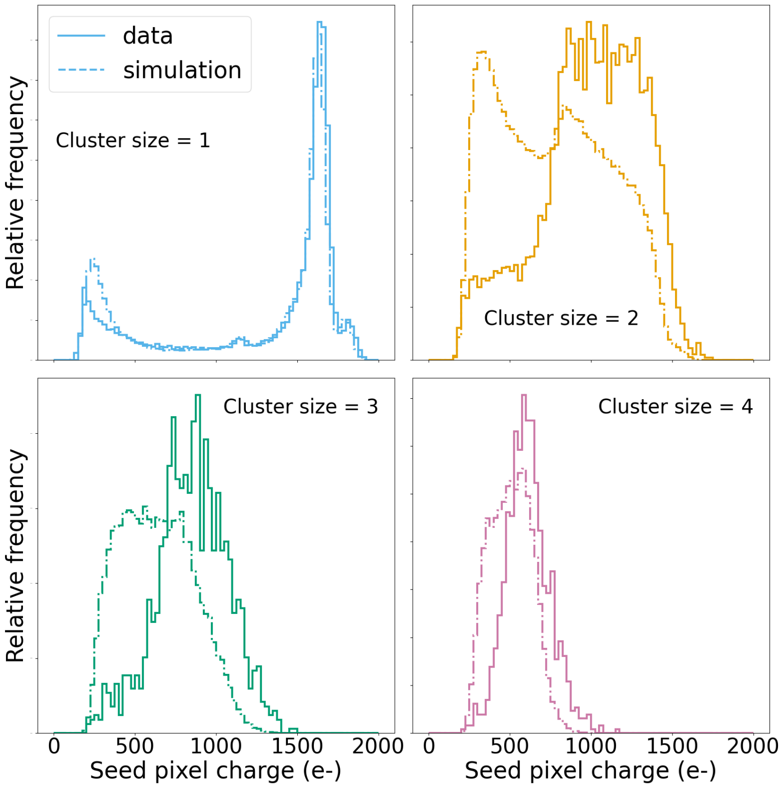

Figure 5.7: Comparison between simulated and measured ^{55}Fe spectra for different cluster sizes. Each sub-plot is normalised individually. Simulations carried out without a recombination model in Garfield++. These data refer to a modified with gap APTS with a pixel pitch of 15 µm and at a back-bias of 1.2 V.

be presented. However, to illustrate the importance of the including the recombination effect, the results obtained without it are presented first.

Lifetime approximation

Initially, to approximate the recombination effect within the limitations of the current Garfield++ model, a practical workaround was employed: the simulation's time window was reduced. By limiting the time window, carriers that require a longer period to reach the collection electrodes are excluded from the simulation results. Importantly,

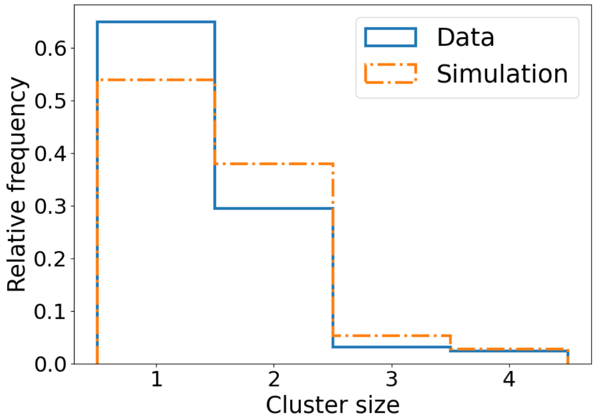

Figure 5.8: Comparison between simulated and measured cluster size distributions. Simulations carried out without a recombination model in Garfield++. These data refer to a modified with gap APTS with a pixel pitch of 15 µm and at a back-bias of 1.2 V.

only carriers originating from the substrate exhibit such prolonged migration times, as in this region there is practically no electric field. While carriers in the epitaxial layer are collected much more rapidly.

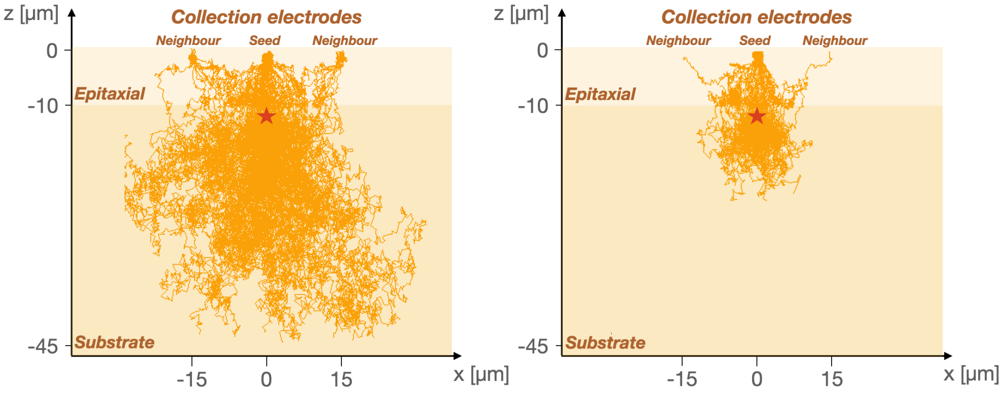

Figure 5.9: Migration lines (drift+diffusion) of the collected electrons for the seed pixel and the two neighbouring pixels along the x-axis. Data obtained injecting 100 electrons at a depth of 12 µm in the seed pixel. On the left without any time window and on the right with a time window of 3 ns applied to the simulation. The red star indicates the injection point.

An example of how applying this time window affect the collected charge is shown in Figure 5.9, where the drift lines of all the collected electrons are shown along the sensor depth. To obtain these data, 100 electrons were deposited at a depth of 12 µm, thus in the region of the substrate closer to the epitaxial layer.

On the left no time window is applied, thus there is no accounting for the recombination effect, while on the right a time window of 3 ns is applied. This specific value was selected as it produces the best match between the simulated results and the observed ^{55}Fe spectra and corresponding cluster size distributions. The results of this comparisons are shown respectively in Figure 5.10 and 5.11.

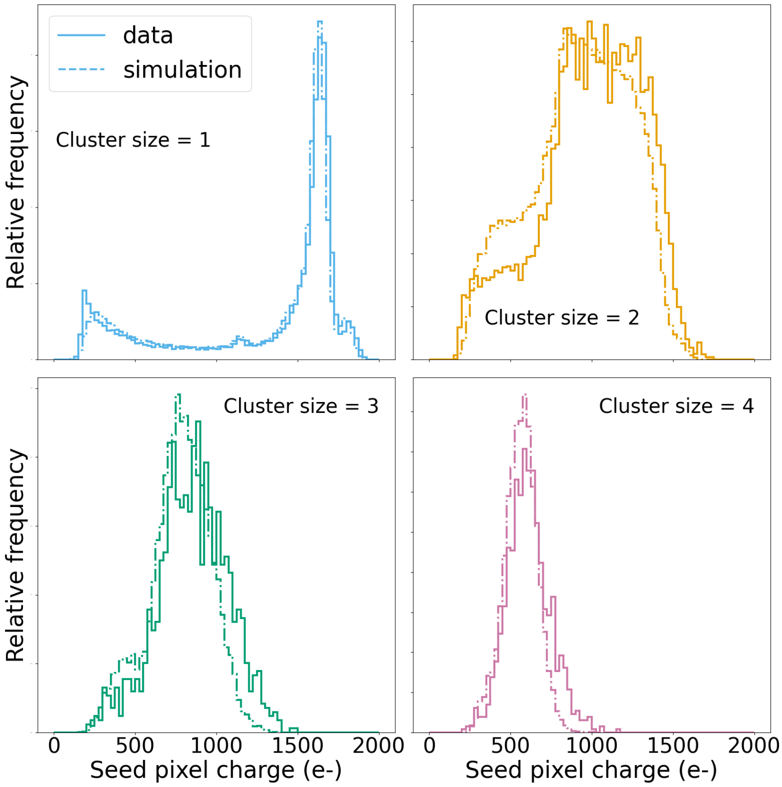

Figure 5.10: Comparison between simulated and measured ^{55}Fe spectra for different cluster sizes, with the application of a 3 ns time window to the simulation. These data refer to a modified with gap APTS with a pixel pitch of 15 µm and at a back-bias of 1.2 V.

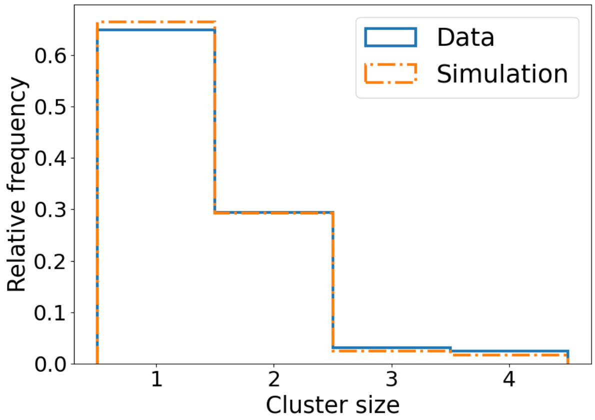

Figure 5.11: Comparison between simulated and measured cluster size distributions, with the application of a 3 ns time window to the simulation. These data refer to a modified with gap APTS with a pixel pitch of 15 µm and at a back-bias of 1.2 V.

Comparing these plots to Figure 5.7 and 5.8, it is evident that this approximation results in a great improvement in terms of compatibility with the data.

This method, while not an exact replication of the recombination effect, serves as a reasonable approximation. It effectively emulates the reduced carrier lifetime in the substrate by inherently filtering out slower-moving carriers, which would otherwise recombine before reaching the electrodes. Thus, the approach provides a simplified yet effective way to account for substrate-specific recombination dynamics, even in the absence of a fully implemented recombination model in Garfield++. Unfortunately this method remains reasonable only in sensors where the carrier migration inside the epitaxial layer is drift-driven.

To better illustrate why the lifetime approximation can become ineffective in some cases, the simulation process was repeated for the different implant geometries of the APTS sensor (see Figure 4.21). For each of these variants the geometry parameters were modified according to the corresponding low-dose implant specifications and the electric field was reproduced. The results of these comparisons are shown in Figure 5.12.

The comparison shows that the simulated and measured spectra are compatible for all the different implant geometries. The only visible discrepancy is in the standard process simulation, in the low-charge region associated with the charge sharing. This can be attributed to the time window application. While this approach works well as an approximation in scenarios where charge migration is dominated by drift mechanisms,

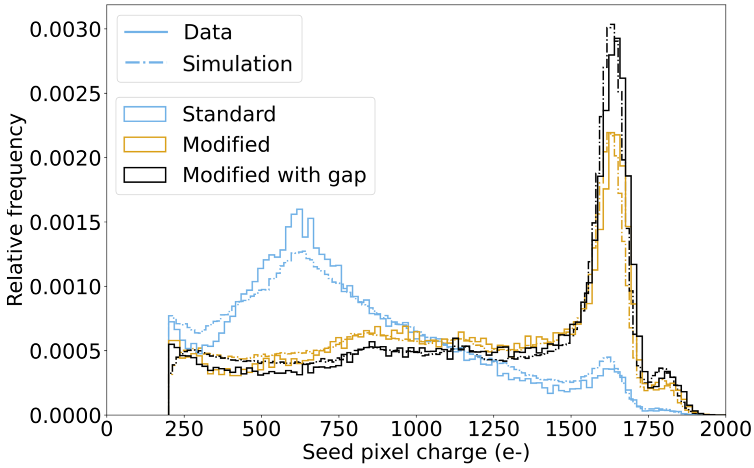

Figure 5.12: Comparison between simulated and measured ^{55}Fe spectra for different implant geoemtries. These data refer to APTS pixel pitch of 15 µm and at a back-bias of 1.2 V.

it is less accurate in the standard process where diffusion also plays a significant role.

In diffusion-dominated scenarios, charges can take longer to migrate due to their random spread across the diffusion region. By imposing a fixed time window, the simulation inadvertently excludes some events that are not truly lost but instead require additional time to complete their migration. Consequently, this time window truncation leads to the observed mismatch in the low-charge region of the standard process distribution.

Recombination modelling in Garfield++

To overcome this limitation, a robust implementation of the recombination effect has been integrated into the Garfield++ framework.

TCAD simulations provide detailed spatial distributions of material properties, including the carrier lifetime information (modeled as explained in Section 5.2.3). These distributions reflect variations in doping concentration and electric fields. By importing the outputs of TCAD simulations into the Garfield++ framework, it becomes possible to accurately simulate recombination effects with high precision. The same method of importing TCAD outputs was applied to the carrier mobility information.

This upgraded version of Garfield++ incorporates recombination probability maps derived from TCAD simulations, which are imported into Garfield++ as spatially dependent tables. During each transport step, the framework evaluates the recombination probability based on the carrier's spatial position.

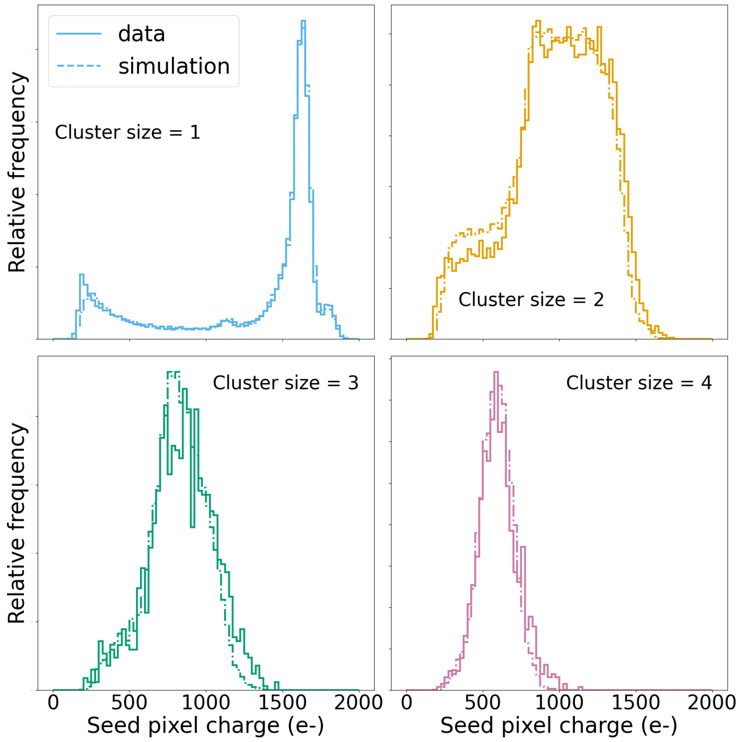

Figure 5.13: Comparison between simulated and measured ^{55}Fe spectra for different cluster sizes. Simulations carried out with the new recombination modelling of Garfield++. These data refer to a modified with gap APTS with a pixel pitch of 15 µm and at a back-bias of 1.2 V.

The results of this implementation are presented in Figure 5.13 and Figure 5.14, for charge sharing and cluster size distributions, respectively. These plots demonstrate a much better agreement between simulation and experimental data, with only minor discrepancies observed.

For the validation of this new framework the results were compared not only with the experimental data but also with other simulations carried out using Allpix2, a well-established software framework for silicon detectors [125]. The simulation structure remained the same explained in Section 5.1, but the charge collected maps were produced in Allpix2 instead of Garfield++. The comparisons revealed a strong agreement across different tools, further confirming the accuracy and reliability of the implementation.

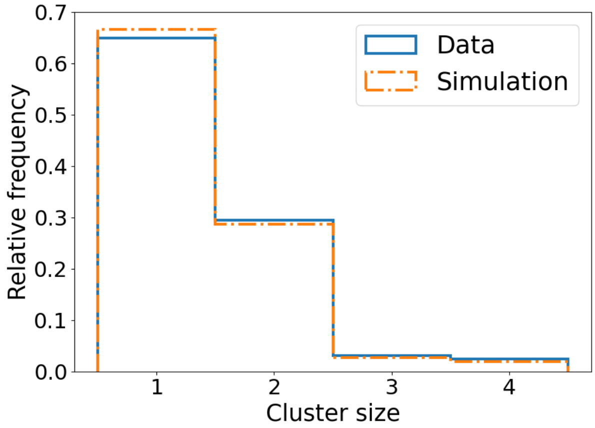

Figure 5.14: Comparison between simulated and measured cluster size distributions. Simulations carried out with the new recombination modelling of Garfield++. These data refer to APTS pixel pitch of 15 µm and at a back-bias of 1.2 V.

The plots of this comparison are shown in Appendix C.

5.5.2 Variants comparison

The validity of the recombination implementation is further supported by the results obtained for the standard process, as depicted in Figure 5.15.

When compared to Figure 5.12, which employs the time window approximation rather than utilizing carrier lifetime information, the simulation of the standard process demonstrates a significantly improved alignment with the experimental data. This improvement can be attributed to a more accurate representation of regions where diffusion dominates over drift, ensuring a closer match to the physical behavior observed in the experimental setup.

Additionally, different pixel pitches of the modified with gap process were simulated and compared to the experimental data. The results are reported in Figure 5.16.

The distributions exhibit a trend consistent with those observed in Figure 4.23(c), demonstrating a similar overall shape across different pixel pitches, with a very slight improvement in the charge collection performance for larger pixel pitches.

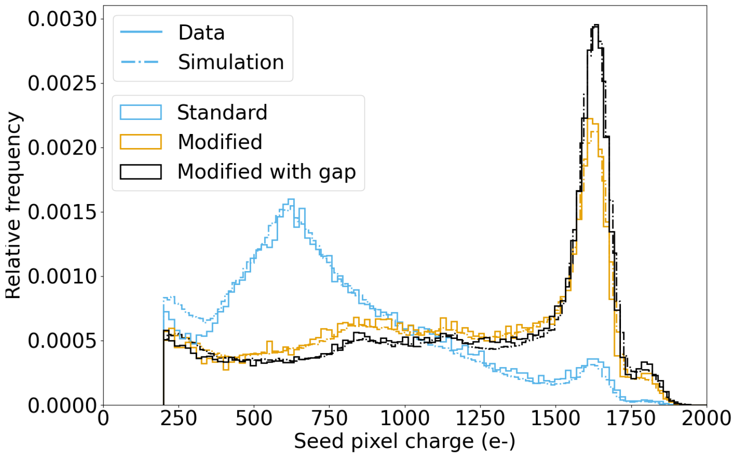

Figure 5.15: Comparison between simulated and measured ^{55}Fe spectra for different implant geoemtries. Simulations carried out with the new recombination modelling of Garfield++. These data refer to APTS pixel pitch of 15 µm and at a back-bias of 1.2 V.

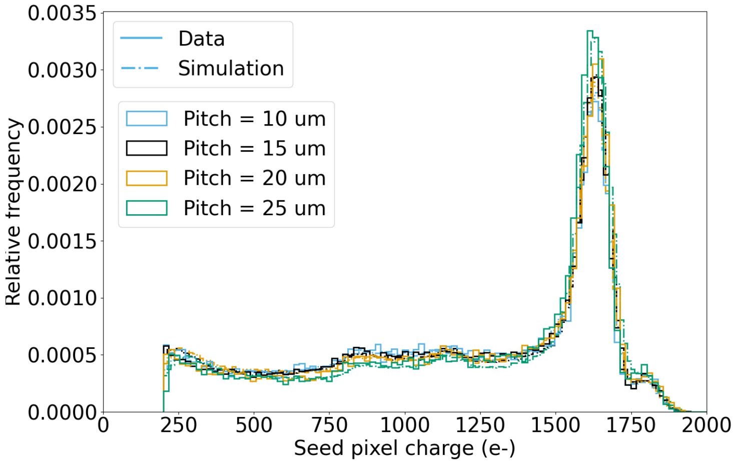

Figure 5.16: Comparison between simulated and measured ^{55}Fe spectra for different pixel pitches. Simulations carried out with the new recombination modelling of Garfield++. These data refer to APTS pixel pitch of 15 µm and at a back-bias of 1.2 V.

5.6 Summary

The simulation studies conducted on the APTS chips have led to significant advancements in the understanding and modeling of their performance. By integrating TCAD simulations for electric field modeling, Garfield++ for charge transport simulation, and a Python-based framework for X-ray interaction and chip response, a comprehensive simulation workflow was established.

The comparison between simulated and experimental spectra revealed a high level of agreement, validating the overall framework. The observed discrepancy in the low-charge region highlighted the importance of accurately modeling substrate effects, particularly recombination phenomena. The initial lifetime approximation provided a temporary solution but proved insufficient for scenarios with notable diffusion transport. The direct implementation of recombination effects in the Garfield++ source code addressed these challenges, significantly improving the agreement between simulation and experimental results across various conditions.

This simulation framework is now versatile and capable of accommodating multiple chip variants and conditions, including ongoing developments to model irradiation effects. These advancements not only provide valuable insights into the behavior of APTS chips but also establish a robust foundation for future studies and optimizations. As a result, this work paves the way for the accurate characterization and development of high-performance sensors for ITS3 and other applications.

Chapter 6

Outlook & Conclusions

6.1 Outlook

The studies presented in this thesis have demonstrated the significant potential of the 65nm technology to meet the stringent requirements of the ITS3 upgrade for the ALICE experiment. This achievement marks a critical advancement in the ITS3 development, but it also provides a solid foundation for a wide range of applications beyond the immediate scope of this project.

Building on these findings, the development of the ITS3 upgrade is now entering a pivotal phase, with an emphasis on wafer-scale prototypes.

As anticipated in Section 2.1.3, a key ingredient of this phase is the adoption of stitching technology, which enables the production of monolithic sensors spanning the entire diameter of a silicon wafer. This innovation eliminates the need for segmentation and interconnects, fundamental limitations of traditional designs. Consequently, it allows the creation of ultra-thin, wafer-scale sensors that can be bent to conform to the ITS3's truly cylindrical geometry around the beam pipe.

In order to validate the stitching technology for this application, two prototypes were designed and produced in Engineering Run 1 (ER1): the MOnolithic Stitched Sensor (MOSS) and the MOnolithic Stitched Timing (MOST), developed using the 65nm CMOS imaging process. A photograph of an ER1 wafer containing both MOSS and MOST prototypes is shown in Figure 6.1.

Each prototype comprises 10 Repeated Sensor Units (RSUs) stitched together, resulting in a total structure length of approximately 260 mm. The MOSS prototype features pixel pitches of 18 µm and 22.5 µm, hosting a total of 6.72 million pixels, while MOST comprises 0.9 million pixels with an 18 µm pitch.

The characterization of these devices necessitates specialized tools and procedures for both handling and testing. In particular, MOSS is undergoing a comprehensive functional testing campaign, which includes laboratory evaluations and beam test demon-

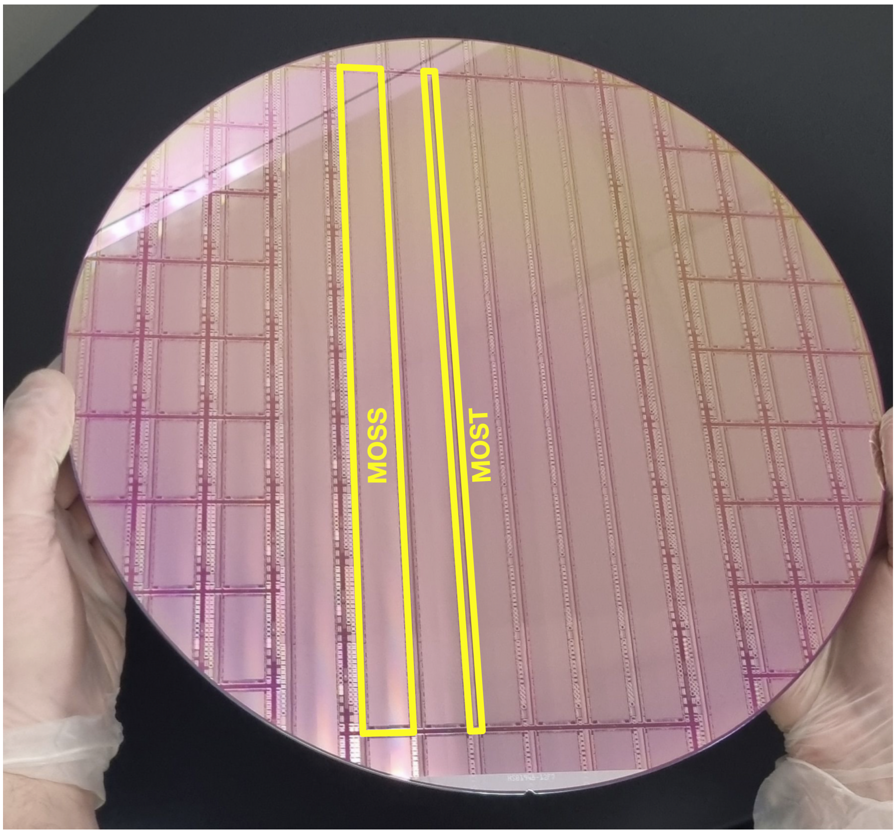

Figure 6.1: A 300 mm ER1 wafer, containing six MOSS and MOST stitched sensors (indicated), as well as a number of small prototype chips. Taken from [42].

strations. First results are highly promising, indicating robust yield and good detection performance [42].

The R&D provided key knowledge in the design, handling and testing of thin, highly integrated and segmented, wafer-scale structures and provides crucial input for the final sensor implementation.

The next major milestone in the ITS3 roadmap is the development of MOSAIX, a full-feature wafer-scale MAPS sensor that leverages stitching technology and the 65nm CMOS imaging process. As the second-generation stitched sensor, MOSAIX represents a comprehensive, fully functional prototype, incorporating the lessons learned from the MLR1 and ER1 submissions. The MOSAIX sensor will feature approximately 10.73 million pixels per segment, with a pixel pitch of 20.8 µm × 22.8 µm.

This project integrates full staves and modules on a single wafer, with each segment composed of 144 identical tiles. Each tile operates as an independent unit, enhancing manufacturability and enabling the deactivation of defective tiles to maximize overall yield. The wafer stitching plan of the MOSAIX is shown in Figure 6.2.

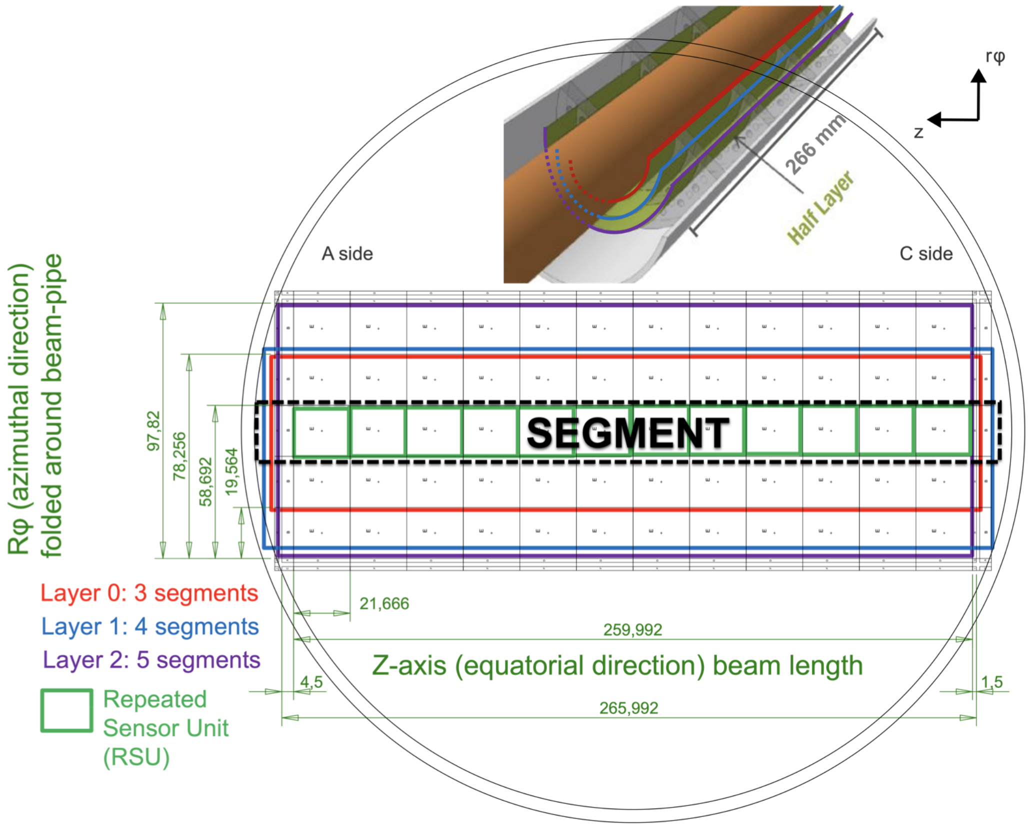

Figure 6.2: CMOS wafer stitching plan and dimensions of the ITS3 sensors in mm. The actual chip design dimensions are shown with a precision of 1 µm. The dashed black rectangle indicates one of the five segments. The red rectangle shows one of the 3 possible groupings of three segments to make one of the sensors for layer 0. The blue rectangle shows one of the 2 possible groupings of four segments to make one of the sensors for layer 1. The purple rectangle shows the grouping of five segments to make layer 2. The beam axis direction (z) and the azimuthal direction (rϕ) are shown. The A side and C side labels indicate the ALICE detector sides. The illustration in the top of the figure shows the placement of the 3 lower bottom sensors bent around the beam pipe illustrating that the detector consists of 6 silicon sensors only. Taken from [42].

The design phase of MOSAIX is nearing completion, with verification processes actively underway. This prototype is expected to undergo rigorous testing in the coming years to ensure its reliability and performance.

All the advancements that the ITS3 R&D has achieved (such as 65 nm technology validation, wafer-scale sensor development, bending procedures), will also set the basis for future upgrades of ALICE, such as the vertex detector of ALICE 3 (a completely new apparatus planned for LHC Runs 5 and 6 [126]). This novel detector is based on an evolution of the ITS3 concept aiming at a track pointing resolution of better than 10 µm for tranverse momenta above 200 MeV/c through the integration of the tracking layers in a retractable structure inside the beam pipe [127]. In Figure 6.3 the pointing resolution progression with the future ALICE upgrades is shown.

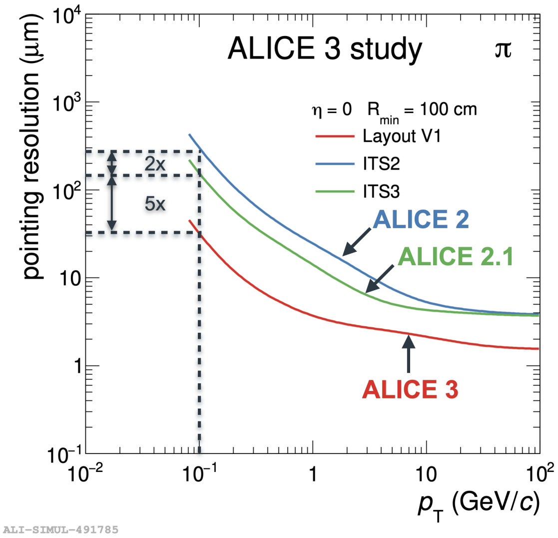

Figure 6.3: Pointing resolution progression with the future ALICE upgrades. Taken from [128].

The layout of the ALICE 3 tracking system is depicted in Figure 6.4, comprising of Vertex Detector, Middle layer and Outer tracker.

The main challenge of the ALICE 3 vertex detector will be the radiation tolerance, of approximately 300 Mrad + 10^{16} 1 MeV $\mathrm{n_{eq}}$ cm^{-2}. However, considering that ITS3 prototypes already demonstrated a good performance for a radiation dose up to 10^{15} 1 MeV $\mathrm{n_{eq}}$ cm^{-2} at room temperature, an improvement on the forthcoming designs seems achievable. This underscores the critical value of this thesis work for ALICE 3. The extensive characterization on the 65 nm CMOS prototypes provide a solid foundation for future characterization and optimization efforts. These contributions are essential to

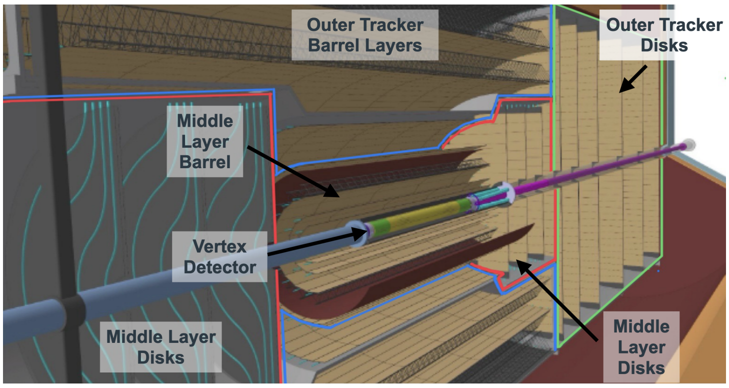

Figure 6.4: Layout of the ALICE 3 tracking system. Taken from [128].

meet the stringent requirements of the ALICE 3 vertex detector.

Looking even further in the future, the 65 nm technology will play a crucial role in the development of MAPS sensors for experiments beyond ALICE. This technology is considered a favourite candidate for future Higgs factories like the Future Circular Collider (FCC-ee) [129]. The ITS3, ALICE 3 and FCC-ee vertex detectors share key requirements, such as low material budget and enhanced pointing resolution [130, 131]. For these reasons, ALICE upgrades can provide a valuable platform for prototyping and refining MAPS technology, serving as a stepping stone toward future detectors.

Another important contribution of this thesis work to the field of MAPS is the developed simulation framework, which will serve as a powerful tool for the design and optimization of MAPS sensors. While it is tailored to the specific needs of the APTS chip, its design extends far beyond this application. The framework's adaptability allows to simulate a wide range of experimental setups, making it an invaluable resource for testing and optimizing diverse configurations. Furthermore, it can be adapted to simulate the response of various monolithic prototypes, within and outside the scope of ITS3. In particular, simulating the final sensor of ITS3 and implementing its response to the ALICE O^2 simulation framework will enable more accurate simulations of the detector performance.

6.2 Conclusions

In this thesis the performance of the Analogue Pixel Test Structure (APTS) chip, developed in the MLR1 submission as part of the ITS3 upgrade of the ALICE experiment, was extensively studied. This characterization successfully validated the Tower Partners Semiconductor Co (TPSCo) CMOS 65 nm ISC process for its intended application by assessing key performance metrics such as charge collection efficiency, detection efficiency, and radiation hardness. Additionally, the study identified the most suitable variant of APTS from the several produced, differing in terms of: implant geometry design, doping and pixel pitch. Each variants was tested at different reverse substrate bias and levels of NIEL and TID irradiation.

The initial phase of this work involved extensive functional tests conducted in the laboratory to ensure the proper operation of the chip and to determine an optimal operational point. Using an ^{55}Fe source, a precise energy calibration was performed and a campaign of measurements was conducted to study the charge collection performance of the various APTS variants. The measurements demonstrated that the modified with gap process, designed to optimize the charge collection efficiency, achieved significantly superior performance compared to other variants.

Furthermore, the APTS variants were tested during several beam test campaigns, where the detection efficiency was evaluated. The results showed that the modified with gap variant reached a higher operational margin compared to the others. It also reached a detection efficiency higher than 99% across different substrate biases and pixel pitches, consistently exceeding the requirement for the ITS3 application. Larger pitches provide a slight improvement in operating margin but only up to moderate NIEL levels.

This characterization demonstrated that the APTS chip satisfies the radiation hardness requirements for ITS3: both TID (3 MGy) and NIEL (10^{13} 1 MeV neq cm^{-2}). Additionally, it performs robustly even under higher irradiation levels, highlighting the prototype's versatility and potential applicability beyond ITS3. Notably, these results were achieved at room temperature, suggesting that there is room for improvement at lower temperatures.

This comprehensive characterisation on the APTS chip played a pivotal role in the completion of the ITS3 Technical Design Report (TDR) [31].

Additionally, it laid a solid foundation for the development of subsequent ITS3 prototypes, such as the ER1 wafer-scale stitched prototypes and the full-feature MOSAIX prototype. The promising results from this study provide confidence in the scalability and applicability of the 65 nm technology for ITS3 and future detector systems.

In parallel with the experimental work, a detailed simulation framework was developed to model the APTS response to X-rays coming from the ^{55}Fe source. This framework integrated TCAD simulations for electric field modeling, Garfield++ for carrier transport and collection mechanisms simulations, and a custom Python-based simulation for X-rays interaction and sensor response. Modifications were made to the Garfield++ source code to properly implement recombination effects in the sensor. These enhancements enabled excellent agreement between simulation results and experimental data, validating the reliability and accuracy of the simulation framework. This toolset is versatile and adaptable, capable of simulating not only different experimental setups but also other monolithic prototypes beyond APTS, facilitating the development of subsequent iterations for ITS3 and related applications.

Appendix A

Baseline autocorrelation

Several algorithms have been investigated to obtain the best evaluation of the baseline. The traditional way is calculating the average of the baseline over a given number of frames before the signal occurrence. However, this approach was not adopted because the baseline showed a short-range auto-correlation. Such a feature is illustrated in Figure A.1, where the chip output is measured in the region before the occurrence of the signal. More precisely, the chip output at the i^{th} sampling (where $i = 96$, therefore lower than the number of samples before the signal, that was set to 100) is reported as a function of the chip output at the $i^{th} - 1$ (left panel), $i^{th} - 4$ (middle panel) and $i^{th} - 20$ (right panel) samples.

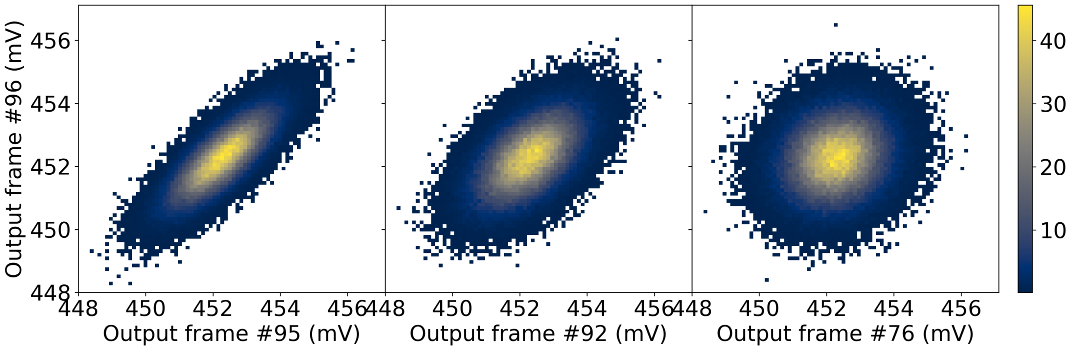

Figure A.1: Chip output voltage obtained at the 96^{th} frame, as a function of the chip output voltage at the 95^{th} (left), 92^{nd} (middle) and 76^{th} frame (right).

The auto-correlation is significant among close samples and decreases progressively considering more distant time/frames, becoming negligible already at 10 frames of distance. From this result one can conclude that at frames that are closer to the signal a more precise baseline evaluation is possible, while distant frames can lead to degradation in energy resolution.

However, it is also important to exclude the signal rise edge from the baseline evaluation. As a compromise between these two conditions, the baseline is estimated as the chip output in the 4^{th} sampling before the signal.

Appendix B

I_{reset} effect on the signal extraction

The I_{reset} parameter is directly linked to the accuracy of the signal extraction, and thus the energy resolution, bceuse of its impact on the return to baseline of the signal. Given that the algorithm used for the signal extraction is based on the search for the minimum of the waveform, at fixed sampling frequency a slower return to baseline results in a more precise evaluation.

In order to better quantify this effect, the minimum of the signal was evaluated with high precision using a delay between the trigger event and the starting point of the system sampling. Scanning over different values of this delay it is possible to overcome the limitation of the sampling frequency and obtain a finer measurement of the minimum.

This measurement was performed for different values of I_{reset} to better understand its effect on the energy resolution.

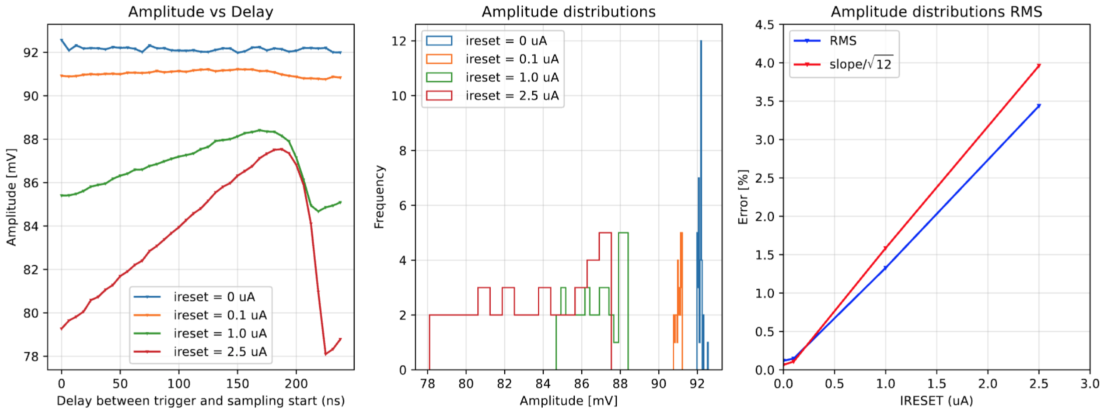

Figure B.1: Signal amplitude calculated scanning the delay between the trigger event and the starting point of the system sampling (left), its distribution (center) and the error associated with it (right) for different I_{reset}.

Figure B.1 shows the amplitude calculated with this finer method at different delays (left), its distribution (center) and the error associated with it (right) for different I_{reset}.

The error was estimated using two different methods: one is simply defined as the RMS of the amplitude distribution, the other is calculated as $slope/\sqrt{12}$ where *slope* is the slope of a linear fit performed on the region between 50 and 150 ns of the amplitude vs delay plot.

From this results it is clear that high values of I_{reset} result in a bigger error on the amplitude measurement, thus lower energy resolution.

Appendix C

Comparison between Garfield++ and Allpix2 simulations

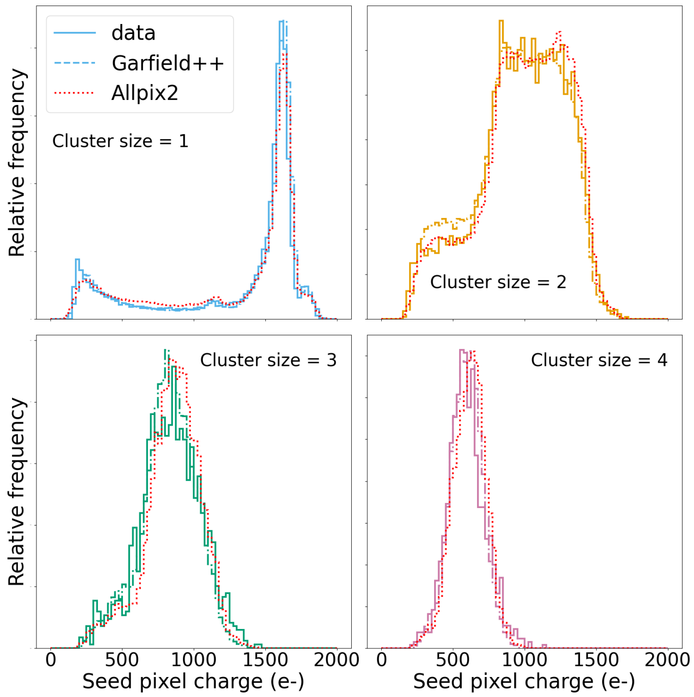

Figure C.1: Comparison between simulated and measured ^{55}Fe spectra for different cluster sizes. Simulations carried out both with the new recombination modelling of Garfield++ and with Allpix2. These data refer to a modified with gap APTS with a pixel pitch of 15 µm and at a back-bias of 1.2 V.

In Figures C.1 and C.2, the comparison between the data and the simulations obtained both in Garfield++ and in Allpix2 is shown.

The results are similar to those shown in Figures 5.13 and 5.14, but with the addition of the results obtained using the Allpix2 framework. An excellent agreement among the two different tools is observed, further confirming the accuracy and reliability of the implementation.

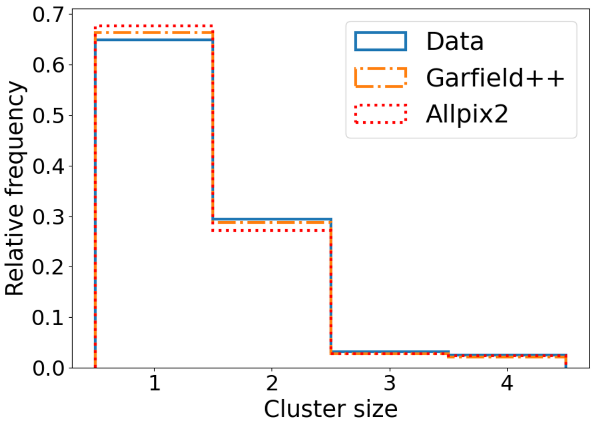

Figure C.2: Comparison between simulated and measured cluster size distributions. Simulations carried out both with the new recombination modelling of Garfield++ and with Allpix2. These data refer to APTS pixel pitch of 15 µm and at a back-bias of 1.2 V.

Bibliography

[1] Lyndon Evans and Philip Bryant. “LHC machine”. In: *Journal of instrumentation* 3.08 (2008), S08001 (cit. on pp. 1, 2).

[2] Ewa Lopienska. *The CERN accelerator complex, layout in 2022*. Tech. rep. 2022 (cit. on pp. 1, 2).

[3] ALICE collaboration. *First Lead Ion Collisions: LHC record energy*. URL: `https://home.cern/news/news/experiments/first-lead-ion-collisions-lhc-record-energy` (cit. on p. 1).

[4] Elena Shaposhnikova et al. *Lhc injectors upgrade (liu) project at cern*. Tech. rep. 2016 (cit. on p. 1).

[5] SM Alam et al. “The ATLAS experiment at the CERN large hadron collider”. In: *Journal of instrumentation* 3.8 (2008), S08003–S08003 (cit. on p. 2).

[6] Cms Collaboration et al. “The CMS experiment at the CERN LHC”. In: *Journal of instrumentation* 3.August 2008 (2008), pp. 1–334 (cit. on p. 2).

[7] Kenneth Aamodt et al. “The ALICE experiment at the CERN LHC”. In: *Journal of Instrumentation* 3.08 (2008), S08002 (cit. on p. 2).

[8] A Augusto Alves Jr et al. “The LHCb detector at the LHC”. In: *Journal of instrumentation* 3.08 (2008), S08005 (cit. on p. 2).

[9] Georges Aad et al. “Observation of a new particle in the search for the Standard Model Higgs boson with the ATLAS detector at the LHC”. In: *Physics Letters B* 716.1 (2012), pp. 1–29 (cit. on p. 2).

[10] Serguei Chatrchyan et al. “Observation of a new boson at a mass of 125 GeV with the CMS experiment at the LHC”. In: *Physics Letters B* 716.1 (2012), pp. 30–61 (cit. on p. 2).

[11] Johannes Erdmann et al. “Beyond Standard Model searches by ATLAS and CMS”. In: *Journal of Physics: Conference Series*. Vol. 1390. 1. IOP Publishing. 2019, p. 012041 (cit. on p. 2).

[12] Ana Lopes. *LHCb sheds light on two pieces of the matter-antimatter puzzle.* URL: `https://home.cern/news/news/physics/lhcb-sheds-light-two-pieces-matter-antimatter-puzzle` (cit. on p. 3).

[13] Kenneth Aamodt et al. “The ALICE experiment at the CERN LHC”. In: *Journal of Instrumentation* 3.08 (2008), S08002 (cit. on p. 3).

[14] Walter Greiner, Stefan Schramm, and Eckart Stein. *Quantum chromodynamics.* Springer Science & Business Media, 2013 (cit. on p. 3).

[15] Helen Caines. “The search for critical behavior and other features of the QCD phase diagram–current status and future prospects”. In: *Nuclear Physics A* 967 (2017), pp. 121–128 (cit. on pp. 3, 4).

[16] John W. Harris and Berndt Müller. “THE SEARCH FOR THE QUARK-GLUON PLASMA”. In: *Annual Review of Nuclear and Particle Science* 46.1 (Dec. 1996), pp. 71–107. ISSN: 1545-4134. DOI: `10.1146/annurev.nucl.46.1.71` (cit. on p. 3).

[17] Alexandre Deur, Stanley J. Brodsky, and Guy F. de Téramond. “The QCD running coupling”. In: *Progress in Particle and Nuclear Physics* 90 (2016), pp. 1–74. ISSN: 0146-6410. DOI: `https://doi.org/10.1016/j.ppnp.2016.04.003` (cit. on p. 3).

[18] John W Harris and Berndt Müller. “The search for the quark-gluon plasma”. In: *Annual Review of Nuclear and Particle Science* 46.1 (1996), pp. 71–107 (cit. on pp. 3, 4).

[19] Ulrich W Heinz. “Concepts of heavy-ion physics”. In: *arXiv preprint hep-ph/0407360* (2004) (cit. on p. 4).

[20] A Tawfik and Asmaa G Shalaby. “Balance Function in High-Energy Collisions”. In: *Advances in High Energy Physics* 2015.1 (2015), p. 186812 (cit. on p. 5).

[21] John W Harris and Berndt Müller. ““QGP Signatures” revisited”. In: *The European Physical Journal C* 84.3 (2024), p. 247 (cit. on p. 5).

[22] Jonghan Park. “Recent heavy-flavour measurements from ALICE”. In: *arXiv preprint arXiv:2407.13056* (2024) (cit. on p. 5).

[23] ALICE Collaboration. “Performance of the ALICE experiment at the CERN LHC”. In: *International Journal of Modern Physics A* 29.24 (2014), p. 1430044 (cit. on p. 6).

[24] ALICE collaboration et al. “ALICE upgrades during the LHC Long Shutdown 2”. In: *arXiv preprint arXiv:2302.01238* (2023) (cit. on pp. 6–8, 11).

[25] ALICE collaboration et al. “Alignment of the ALICE Inner Tracking System with cosmic-ray tracks”. In: *Journal of Instrumentation* 5.03 (2010), P03003 (cit. on p. 7).

[26] Johan Alme et al. “The ALICE TPC, a large 3-dimensional tracking device with fast readout for ultra-high multiplicity events”. In: *Nuclear Instruments and Methods in Physics Research Section A: Accelerators, Spectrometers, Detectors and Associated Equipment* 622.1 (2010), pp. 316–367 (cit. on p. 7).

[27] ALICE Collaboration et al. “The ALICE Transition Radiation Detector: construction, operation, and performance”. In: *Nuclear Instruments and Methods in Physics Research Section A: Accelerators, Spectrometers, Detectors and Associated Equipment* 881 (2018), pp. 88–127 (cit. on p. 7).

[28] A Akindinov et al. “Performance of the ALICE Time-Of-Flight detector at the LHC”. In: *The European Physical Journal Plus* 128 (2013), pp. 1–9 (cit. on p. 7).

[29] ALICE Collaboration, G Martinez-Garcia, W Riegler, et al. *Technical Design Report for the Muon Forward Tracker*. Tech. rep. tech. rep., CERN-LHCC-2015-001, ALICE-TDR-018, 2015. (cit. on p. 8).

[30] Jurgen Schukraft, ALICE Collaboration, et al. “First Results from the ALICE experiment at the LHC”. In: *Nuclear Physics A* 862 (2011), pp. 78–84 (cit. on p. 8).

[31] ALICE Collaboration. “Technical design report for the upgrade of the ALICE inner tracking system”. In: *Journal of Physics G: Nuclear and Particle Physics* 41.8 (2014) (cit. on pp. 8, 9, 22, 112).

[32] Giacomo Contin. “The STAR PXL detector”. In: *Journal of Instrumentation* 11.12 (2016), p. C12068 (cit. on p. 8).

[33] Helmuth Spieler. *Semiconductor detector systems*. Vol. 12. Oxford university press, 2005 (cit. on pp. 10, 35, 36).

[34] Kenzo Nakamura. “Review of particle physics”. In: *Journal of Physics G: Nuclear and Particle Physics* 37.7 A (2010) (cit. on p. 10).

[35] Tower Semiconductor. *TCMOS image sensor*. URL: `https://towersemi.com/technology/cmos_image_sensor/` (cit. on pp. 10, 17).

[36] M Mager, ALICE collaboration, et al. “ALPIDE, the Monolithic Active Pixel Sensor for the ALICE ITS upgrade”. In: *Nuclear Instruments and Methods in Physics Research Section A: Accelerators, Spectrometers, Detectors and Associated Equipment* 824 (2016), pp. 434–438 (cit. on p. 11).

[37] G. Aglieri Rinella, ALICE collaboration, et al. “The ALPIDE pixel sensor chip for the upgrade of the ALICE Inner Tracking System”. In: *Nuclear Instruments and Methods in Physics Research Section A: Accelerators, Spectrometers, Detectors and Associated Equipment* 845 (2017), pp. 583–587 (cit. on p. 11).

[38] W Snoeys. “CMOS monolithic active pixel sensors for high energy physics”. In: *Nuclear Instruments and Methods in Physics Research Section A: Accelerators, Spectrometers, Detectors and Associated Equipment* 765 (2014), pp. 167–171 (cit. on p. 11).

[39] Jamie Alexander Ballin et al. “Monolithic Active Pixel Sensors (MAPS) in a quadruple well technology for nearly 100% fill factor and full CMOS pixels”. In: *Sensors* 8.9 (2008), pp. 5336–5351 (cit. on p. 11).

[40] Cameron Thomas Dean. “The sPHENIX experiment at RHIC”. In: *PoS-Proceedings of Science* 390.LA-UR-20-30202 (2021) (cit. on p. 11).

[41] Luciano Musa. *Letter of Intent for an ALICE ITS Upgrade in LS3*. Tech. rep. 2019 (cit. on pp. 14, 20, 23, 24, 37).

[42] ALICE collaboration The. *Technical Design report for the ALICE Inner Tracking System 3 - ITS3 ; A bent wafer-scale monolithic pixel detector*. Tech. rep. Geneva: CERN, 2024 (cit. on pp. 14–16, 18–21, 108, 109).

[43] G Aglieri Rinella et al. “First demonstration of in-beam performance of bent Monolithic Active Pixel Sensors”. In: *arXiv preprint arXiv:2105.13000* (2021) (cit. on p. 15).

[44] ITS ALICE. “Expression of Interest for an ALICE ITS Upgrade in LS3”. In: *Preprint ALICE-PUBLIC-2018-013* (2019) (cit. on p. 20).

[45] ALICE Collaboration et al. *Upgrade of the ALICE Inner Tracking System during LS3: study of physics performance*. Tech. rep. ALICE-PUBLIC-2023-002, 2023 (cit. on pp. 20, 22).

[46] Ola Groettvik, ALICE Collaboration, et al. “ALICE ITS3: a bent stitched MAPS-based vertex detector”. In: *Journal of Instrumentation* 19.02 (2024), p. C02048 (cit. on p. 20).

[47] A Andronic et al. “Heavy-flavour and quarkonium production in the LHC era: from proton–proton to heavy-ion collisions”. In: *The European Physical Journal C* 76 (2016), pp. 1–151 (cit. on p. 21).

[48] Shreyasi Acharya et al. “Λc+ production in Pb–Pb collisions at sNN= 5.02 TeV”. In: *Physics Letters B* 793 (2019), pp. 212–223 (cit. on p. 21).

[49] V Drugakov, CMS collaboration, et al. "Production of Λc+ baryons in proton-proton and lead-lead collisions at sNN= 5.02 TeV". In: (2020) (cit. on p. 21).

[50] S. K. Radhakrishnan (STAR). *Proceedings of the 27th International Confer- ence on Ultra-Relativistic Nucleus-Nucleus Collisions (Quark Matter 2015): Lido di Venezia, Italy, May 14-17, 2018 (2018).* URL: `https://indico.cern.ch/event/%20656452/contributions/2869736/` (cit. on p. 21).

[51] Shreyasi Acharya et al. "Constraining hadronization mechanisms with Λc+/D0 production ratios in Pb–Pb collisions at sNN= 5.02 TeV". In: *Physics Letters B* 839 (2023), p. 137796 (cit. on p. 21).

[52] Shreyasi Acharya et al. "Charm-quark fragmentation fractions and production cross section at midrapidity in pp collisions at the LHC". In: *Physical Review D* 105.1 (2022), p. L011103 (cit. on p. 22).

[53] CMS collaboration et al. "The Phase-2 Upgrade of the CMS Tracker-Technical Design Report". In: *CERN, Geneva, Switzerland, Tech. Rep. CERN-LHCC-2017-009, CMS-TDR-014* (2017) (cit. on pp. 24, 25).

[54] Laura Gonella, ATLAS ITk Collaboration, et al. "The ATLAS ITk detector system for the Phase-II LHC upgrade". In: *Nuclear Instruments and Methods in Physics Research Section A: Accelerators, Spectrometers, Detectors and Associated Equipment* 1045 (2023), p. 167597 (cit. on pp. 24, 25).

[55] ATLAS Collaboration et al. *Expected tracking performance of the ATLAS Inner Tracker Upgrade for Phase-II.* Tech. rep. ATL-COM-SOFT-2023-128, 2023 (cit. on pp. 24, 25).

[56] Collaboration ATLAS. *Letter of Intent for the Phase-II Upgrade of the ATLAS Experiment.* Tech. rep. 2012 (cit. on pp. 24, 25).

[57] S. Passaggio. *The ATLAS ITk Pixel Detector Status and Roadmap.* URL: `https://cds.cern.ch/record/2883326/files/ATL-ITK-SLIDE-2023-636.pdf` (cit. on p. 25).

[58] N. Calace. *Expected Performance of the ATLAS Inner Tracker at the High-Luminosity LHC.* URL: `https://cds.cern.ch/record/2310669/files/ATL-PHYS-SLIDE-2018-144.pdf` (cit. on p. 25).

[59] S. Beolé. *Upgrade of Trackers at LHC.* URL: `https://indico.cern.ch/event/1109611/contributions/4790641/attachments/2444591/4188802/Beole_Upgrade_trackers.pdf` (cit. on p. 25).

[60] Emma Buchanan. “The LHCb vertex locator (VELO) pixel detector upgrade”. In: *Journal of Instrumentation* 12.01 (2017), p. C01013 (cit. on p. 25).

[61] LHCb Collaboration et al. *LHCb VELO upgrade technical design report*. Tech. rep. 2013 (cit. on p. 25).

[62] Z Citron et al. “Future physics opportunities for high-density QCD at the LHC with heavy-ion and proton beams”. In: *arXiv preprint arXiv:1812.06772* (2018) (cit. on p. 24).

[63] Albert M Sirunyan et al. “Production of Λc+ baryons in proton-proton and lead-lead collisions at sNN= 5.02 TeV”. In: *Physics Letters B* 803 (2020), p. 135328 (cit. on p. 24).

[64] Walter Snoeys. “Monolithic cmos sensors for high energy physics–challenges and perspectives”. In: *Nuclear instruments and methods in physics research section A: accelerators, spectrometers, detectors and associated equipment* (2023), p. 168678 (cit. on p. 27).

[65] Chris Damerell. “Tracking the rise of pixel detectors”. In: (2021) (cit. on p. 27).

[66] M Turala. “Silicon tracking detectors—historical overview”. In: *Nuclear Instruments and Methods in Physics Research Section A: Accelerators, Spectrometers, Detectors and Associated Equipment* 541.1-2 (2005), pp. 1–14 (cit. on p. 27).

[67] Leonardo Rossi. *Pixel detectors: From fundamentals to applications*. Springer Science & Business Media, 2006 (cit. on pp. 27, 31, 43).

[68] Jacob Fraden. *Handbook of modern sensors*. 1999 (cit. on p. 28).

[69] Particle Data Group et al. “Review of particle physics”. In: *Progress of Theoretical and Experimental Physics* 2020.8 (2020), p. 083C01 (cit. on p. 28).

[70] Charles Kittel and Paul McEuen. *Introduction to solid state physics*. John Wiley & Sons, 2018 (cit. on pp. 28, 30).

[71] J-P Colinge and Cynthia A Colinge. *Physics of semiconductor devices*. Springer Science & Business Media, 2005 (cit. on p. 28).

[72] Simon M Sze, Yiming Li, and Kwok K Ng. *Physics of semiconductor devices*. John wiley & sons, 2021 (cit. on pp. 29, 32).

[73] Glenn F Knoll. *Radiation detection and measurement*. John Wiley & Sons, 2010 (cit. on pp. 30, 32, 37, 38).

[74] Wikipedia. *p-n junction*. URL: `https://en.wikipedia.org/wiki/P-n_junction` (cit. on p. 31).

[75] William Shockley. "Problems related to pn junctions in silicon". In: *Solid-State Electronics* 2.1 (1961), pp. 35–67 (cit. on p. 32).

[76] Benoit Cushman-Roisin. *Diffusion Equation Part 1*. URL: `https://cushman.host.dartmouth.edu/courses/engs43/DiffusionEquation.pdf`.

[77] Claudio Canali et al. "Electron and hole drift velocity measurements in silicon and their empirical relation to electric field and temperature". In: *IEEE Transactions on electron devices* 22.11 (1975), pp. 1045–1047 (cit. on p. 32).

[78] WTRW Shockley and WT Read Jr. "Statistics of the recombinations of holes and electrons". In: *Physical review* 87.5 (1952), p. 835 (cit. on p. 34).

[79] Hermann Kolanoski and Norbert Wermes. *Particle Detectors: Fundamentals and Applications*. Oxford University Press, USA, 2020 (cit. on p. 35).

[80] Gerhard Lutz et al. *Semiconductor radiation detectors*. PUBDB-2020-02521. Springer, 2007 (cit. on p. 35).

[81] S Pirollo et al. "Radiation damage on p-type silicon detectors". In: *Nuclear Instruments and Methods in Physics Research Section A: Accelerators, Spectrometers, Detectors and Associated Equipment* 426.1 (1999), pp. 126–130 (cit. on p. 36).

[82] George C Messenger. "A summary review of displacement damage from high energy radiation in silicon semiconductors and semiconductor devices". In: *IEEE Transactions on nuclear Science* 39.3 (1992), pp. 468–473 (cit. on p. 37).

[83] Olaf Krasel et al. "Measurement of trapping time constants in proton-irradiated silicon pad detectors". In: *IEEE Transactions on Nuclear Science* 51.6 (2004), pp. 3055–3062 (cit. on p. 37).

[84] NS Saks, MG Ancona, and JA Modolo. "Radiation effects in MOS capacitors with very thin oxides at 80 K". In: *IEEE Transactions on Nuclear Science* 31.6 (1984), pp. 1249–1255 (cit. on p. 37).

[85] Nelson S Saks, Mario G Ancona, and John A Modolo. "Generation of interface states by ionizing radiation in very thin MOS oxides". In: *IEEE Transactions on Nuclear Science* 33.6 (1986), pp. 1185–1190 (cit. on p. 37).

[86] H Hillemanns et al. "Radiation hardness and detector performance of new 180nm CMOS MAPS prototype test structures developed for the upgrade of the ALICE Inner Tracking System". In: *2013 IEEE Nuclear Science Symposium and Medical Imaging Conference (2013 NSS/MIC)*. IEEE. 2013, pp. 1–5 (cit. on p. 37).

[87] William R Leo. *Techniques for nuclear and particle physics experiments: a how-to approach*. Springer Science & Business Media, 1994 (cit. on pp. 37, 40).

[88] Claudia Patrignani et al. “Review of particle physics”. In: (2016) (cit. on p. 37).

[89] Alessandro Bettini. *Introduction to elementary particle physics*. Cambridge University Press, 2024 (cit. on p. 37).

[90] Donald E Groom and SR Klein. “Passage of particles through matter”. In: *The European Physical Journal C-Particles and Fields* 15.1-4 (2000), pp. 163–173 (cit. on pp. 38, 39).

[91] Simon Eidelman et al. “Review of particle physics”. In: *Physics letters B* 592.1-4 (2004), pp. 1–5 (cit. on p. 39).

[92] Lev Davidovich Landau. “On the energy loss of fast particles by ionization”. In: *J. Phys.* 8 (1944), pp. 201–205 (cit. on p. 40).

[93] Particle Data Group et al. “Experimental methods and colliders”. In: *Physics Letters B* 592.1-4 (2004), pp. 235–274 (cit. on p. 40).

[94] Hans Bichsel. “Straggling in thin silicon detectors”. In: *Reviews of Modern Physics* 60.3 (1988), p. 663 (cit. on p. 40).

[95] I. B. Smirnov. *Introduction to the pai model.* URL: `https://indico.cern.ch/event/911950/contributions/3898109/attachments/2062395/3460176/Intro_PAI_wc.pdf` (cit. on p. 40).

[96] Helmuth Spieler. “Introduction to radiation detectors and electronics”. In: *VI. Position-Sensitive Detectors* (1998) (cit. on p. 41).

[97] Marie-Martine Bé et al. *Table of radionuclides (Vol. 3-A= 3 to 244)*. Vol. 3. 2006 (cit. on p. 42).

[98] MJOK Berger. *XCOM: photon cross sections database*. 2010. URL: `http://www.nist.gov/pml/data/xcom/index.cfm` (cit. on p. 42).

[99] BG Lowe. “Measurements of Fano factors in silicon and germanium in the low-energy X-ray region”. In: *Nuclear Instruments and Methods in Physics Research Section A: Accelerators, Spectrometers, Detectors and Associated Equipment* 399.2-3 (1997), pp. 354–364 (cit. on p. 42).

[100] MN Mazziotta. “Electron–hole pair creation energy and Fano factor temperature dependence in silicon”. In: *Nuclear Instruments and Methods in Physics Research Section A: Accelerators, Spectrometers, Detectors and Associated Equipment* 584.2-3 (2008), pp. 436–439 (cit. on p. 42).

[101] Deslattes et al. *X-ray transition energy database.* URL: `https://physics.nist.gov/%20PhysRefData/XrayTrans/Html/search.html` (cit. on p. 43).

[102] GW Fraser et al. "The X-ray energy response of silicon Part A. Theory". In: *Nuclear Instruments and Methods in Physics Research Section A: Accelerators, Spectrometers, Detectors and Associated Equipment* 350.1-2 (1994), pp. 368–378 (cit. on p. 43).

[103] P. Riedler. *Overview of monolithic silicon pixel detectors.* URL: `https://indico.cern.ch/event/374145/contributions/1796414/attachments/745477/1022655/CLIC_seminar_032015_priedler.pdf` (cit. on p. 44).

[104] Ch-K Kim, MJ Howes, and DV Morgan. "Charge-Coupled Devices and Systems". In: *New York: Wiley* 57 (1979) (cit. on p. 44).

[105] Miljenko Šuljić et al. "Study of monolithic active pixel sensors for the upgrade of the ALICE inner tracking system". In: (2018) (cit. on p. 46).

[106] G. et al. Aglieri Rinella. "Characterisation of analogue Monolithic Active Pixel Sensor test structures implemented in a 65 nm CMOS imaging process". In: *arXiv preprint arXiv:2403.08952* (2024) (cit. on pp. 47, 49, 50, 54, 61, 64, 68, 74, 77–81).

[107] W. Deng et al. "Design of an analog monolithic pixel sensor prototype in TPSCo 65 nm CMOS imaging technology". In: *Journal of Instrumentation* 18 (Jan. 2023), p. C01065. DOI: `10.1088/1748-0221/18/01/C01065` (cit. on pp. 47, 51).

[108] W. Snoeys. *Optimization of a 65 nm CMOS imaging technology for monolithic sensors for high energy physics.* URL: `https://indico.cern.ch/event/829863/contributions/5053903/attachments/2568452/4428586/PIXEL_2022_WS.pdf` (cit. on p. 47).

[109] W. Snoeys et al. "A process modification for CMOS monolithic active pixel sensors for enhanced depletion, timing performance and radiation tolerance". In: *NIMA* 871 (2017), pp. 90–96. ISSN: 0168-9002. DOI: `https://doi.org/10.1016/j.nima.2017.07.046` (cit. on p. 48).

[110] Walter Snoeys et al. "Optimization of a 65 nm CMOS imaging process for monolithic CMOS sensors for high energy physics". In: *POS PROCEEDINGS OF SCIENCE* (2023) (cit. on p. 49).

[111] V Sarritzu, ALICE Collaboration, et al. "A readout system for monolithic pixel sensor prototypes towards the upgrade of the ALICE Inner Tracking System". In: *Journal of Instrumentation* 18.01 (2023), p. C01047 (cit. on pp. 51, 52).

[112] Marie-Martine Bé et al. *Table of radionuclides (Vol. 3 - A = 3 to 244).* Ed. by Bureau International des Poids et Mesures. Vol. 3. 2006 (cit. on p. 63).

[113] B Denecke et al. "A set of X-ray fluorescence reference sources for the intrinsic efficiency calibration of Si (Li) detectors down to 1 keV". In: *Nuclear Instruments and Methods in Physics Research Section B: Beam Interactions with Materials and Atoms* 49.1-4 (1990), pp. 152–156 (cit. on p. 65).

[114] Thomas Walsh. "The plastic piping industry in North America". In: *Applied plastics engineering handbook*. Elsevier, 2011, pp. 585–602 (cit. on p. 65).

[115] M. Mager. *The Telescope Optimiser*. URL: `https://mmager.web.cern.ch/telescope/tracking.html` (cit. on p. 77).

[116] Jens Kröger, Simon Spannagel, and Morag Williams. "User manual for the corryvreckan test beam data reconstruction framework, version 1.0". In: *arXiv preprint arXiv:1912.00856* (2019) (cit. on p. 78).

[117] Giacomo Alocco. "Next-generation silicon pixel detectors for high energy physics experiments". PhD thesis. Cagliari, CA: University of Cagliari, Apr. 2024 (cit. on p. 78).

[118] Synopsys. *Technology Computer Aided Design (TCAD)*. URL: `https://www.synopsys.com/manufacturing/tcad.html` (cit. on pp. 85, 87).

[119] *Garfield++*. URL: `https://garfieldpp.web.cern.ch/garfieldpp/` (cit. on p. 85).

[120] *O2 simulation documentation*. URL: `https://aliceo2group.github.io/simulation/` (cit. on p. 85).

[121] Guido Masetti, Maurizio Severi, and Sandro Solmi. "Modeling of carrier mobility against carrier concentration in arsenic-, phosphorus-, and boron-doped silicon". In: *IEEE Transactions on electron devices* 30.7 (1983), pp. 764–769 (cit. on p. 91).

[122] Heinrich Schindler. "Microscopic simulation of particle detectors". PhD thesis. CERN, 2012 (cit. on p. 91).

[123] H. Schindler. *Garfield++ User Guide*. Version 2023 (cit. on p. 93).

[124] *X-ray Attenuation Length*. URL: `https://henke.lbl.gov/optical_constants/atten2.html` (cit. on p. 94).

[125] Simon Spannagel et al. "Allpix2: A modular simulation framework for silicon detectors". In: *Nuclear Instruments and Methods in Physics Research Section A: Accelerators, Spectrometers, Detectors and Associated Equipment* 901 (2018), pp. 164–172 (cit. on p. 102).

[126] *Letter of intent for ALICE 3: A next generation heavy-ion experiment at the LHC.* Tech. rep. 202 pages, 103 captioned figures, 19 tables. Geneva: CERN, 2022 (cit. on p. 110).

[127] Isabella Sanna. "Novel silicon detectors in ALICE at the LHC: The ITS3 and ALICE 3 upgrades". In: *EPJ Web of Conferences.* Vol. 296. EDP Sciences. 2024, p. 08002 (cit. on p. 110).

[128] Felix Reidt. *ALICE Upgrades.* 2024 (cit. on pp. 110, 111).

[129] CERN. *Future Circular Collider.* URL: `https://home.cern/science/accelerators/future-circular-collider` (cit. on p. 111).

[130] F. Reidt. *MAPS sensor developments in ALICE.* URL: `https://cds.cern.ch/record/2903876` (cit. on p. 111).

[131] Kunal Gautam and Ajit Kumar. "Characterisation of analogue MAPS fabricated in 65 nm technology for the ALICE ITS3". In: *Nuclear Instruments and Methods in Physics Research Section A: Accelerators, Spectrometers, Detectors and Associated Equipment* 1068 (Nov. 2024), p. 169787. ISSN: 0168-9002. DOI: `10.1016/j.nima.2024.169787` (cit. on p. 111).

List of Figures

1.1 Schematic of the CERN accelerator complex and the LHC experiments. Taken from [2]. 2
1.2 Illustration of the phase diagram of strongly interacting matter. Taken from [15]. 4
1.3 Space-time evolution of a heavy-ion collision. Taken from [20]. 5
1.4 Schematic view of all ALICE detectors. Taken from [24]. 6
1.5 Schematic view of the Inner Tracking System currently installed in ALICE. Taken from [31]. 9
1.6 Schematic drawing of the IB (left) and OB (right) staves. Taken from [31]. 9
1.7 Photograph of the ALPIDE chip. Taken from [24]. 11

2.1 Azimuthal distribution of the material budget of ITS2 layer 0 averaged over $|\eta| < 1$. Taken from [41]. 14
2.2 Engineering Model of ITS3. (a) Perspective, (b) A-side and (c) C-side views of the prototype. Three wafer-size blank silicon pieces (40 µm thin, 280 mm long), simulating the half-layers are kept bent by half-rings (A-side), longerons and wedges (C-side) made from carbon foam. Taken from [42]. 15
2.3 Concept diagram of the MOSS chip. Taken from [42]. 16
2.4 Simplified ITS3 Detector layout, (a) 3 top and 3 bottom half layers around the beam pipe within the cylindrical support structure supported by carbon foam half-rings and longerons, (b) radial distance of beam pipe and layers 0, 1, 2, (c) zoom of supporting carbon foam structures. Taken from [42]. 18
2.5 Half-detector: (a) Exploded and (b) assembled view. Taken from [42]. . . 19

2.6 (left) Impact parameter resolution and (right) tracking efficiecy as a function of the transverse momentum for ITS2 (blue) and ITS3 (red) in the transverse plane. Dashed lines show the results with ITS only, solid lines show the results with ITS+TPC. The lines represents the results obtained with a fast analytic tool, while circles show the results obtained with full MC. Taken from [42]. 21

2.7 $\Lambda_c \to pK^-\pi^+$ in central Pb-Pb collisions at $\sqrt{s_{NN}} = 5.5$ TeV: statistical significance (left) and signal-to-background ratio (right). Taken from [45]. 22

2.8 Expected relative uncertainty of the extraction of the T parameter from a fit to the invariant mass excess spectrum in $1.1 < M_{ee} < 2.0$ GeV/c^2. The results are shown for the ITS2 and ITS3 scenarios, with a tight cut on the quadratic sum of the impact parameters of the lepton pair. Error bars show the statistical uncertainties. The green boxes show the systematic uncertainties from the combinatorial background subtraction, the magenta boxes indicate systematic uncertainties related to the subtraction of the charm-decay electron contribution. Taken from [41]. 23

3.1 Band scheme for intrinsic conductivity in a semiconductor. At 0 K the conductivity is zero because all states in the valence band are filled and all states in the conduction band are vacant. As the temperature is increased, electrons are thermally excited from the valence band to the conduction band, where they become mobile. Taken from [70]. 28

3.2 Band scheme for doped silicon, with the corresponding donor/acceptor levels created in the silicon bandgap. Adjusted from [73]. 30

3.3 A visualization of a p-n junction atomic configuration (top), together with the space charge, electric field and potential along the junction (bottom). Adjusted from [74]. 31

3.4 Sketch of typical additional energy level locations due to lattice defects. Adjusted from [79]. 35

3.5 Effective doping concentration in a p-type silicon as a function of neutron fluence. Taken from [81]. 36

3.6 Stopping power curve for different materials versus momentum of various particles. Taken from [90]. 38

3.7 Energy loss distribution in silicon for 500 MeV pions, normalised to unity at the most probable value Δ_p/x, for different sensor thicknesses. Taken from [91]. 39

3.8 Energy dependent cross section of the three dominant energy loss mechanisms for photons in silicon. Taken from [96]. 41

3.9 Cross section scheme of a hybrid and a MAPS pixel. The hybrid pixel (a) consist of Si sensor bump-bonded to CMOS read-out electronics while MAPS (b) combines the two in a single volume. Taken from [103]. 44

3.10 Schematic view of the well-structure used for ALPIDE and the corresponding charge collection. 45

3.11 MAPS 3D schematic rappresentation - A matrix of 2×2 pixels belonging to the ALPIDE chip. Taken from [105]. 46

4.1 The APTS chip. 48

4.2 Half cross-sections of the three different pixel designs implemented: (a) standard: no additional low-dose implant, (b) modified: with deep blanket low dose n-type implant, and (c) modified with gap: with a gap in the deep low dose n-type implant at the pixel borders. Taken from [106]. . . . 49

4.3 Top view of half a pixel of a modified with gap pixel design for different shapes of the deep p-well: (a) reference shape and (b) finger-shaped p-well enclosure. Taken from [106]. 50

4.4 A schematic of the front-end chain of APTS. Taken from [107]. 51

4.5 DAQ system: FPGA-based DAQ board + chip-specific proximity + chip carrier card. Taken from [111]. 52

4.6 Typical waveforms from the 4 innermost pixels of an APTS chip (15 µm pitch, modified with gap, split 4). Data obtained pulsing the matrix with $V_{\mathrm{H}} = 1200$ mV and applying a back-bias of 1.2 V. Taken from [106]. . . . 54

4.7 Baseline distribution for the 4 innermost pixels of a modified with gap, split 4 chip with 15 μm pitch. Data were acquired at the nominal operating point and $V_{\mathrm{sub}} = 1.2$ V. 55

4.8 S/N ratio as a function of the back-bias voltage for the three chip designs of split 4 with a 15 μm pitch. The signal was obtained by injecting a pulse $V_{\mathrm{H}} = 1200$ mV and it is the average of the 16 pixels response. 56

4.9 Noise in electrons (mV) for split 4 at different V_{sub} and chip designs. The calibration in electrons was performed using data from ^{55}Fe source (see Sect. 4.4 for more details). 56

4.10 Output signal (a), gain (b) and signal amplitude (c) as a function of V_{reset}, for different front-end parameters settings (blue, orange, green and red) and back-bias voltages (dotted, dashed and solid). All the settings have I_{reset}=100 pA (see Section 4.3.1). The settings values are reported in Table 4.2. 57

4.11 Density plot illustrating the maximum gain and the V_{reset} range in which the gain is stable across all the possible combinations of front-end settings. The region highlighted in red is the prefered one, as it ensures values of gain higher than 0.55 and a range of stability higher than 180 mV. 59

4.12 Comparison at different temperatures of the signal waveform (averaged over 1000 events) for chips at different irradiation levels: Not irradiated (a), 10^{13} 1MeV $\mathrm{n_{eq}}$ $\mathrm{cm^{-2}}$ (b), 10^{14} 1MeV $\mathrm{n_{eq}}$ $\mathrm{cm^{-2}}$ (c), 10^{15} 1MeV $\mathrm{n_{eq}}$ $\mathrm{cm^{-2}}$ (d), $2\,10^{15}$ 1MeV $\mathrm{n_{eq}}$ $\mathrm{cm^{-2}}$ (e). 60

4.13 Comparison at different temperatures of the signal waveform (averaged over 1000 events) for chips at different irradiation levels, using an optimized working point ($\mathrm{I_{reset}}$ = 250 pA): Not irradiated (a), 10^{13} 1MeV $\mathrm{n_{eq}}$ $\mathrm{cm^{-2}}$ (b), 10^{14} 1MeV $\mathrm{n_{eq}}$ $\mathrm{cm^{-2}}$ (c), 10^{15} 1MeV $\mathrm{n_{eq}}$ $\mathrm{cm^{-2}}$ (d), $2\,10^{15}$ 1MeV $\mathrm{n_{eq}}$ $\mathrm{cm^{-2}}$ (e) and 10^{16} 1MeV $\mathrm{n_{eq}}$ $\mathrm{cm^{-2}}$ (f). Taken from [106]. 61

4.14 Capacitance (left) and energy resolution (right) comparison between different I_{reset}. APTS with 15 µm pitch, modified with gap, split 4, reference variant, V_{sub} = 1.2 V, standard readout. 62

4.15 ^{55}Fe source setup. The source is placed on top of a source holder which contains the chip and covers it from the light. The distance between the source and the chip is of around 1 cm. 63

4.16 (a) An example of a ^{55}Fe spectrum with the four peaks corresponding, starting from the left, to the: Si-$\mathrm{K_\alpha}$, escape peak (Mn-$\mathrm{K_\alpha}$ - Si-$\mathrm{K_\alpha}$), Mn-$\mathrm{K_\alpha}$ and Mn-$\mathrm{K_\beta}$. The final seed distribution is filled with the seed signals of the 4 central pixels of the matrix. This plot was obtained using a modified with gap chip with a pitch of 15 µm at a back-bias voltage of 1.2 V. (b) Energy calibration obtained using the peak means from the Gaussian fits on (a). The errors on the peak amplitudes are the ones resulting from the parameter evaluation of the Gaussian fits. Data are fitted with a linear function, with the offset set at zero and m as the slope parameter. All these data were taken at I_{reset} = 10 pA for a better energy resolution as anticipated in Section 4.3.1. Adjusted from [106]. 64

4.17 Schematic illustration of the setup used for the ^{55}Fe measurements with a Titanium foil target. 65

4.18 Seed signal distribution comparison among different fluorescence sources. The additional 3 peaks (of Ti-K_α, Ti-K_β and Cl-K_α) are fitted with Gaussian functions. This plot was obtained using a modified with gap chip with a pitch of 15 µm, also a value of $I_{\text{reset}} = 10$ pA was chosen for a better energy resolution. 66

4.19 On the left the energy calibration performed using different targets scenario to add K_α lines. The points are fitted with a linear function with the offset set to 0 and m as the slope parameter. The errors on the peak amplitudes are the ones resulting from the parameter evaluation of the Gaussian fits. On the right the associated residuals in percentage. 66

4.20 Seed signal distribution comparison between different back bias voltages, both in mV (a) and in electrons (b). This plot was obtained using a modified with gap chip with a pitch of 15 µm. Adjusted from [106]. 68

4.21 Seed signal distribution comparison between different implant geometries, both in mV (4.21(a)) and in electrons (4.21(b)). This plot was obtained using chips with a pitch of 15 µm and at a back-bias voltage of 1.2 V. . . 69

4.22 Seed signal distribution comparison between different doping profiles, both in mV (4.22(a)) and in electrons (4.22(b)). This plot was obtained using modified with gap chips with a pitch of 15 µm and at a back-bias voltage of 4.8 V. 70

4.23 Seed signal distribution in electrons compared between different pixel pitches for the standard (a), modified (b) and modified with gap (c) designs. These plots have been obtained with a back-bias voltage of 1.2 V. . 71

4.24 Seed signal distribution comparison between different levels of NIEL irradiation, both in mV (4.24(a)) and in electrons (4.24(b)). This plot was obtained using modified with gap chips with a pitch of 15 µm and at a back-bias voltage of 1.2 V. For irradiation levels of 2 10^{15} 1 MeV n_{eq} cm^{-2} or higher, the measurements have been taken with $I_{\text{reset}} = 250$ pA (see Section 4.3.1). 72

4.25 Seed signal distribution comparison between different pixel pitches of a chip irradiated 10^{15} 1MeV n_{eq} cm^{-2} in electrons. This plot was obtained using modified with gap chips and at a back-bias voltage of 1.2 V. 73

4.26 Comparison of the main characteristics extracted from the ^{55}Fe spectra. The light blue window in the last column refers to the data points acquired with $I_{\mathrm{reset}} = 250$ pA, all the others with $I_{\mathrm{reset}} = 100$ pA. Taken from [106]. 74

4.27 Scheme of the telescope setup used at SPS test beams in October 2022 and May 2023. Two APTS are enclosed in two groups of three ALPIDE each. The trigger is provided by one of the two APTS. Not to scale. Taken from [106]. 77

4.28 Telescope setup used at SPS test beams in October 2022 and May 2023. The setup was positioned inside a box and covered from the light. 78

4.29 (Top left) Comparison between different designs of the seed pixel signal charge distribution for a pitch of 15 µm. (Top right) Comparison between different pixel pitch sizes of the seed pixel signal charge distribution for modified with gap sensors. (Bottom) Comparison between different NIEL irradiation doses of the seed pixel signal charge distribution for a modified with gap sensor with a pitch 15 µm. Adjusted from [106]. 79

4.30 Efficiency comparison between different reverse substrate voltages as a function of the applied seed threshold. The dotted lines indicate the threshold corresponding to 3 times the RMS noise value. APTS with 15 µm pitch, modified with gap, split 4, reference variant. Taken from [106]. 80

4.31 Comparison of the main characteristics extracted from the efficiency plots versus threshold. APTS with split 4, reference variant. Taken from [106]. 81

5.1 Sketch of the simulation workflow. 86

5.2 Sketch of an APTS cross section and the geometric parameters used for the TCAD device simulation. The implant depth, gap width and pixel pitch are the parameters that can be varied according to the simulated variant. Not to scale. 88

5.3 Cross section of half a pixel cell in TCAD. Here, a finer meshing is used for the epitaxial layer, and a coarser one for the substrate. Simulation not based on the actual doping profiles. 89

5.4 Cross section of a typical electric field (absolute value) of one pixel cell along the epitaxial layer for a modified with gap APTS with a 15 µm pixel pitch. Simulation not based on the actual doping profiles. 90

5.5 Sketch of a simulated matrix of 5 × 5 pixels with a pitch of 15 µm. In red the range of the scanned injection coordinates is highlighted. 92

5.6 Comparison between simulated and actual ^{55}Fe spectrum for different cluster sizes. Simulations carried out without a recombination model in Garfield++. These data refer to a modified with gap APTS with a pixel pitch of 15 µm and at a back-bias of 1.2 V. 96

5.7 Comparison between simulated and measured ^{55}Fe spectra for different cluster sizes. Each sub-plot is normalised individually. Simulations carried out without a recombination model in Garfield++. These data refer to a modified with gap APTS with a pixel pitch of 15 µm and at a back-bias of 1.2 V. 97

5.8 Comparison between simulated and measured cluster size distributions. Simulations carried out without a recombination model in Garfield++. These data refer to a modified with gap APTS with a pixel pitch of 15 µm and at a back-bias of 1.2 V. 98

5.9 Migration lines (drift+diffusion) of the collected electrons for the seed pixel and the two neighbouring pixels along the x-axis. Data obtained injecting 100 electrons at a depth of 12 µm in the seed pixel. On the left without any time window and on the right with a time window of 3 ns applied to the simulation. The red star indicates the injection point. . . . 98

5.10 Comparison between simulated and measured ^{55}Fe spectra for different cluster sizes, with the application of a 3 ns time window to the simulation. These data refer to a modified with gap APTS with a pixel pitch of 15 µm and at a back-bias of 1.2 V. 99

5.11 Comparison between simulated and measured cluster size distributions, with the application of a 3 ns time window to the simulation. These data refer to a modified with gap APTS with a pixel pitch of 15 µm and at a back-bias of 1.2 V. 100

5.12 Comparison between simulated and measured ^{55}Fe spectra for different implant geoemtries. These data refer to APTS pixel pitch of 15 µm and at a back-bias of 1.2 V. 101

5.13 Comparison between simulated and measured ^{55}Fe spectra for different cluster sizes. Simulations carried out with the new recombination modelling of Garfield++. These data refer to a modified with gap APTS with a pixel pitch of 15 µm and at a back-bias of 1.2 V. 102

5.14 Comparison between simulated and measured cluster size distributions. Simulations carried out with the new recombination modelling of Garfield++. These data refer to APTS pixel pitch of 15 µm and at a back-bias of 1.2 V.103

5.15 Comparison between simulated and measured ^{55}Fe spectra for different implant geoemtries. Simulations carried out with the new recombination modelling of Garfield++. These data refer to APTS pixel pitch of 15 µm and at a back-bias of 1.2 V. 104

5.16 Comparison between simulated and measured ^{55}Fe spectra for different pixel pitches. Simulations carried out with the new recombination modelling of Garfield++. These data refer to APTS pixel pitch of 15 µm and at a back-bias of 1.2 V. 104

6.1 A 300 mm ER1 wafer, containing six MOSS and MOST stitched sensors (indicated), as well as a number of small prototype chips. Taken from [42]. 108

6.2 CMOS wafer stitching plan and dimensions of the ITS3 sensors in mm. The actual chip design dimensions are shown with a precision of 1 µm. The dashed black rectangle indicates one of the five segments. The red rectangle shows one of the 3 possible groupings of three segments to make one of the sensors for layer 0. The blue rectangle shows one of the 2 possible groupings of four segments to make one of the sensors for layer 1. The purple rectangle shows the grouping of five segments to make layer 2. The beam axis direction (z) and the azimuthal direction (rϕ) are shown. The A side and C side labels indicate the ALICE detector sides. The illustration in the top of the figure shows the placement of the 3 lower bottom sensors bent around the beam pipe illustrating that the detector consists of 6 silicon sensors only. Taken from [42]. 109

6.3 Pointing resolution progression with the future ALICE upgrades. Taken from [128]. 110

6.4 Layout of the ALICE 3 tracking system. Taken from [128]. 111

A.1 Chip output voltage obtained at the 96th frame, as a function of the chip output voltage at the 95th (left), 92nd (middle) and 76th frame (right). . . 115

B.1 Signal amplitude calculated scanning the delay between the trigger event and the starting point of the system sampling (left), its distribution (center) and the error associated with it (right) for different I_{reset}. 117

C.1 Comparison between simulated and measured ^{55}Fe spectra for different cluster sizes. Simulations carried out both with the new recombination modelling of Garfield++ and with Allpix2. These data refer to a modified with gap APTS with a pixel pitch of 15 µm and at a back-bias of 1.2 V. . 119

C.2 Comparison between simulated and measured cluster size distributions. Simulations carried out both with the new recombination modelling of Garfield++ and with Allpix2. These data refer to APTS pixel pitch of 15 µm and at a back-bias of 1.2 V. 120

List of Tables

2.1 Characteristics of the MLR1 test structures developed for ITS3. 17
2.2 Geometrical parameters of ITS3 Layers. 19
2.3 Summary of LHC vertex detectors and their features. 25

3.1 Default parameters for doping- and temperature-dependent SRH lifetime. 34
3.2 Emissions of ^{55}Fe [97]. 42

4.1 Main characteristics and variants of the APTS silicon sensors. 48
4.2 Some of the front-end settings explored for the determiantion of the operation point of APTS. 58

Acknowledgements

First and foremost, I would like to express my deepest gratitude to my two supervisors, Dr. Magnus Mager and Prof. Laura Fabbietti, for their invaluable guidance, support, and encouragement throughout the course of my research. Their expertise and dedication have been fundamental in shaping both the scientific direction of this thesis and my growth as a researcher.

I would also like to extend my heartfelt thanks to the entire ITS3 group, whose collaborative spirit and constructive discussions created an inspiring research environment. I am especially grateful to Francesca Carnesecchi, Valerio Sarritzu, Walter Snoeys, Corentin Lemoine, and Giulio Borghello, with whom I had the privilege to work closely. Their insights and technical expertise have greatly enriched my experience, and this work would not have been possible without their contributions. A heartfelt thank you to Heinrich Schindler for his support and collaboration in the Garfield++ software modifications.

My profound gratitude goes to my family, my friends, and to Fabrizio, whose encouragement and belief in me provided the strength and motivation I needed during this journey.

Finally, I am grateful to everyone who, in one way or another, has contributed to the completion of this thesis. Your support and encouragement have made all the difference.